The Design of Hardware and Signal Processing for a Stepped Frequency Continuous Wave Ground Penetrating Radar

by

Alan Langman
BSc (Eng) UCT (1991)

A thesis submitted to the Department of Electrical Engineering,
University of Cape Town, in fulfilment of the requirements
for the degree of

Doctor of Philosophy

at the

UNIVERSITY OF CAPE TOWN

March 2002

Declaration

I declare that this thesis is my own, unaided work. It is being submitted for the degree of Doctor of Philosophy at the University of Cape Town. It has not been submitted before for any degree or examination at any other university.

Signature of Author .....

Department of Electrical Engineering
Cape Town, March 2002

Abstract

A Ground Penetrating Radar (GPR) sensor is required to provide information that will allow the user to detect, classify and identify the target. This is an extremely tough requirement, especially when one considers the limited amount of information provided by most GPRs to accomplish this task. One way of increasing this information is to capture the complete scattering matrix of the received radar waveform.

The objective of this thesis is to develop a signal processing technique to extract polarimetric feature vectors from Stepped Frequency Continuous Wave (SFCW) GPR data. This was achieved by first developing an algorithm to extract the parameters from single polarization SFCW GPR data and then extending this algorithm to extract target features from fully polarimetric data.

A model is required to enable the extraction of target parameters from raw radar data. A single polarization SFCW GPR model is developed based on the radar geometry and linear approximations to the wavenumber in a lossy medium. Assuming high operating frequencies and/or low conductive losses, the model is shown to be equivalent to the exponential model found in signal processing theory. A number of algorithms exist to extract the required target parameters from the measured data in a least squared sense. In this thesis the Matrix Pencil-of-Function Method is used. Numerical simulations are presented to show the performance of this algorithm for increasing model error. Simulations are also provided to compare the standard Inverse Discrete Fourier Transform (IDFT) with the algorithm presented in this thesis. The processing is applied to two sets of measured radar data using the radar developed in the thesis. The

technique was able to locate the position of the scatterers for both sets of data, thus demonstrating the success of the algorithm on practical measurements.

The single polarization model is extended to a fully polarimetric SFCW GPR model. The model is shown to relate to the multi-dimensional exponential signal processing model, given certain assumptions about the target scattering damping factor. The multi-snapshot Matrix Pencil-of-Function Method is used to extract the scattering matrix parameters from the raw polarimetric stepped frequency data. Those Huynen target parameters that are independent of the properties of the medium, are extracted from the estimated scattering matrices. Simulations are performed to examine the performance of the algorithm for increasing conductive and dielectric losses. The algorithm is also applied to measured data for a number of targets buried a few centimeters below the ground surface, with promising results.

Finally, the thesis describes the design and development of a low cost, compact and low power SFCW GPR system. It addresses both the philosophy as well as the technology that was used to develop a $200 - 1600$ MHz and a $1 - 2$ GHz system. The system is built around a dual synthesizer heterodyne architecture with a single intermediate frequency stage and a novel coherent demodulator system - with a single reference source. Comparison of the radar system with a commercial impulse system, shows that the results are of a similar quality. Further measurements demonstrate the radar performance for different field test cases, including the mapping of the bottom of an outdoor testsite down to 1.6 m.

To my wife and parents

Acknowledgements

I would like to offer my most sincere thanks to my supervisor, Professor Michael Inggs, for his continual support, guidance, persistence, patience, flexibility and suggestions throughout the time of this project. I have benefitted greatly from his expertise, help, advice and friendship. I am also grateful for his financial assistance and for the honour of having a true highlander play the bagpipes at my wedding.

I would also like to thank Reutech Radar Systems, for their financial contributions that provided the funding to develop the first MercuryA radar system. I am also indebted to Ball Aerospace for providing the funding to develop the MercuryB radar system. I am particularly thankful to four of its employees - Robert, Vince, Dave and Robert for providing such an incredible work environment and making the experience of working with them such fun.

I have received much help and support from numerous past and present members of the Radar Remote Sensing Group. These include those who helped directly with building the radars - Simon Dimiao, Brian Burns, Gordan Farquharson, Alex Rossi, the late Rolf Lengenfelder, Allen Wallis, Carl van Schaik and Grant Carter and those who helped indirectly through numerous technical discussions - Pete Golda, Richard Lord, Andrew Wilkinson, Jasper Horrel and Dr Morrison. Also thanks to Judy Mackintosch for providing a simple interface to the university administration system.

I am greatly indebted to Pete Golda, Shuan and Jenni Courtney for all their help in proof reading this document.

A special thanks to my mom and dad who have given me the freedom to choose and their continued support in all my choices. A very special thanks to my wife for providing continued support, motivation and love through all the highs and lows.

Most of all thanks to God who makes the impossible, possible.

Contents

Declaration ii

Abstract iv

Acknowledgements vii

Contents ix

List of Figures xiii

List of Tables xx

Nomenclature xxii

1 Introduction 1

1.1 Problem Description 3
1.2 Thesis Objectives 6
1.3 Approach 6
1.3.1 Signal Processing 7
1.3.2 Hardware Design 8
1.4 Thesis Overview 9
1.5 Statement of Originality 10

2 Single Polarization GPR Model Based Processing 12

2.1 Introduction 12
2.2 Contributions 13
2.3 Motivation 14

2.4 Simple GPR Scattering Model 14
2.4.1 Approximation for an EM Wave Propagating in a Lossy Medium 16
2.4.2 Scattering from a Target 22
2.4.3 Received Signal at GPR 23
2.5 SFCW Modulation 24
2.6 Parameter Estimation 28
2.6.1 Matrix Pencil-of-Function Method 31
2.6.2 Model Error 33
2.6.3 IDFT Method 46
2.7 Simulation Results 48
2.7.1 Conductive Losses 49
2.7.2 Dielectric Losses 55
2.7.3 Discussion 56
2.8 Measurements 63
2.8.1 Buried Antenna Pipe Measurements 63
2.9 Buried Pipe Measurement 70
2.10 Conclusions 73

3 Fully Polarimetric GPR Model Based Processing 76
3.1 Introduction 76
3.2 Contribution 78
3.3 Polarimetric Model 78
3.3.1 Propagation of an EM Wave in a Lossy Medium 80
3.3.2 Scattering From a Target 83
3.3.3 Complete Polarization Radar Model 84
3.3.4 Target Invariant Parameters 85
3.4 SFCW Modulation 90
3.5 Parameter Estimation 96
3.5.1 Multi-Snapshot Matrix Pencil-of-Function Method 97
3.5.2 Determining the Huynen Target Parameters 101
3.5.3 Model Errors 104
3.6 Simulations 104

3.6.1 Radar with no Thermal Noise ($ns = -\infty$ dBm) 105
3.6.2 Radar with Thermal Noise ($ns = -145$ dBm) 106
3.7 Measurements 113
3.7.1 Results 117
3.8 Conclusions 130

4 Implementation of a SFCW Radar **132**
4.1 Introduction 132
4.2 Contributions 134
4.3 Scope 135
4.4 Modulation Techniques 135
4.5 Possible Radar Architectures 136
4.5.1 Homodyne Architecture 137
4.5.2 Heterodyne Dual Synthesizer Architecture 139
4.6 Radar Design 141
4.6.1 Radar Architecture 142
4.6.2 System Coherency 143
4.6.3 System Phase Noise 144
4.6.4 Effects of Temperature Variations 146
4.6.5 Implementation of an IQ Demodulator 147
4.7 Radar Implementation 150
4.8 Radar Measurements 156
4.8.1 Measurement 1: Back Yard 156
4.8.2 Measurement 2: Ball Aerospace Indoor Test Pit 157
4.8.3 Measurement 3: Outdoor Test Pit - Ball Aerospace 158
4.8.4 Measurement 4: Landmine Detection Measurements 158
4.9 Conclusions 160

5 Conclusions and Scope for Future Work **162**
5.1 Conclusions 162
5.1.1 Single Polarization SFCW GPR 163
5.1.2 Fully Polarimetric SFCW GPR 163
5.1.3 Hardware Development 165

5.2 Future Work 165

A Linearization of the Wavenumber k_m 168

A.1 Case 1: Purely Conductive Losses 169

A.2 Case 2: Purely Dielectric Losses 170

A.3 Case 2: Combined Conductive and Dielectric Losses 170

B Resolution and Spectral Shape 173

C Error Analysis for an IDFT Based Target Parameter Estimation 178

List of Figures

1.1 View of the GPR problem space 4

2.1 GPR/target geometry 15

2.2 Plot of the percentage model error as a function of $\tan\delta$ 19

2.3 Plot of percentage model error and 2 way medium loss as a function of conductivity (σ_m) 21

2.4 Conceptual block diagram of a SFCW GPR 24

2.5 Plot of percentage model error as a function of conductivity for two targets with increasing target separation 35

2.6 Estimated radar model parameters as a function of conductivity for targets located at 1 m and 1.05 m 37

2.7 Plot of estimated poles (z_p) for increasing conductivity 38

2.8 Estimated radar model parameters as a function of conductivity for targets located at 1 m and 2.4 m 39

2.9 Plot of estimated pole positions (z_p) as a function of conductivity 40

2.10 Plot of model parameter errors for increasing conductivity and for target spacing of $d_p = 0.01$, 0.02, 0.03, 0.06, 0.1 m 41

2.11 Plot of model parameter errors for increasing conductivity and for target spacing of $d_p = 0.05$, 0.2, 0.5, 2, 5 m 42

2.12 Plot of model parameter errors for increasing conductivity with $s_1 = 1$ m and $s_2 = 0.05$, 0.3, 1, 3, 10 m 43

2.13 Plot of model parameter errors for increasing conductivity and for target scattering phase of $\tau_1 = 0$ rad, $\tau_2 = -2$, -0.8, 0, 0.8, 2 rad 44

2.14 Plot of model parameter errors for increasing conductivity and for target dispersion of $\gamma_1 = 0$, $\gamma_2 = -0.001$, -0.003, -0.01, -0.03, -0.1 45

2.15 Plot of raw and processed data for a conductivity of 1 mS/m ($\tan\delta \approx 0$, $m_e \approx 0$ and SNR ≈ 111 dB) 50

2.16 Plot of raw and processed data for a conductivity of 10 mS/m ($\tan\delta \approx 0.05$, $m_e \approx 0.01$, and SNR ≈ 85 dB) 50

2.17 Plot of raw and processed data for a conductivity of 20 mS/m ($\tan\delta \approx 0.1$, $m_e \approx 0.04$, and SNR ≈ 56 dB) 51

2.18 Plot of raw and processed data for a conductivity of 30 mS/m ($\tan\delta \approx 0.15$, $m_e \approx 0.09$, and SNR ≈ 27 dB). 51

2.19 Plot of raw and processed data for a conductivity of 40 smS/m ($\tan\delta \approx 0.2$, $m_e \approx 0.15$ and SNR ≈ 2.3 dB). 52

2.20 Plot of extracted target parameters as a function of conductivity . 53

2.21 Plot of the RMS error for the model target parameters as a function of conductivity 54

2.22 Plot of $\eta(p)$ for $p \leq l$ for $\sigma_m = 1$, 5, 10, 20, 30 and 40 mS/m . . . 55

2.23 Plot of raw and processed data for $\epsilon_r = 6 - 0.01j$ ($\tan\delta \approx 0$, $m_e \approx 0$ and SNR ≈ 113 dB) 56

2.24 Plot of raw and processed data for $\epsilon_r = 6 - 0.1j$ ($\tan\delta \approx 0.02$, $m_e \approx 0$ and SNR ≈ 100 dB) 57

2.25 Plot of raw and processed data for $\epsilon_r = 6 - 0.2j$ ($\tan\delta \approx 0.03$, $m_e \approx 0$ and SNR ≈ 88 dB) 58

2.26 Plot of raw and processed data for $\epsilon_r = 6 - 0.4j$ ($\tan\delta \approx 0.07$, $m_e \approx 0$ and SNR ≈ 66 dB) 59

2.27 Plot of raw and processed data for $\epsilon_r = 6 - 0.8j$ ($\tan\delta \approx 0.13$, $m_e \approx 0$ and SNR ≈ 25 dB) 60

2.28 Plot of extracted target parameters as a function of the imaginery permittivity 61

2.29 Plot of $\eta(p)$ for $p \leq l$ for $\varepsilon_r^{''} = -0.01$, 0.1, 0.2, 0.4, 0.8 and 1.0 . . 62

2.30 Measurement setup for buried antenna pipe measurement 64

2.31 Two dimensional magnitude plot of the radar impulse response . . 64

2.32 Plot of the raw and processed mean profile response of the measured data 65

2.33 Plot of raw and processed data for the 5^{th} range profile (0.25 m) . 66

2.34 Plot of raw and processed data for the 19^{th} range profile (0.95 m) 67

2.35 Plot of raw and processed data for the 21^{st} range profile (1.0 m) . 67

2.36 Amplitude response for each principle component vector from the MPM alogirthm as a function of pipe azimuth position 68

2.37 Images of the processed radar data after background subtraction. Figure (a) plots the amplitude response of the radar impulse response. Figure (b) plots the position of the target vectors estimated from the MPM algorithm as a function of position 69

2.38 Position plot of the distance between target at the same azimuth location as a function of azimuth 70

2.39 Measurement setup for pipe buried in a large plastic tub 71

2.40 Picture of the measurement setup for the buried pipe measurement 71

2.41 Images of the processed radar data after background subtraction. Figure (a) plots the real part of the radar impulse response. Figure (b) plots the position of the target vectors estimated from the MPM algorithm as a function of position. 72

2.42 Position plot of the distance between pipe target and the ground surface at the same azimuth location as a function of azimuth. . . 73

2.43 2D Plots of the processed radar data after background subtraction. Figure (a) plots the real part of the radar impulse response. Figure (b) plots the position of the target vectors estimated from the MPM algorithm as a function of position. 74

3.1 GPR/target geometry 79

3.2 Polarizarion Elipse 82

3.3 Block diagram of SFCW Polarimetric radar showing the defined coordinate system 90

3.4 Plots of target position (d_p) and dispersion, (γ_p) and their errors as a function of conductivity (σ_m) for a radar noise floor of $-\infty$ dBm106

3.5 Plot of the Huynen target parameters ($M_p, \gamma_p^h, \theta_p, \tau_p$) as a function of conductivity (σ_m) for a radar noise floor of $-\infty$ dBm 107

3.6 Plot of the Huynen target parameter errors (in $M_p, \gamma_p^h, \theta_p, \tau_p$) as a function of conductivity (σ_m) for a radar noise floor of $-\infty$ dBm 108

3.7 Plots of target position (d_p) and dispersion (γ_p) and their errors as a function of conductivity (σ_m) for a radar noise floor of -145 dBm110

3.8 Plot of the Huynen target parameters ($M_p, \gamma_p^h, \theta_p, \tau_p$) as a function of conductivity (σ_m) for a radar noise floor of -145 dBm 111

3.9 Plot of the Huynen target parameter errors (in $M_p, \gamma_p^h, \theta_p, \tau_p$) as a function of conductivity (σ_m) for a radar noise floor of -145 dBm112

3.10 Plot of received power as a function of position for $s_{xx}, s_{xy}, s_{yx}, s_{yy}$ for $\sigma = 10$ mS/m and $\varepsilon_r = 6$ 113

3.11 Plot of received power as a function of position for $s_{xx}, s_{xy}, s_{yx}, s_{yy}$ for $\sigma = 10$ mS/m and $\varepsilon_r = 6 - 0.1j$ 114

3.12 Plot of received power as a function of position for $s_{xx}, s_{xy}, s_{yx}, s_{yy}$ for $\sigma = 10$ mS/m and $\varepsilon_r = 6 - 0.2j$ 114

3.13 Plot of received power as a function of position for $s_{xx}, s_{xy}, s_{yx}, s_{yy}$ for $\sigma = 20$ mS/m and $\varepsilon_r = 6 - 0.2j$ 115

3.14 Plot of received power as a function of position for $s_{xx}, s_{xy}, s_{yx}, s_{yy}$ for $\sigma = 25$ mS/m and $\varepsilon_r = 6 - 0.3j$ 115

3.15 Block diagram of the polarimetric measurements setup. 116

3.16 Photograph of the antenna setup for the polarimetric measurements. 116

3.17 Photograph of antenna location above the ground surface 118

3.18 Plot of received power as a function of position for $s_{xx}, s_{xy}, s_{yx}, s_{yy}$ for ground surface measurement 119

3.19 Metal cylinder 120

3.20 Plot of received power as a function of position for $s_{xx}, s_{xy}, s_{yx}, s_{yy}$ for a metal cylinder 121

3.21 Polystyrene cylinder 122

3.22 Plot of received power as a function of position for $s_{xx}, s_{xy}, s_{yx}, s_{yy}$ for a polystyrene cylinder 123

3.23 Metal rod 123

3.24 Plot of received power as a function of position for $s_{xx}, s_{xy}, s_{yx}, s_{yy}$ for a metal rod parallel to the horizontal polarization axis 124

3.25 Plot of received power as a function of position for $s_{xx}, s_{xy}, s_{yx}, s_{yy}$ for a metal rod at 45° to the horizontal polarization axis 125

3.26 Plot of received power as a function of position for $s_{xx}, s_{xy}, s_{yx}, s_{yy}$ for a metal rod at 90° to the horizontal polarization axis 126

3.27 Sixteen metal screws 127

3.28 Plot of received power as a function of position for $s_{xx}, s_{xy}, s_{yx}, s_{yy}$ for sixteen metal screws 128

3.29 Metal sphere 128

3.30 Plot of received power as a function of position for $s_{xx}, s_{xy}, s_{yx}, s_{yy}$ for the metal sphere 129

4.1 Block diagram of a homodyne architecture 137

4.2 Block diagram of a heterodyne radar architecture 140

4.3 Block diagram of the Stepped Frequency Continuous Wave GPR . 142

4.4 Typical phase noise plot for a PLL [1] 144

4.5 Measured phase noise for the MercuryA transmit synthesiser at 1.5 GHz 145

4.6 Measured IF phase noise at 1 MHz for the MercuryA radar with a transmit frequency of 1.5 GHz 146

4.7 Filtered IF for the MercuryA radar system 147

4.8 Graphical view of the sampler for a SFCW GPR 148

4.9 Block diagram of the implementation of the MercuryB radar system.151

4.10 Photograph of the MercuryB radar hardware. 154

4.11 Photograph of the MercuryA radar system including the radar transceiver, fibre optic communication link, batteries and antennas 155

4.12 Radar profile for yard measurements 156

4.13 Comparison between MercuryB SFCW GPR and the Pulse Ekko 1000 impulse GPR 157

4.14 Radar profile of a test pit at Ball Aerospace, Broomfield Colorado 158

4.15 Photograph of mine test site at the CSIR, Pretoria 159

4.16 Radar profile of a cross section through the centre of the mine test site 160

B.1 Frequency/Time transform for a pulse waveform 173

B.2 Resolution of two pulses 174

B.3 Spectra of a bandlimited Gaussian pulse and conventional SFCWwaveform 175

B.4 Impulse response of a bandlimited Gaussian pulse and SFCW waveform 176

C.1 Range profile for $p \geq l$ as a target is moved off a range bin 180

C.2 The range profile for a target located at $15dz$ for increasing ε_m'' . . 181

C.3 The range profile for a target located at $15dz$ for increasing conductivity σ_m 182

List of Tables

2.1 Radar parameters for the single polarization simulations 48

2.2 List of targets and their parameters for the single polarization simulations 49

3.1 Radar parameters for the fully polarimetric simulations 104

3.2 List of targets and their parameters for the fully polarimetric simulations 105

3.3 Huynen medium independent target parameters for the ground surface 119

3.4 Table of ground response parameters extracted from the various target profiles 120

3.5 Huynen medium independent target parameters for the metal disk 121

3.6 Huynen medium independent target parameters for the polystyrene cylinder 122

3.7 Huynen medium independent target parameters for the metal rod 124

3.8 Huynen medium independent target parameters for the metal screws 127

3.9 Huynen medium independent target parameters the metal sphere 128

4.1 MercuryB specification summary 150

Nomenclature

CW	—	Continuous Wave.
DC	—	Direct current.
DPLL	—	Digital Phase Lock Loop.
DOD	—	Department of Defence.
ELF	—	Estimated Linearity Factor.
EM	—	Electromagnetic.
EMI	—	Electromagnetic Interference.
ESPRIT	—	Estimation of Signal Parameters Via Rotational Invariance Techniques.
FMCW	—	Frequency Modulated Continuous Wave.
FPGA	—	Field Programmible Gate Array.
GPR	—	Ground penetrating radar.
GTD	—	Geometric Theory of Diffraction.
HMI	—	Human Machine Interface.
I	—	In-phase.
IDFT	—	Inverse Discrete Fourier Transform.
IF	—	Intermediate Frequency.
IFFT	—	Inverse Fast Fourier Transform.
LOS	—	Local Oscillator Synthesizer.
LS	—	Least squared.
LSE	—	Least Squared Estimator.
MPM	—	Matrix Pencil-of-Function Method.
MUSIC	—	Multiple Signal Classification.
OSU	—	Ohio State University.
PLL	—	Phase Lock Loop.
PSU	—	Power Supply Unit.

PV — Principle Vector.
Q — Quadrature.
RCDC — Radar Data Capture and Control.
RF — Radio Frequency.
RMS — Root Mean Square.
RX — Receiver.
SFCW — Stepped Frequency Continuous Wave Radar.
SNR — Signal-to-noise Ratio.
TEM — Transverse Electromagnetic.
TX — Transmit.
TXS — Transmit Synthesizer.
TLS — Total Least Squared.
TPR — Transcient Polarization Response.
US — United States.

Chapter 1

Introduction

There is a great need for technologies that can *see* underground. The applications for such technologies are almost endless - ranging from the need to find the almost 100 million life threatening landmines located in fifty countries around the world to searching for antiquities. Currently there is no single technology that can provide a complete solution. Various techniques for extracting information from objects that are not optically visible have existed for quite some time. These include: seismic, nuclear, thermographic, radiometric, electrical resistivity and electromagnetic techniques. One of the more promising of these technologies is Ground Penetrating Radar (GPR). GPR is an electromagnetic technique designed primarily for subsurface exploration, characterization and monitoring. It has the advantage over other remote sensing techniques, in that one can quickly and non-invasively create high resolution images of subsurface features.

According to Daniels [2] the earliest use of electromagnetic signals to locate objects was attributed to Hülsmeyer in 1904 and recorded later in a German patent by Leimbach and Löwy [3]. Leimbach *et al.* [3] transmitted and received a continuos wave signal between dipoles buried in a vertical borehole. The first ground penetrating radar survey, using radio interferometry, was performed in Austria in 1929 to *sound* the depth of a glacier [4]. Olhoeft reports that the GPR field was fairly quiet until the late 1960's and early 1970's with the Apollo 17 Moon sounder experiment [4]. Olhoeft continues to say that shortly after

this the first GPR equipment manufacturing company (Geological Survey Inc.) was formed. According to Olhoeft this resulted in an increase in research which gave birth to the GPR industry. Currently there are a number of equipment manufactures and companies providing services for a large and diverse user base [4, 5]. There has also been an increase in academic interest, resulting in eight international conferences dedicated to GPR technology and applications [6, 7, 8, 9, 10, 11, 12, 13], a number of sessions at The International Society of Optical Engineering (SPIE) conferences and a journal dedicated to subsurface technology [14]. For a detailed review of the field, the reader is referred to the following excellent references [15, 16, 2, 3], as well as Gary Olhoeft's website [4]. This website contains detailed and up-to-date GPR information that includes a very comprehensive bibliography of GPR references.

The most common method of implementing a GPR system is the 'video pulse' or so-called baseband modulation. A number of alternative implementations of GPR sensors do exist. However, these are mostly limited to the domain of academic and government research institutes. One such technique is the stepped frequency continuous wave (SFCW) GPR. While the latter technique has been investigated since the early seventies [17], there are still very few companies that have commercially viable equipment [18]. This is typically due to the high cost and complexity of SFCW GPRs. Over the last decade the cost of RF technologies (fast switching synthesizers and low noise receiver components) has decreased considerably, making it more feasible to develop SFCW GPR. In addition the availability of fast, low cost signal processors has contributed to the growing interest in this implementation of GPR [19, 20, 21, 22, 23].

The primary goal of any GPR sensor is to detect and identify subsurface features. Many researchers have shown the importance of polarimetric information to aid in achieving this goal [24, 2, 25]. However, little attention has been placed on the extraction of the polarimetric information from the measured GPR data. This thesis focuses, primarily, on the extraction of polarimetric features from a fully polarimetric SFCW GPR sensor. Since the GPR sensor plays an important role in producing the data, aspects of the hardware development are also presented.

1.1 Problem Description

Before considering the objectives and approach taken in this thesis, it is important to understand the scope of the GPR problem. In the thesis, the term Ground Penetrating Radar is used to maintain consistency with the literature. However, radar is a very limiting term when applied to this technology, since it is simply an acronym for RAdio Detection And Ranging [26]. The remote sensing equipment which strives to 'see' underground is far more than an electromagnetic sensor designed to detect and determine distance to some subsurface feature. The purpose of these instruments is to provide information which can be used to determine the subsurface structure and location and ultimately lead to the identification of the subsurface feature.

A GPR sensor is required to provide information which will allow the user to extract the geometrical and physical properties of the targets. This is an extremely tough requirement, especially when one considers the limited amount of information provided by most GPRs. To understand the scope of this problem, consider the GPR measurement scenario for a single target buried in some media as is shown in Figure 1.1

Even though this is not a typical GPR scenario, it does serve to convey the fundamental principles of GPR imaging. Figure 1.1 shows a spherical target buried in some medium. For simplicity only the imaging of the target will be considered. Consider some GPR sensor situated a distance r metres from a target buried in a lossy isotropic medium and located at a Cartesian coordinate (x', y', z'). At some time, t, the radar transmits some radar waveform, $v_{tx}(t)$. This may be one of the waveforms described by numerous radar [27] and communication texts [28]. The electromagnetic energy propagates through the medium, reflects off the target and travels back to the GPR sensor. The received signal would be a convolution of the transmitted pulse with the impulse response of the antenna (gain, beam pattern and frequency dependence) $(g(t))$ the response of the subsurface medium (dispersion, attenuation and scattering losses), $(m(t))$ and the impulse response of the target $(T(t))$, such that

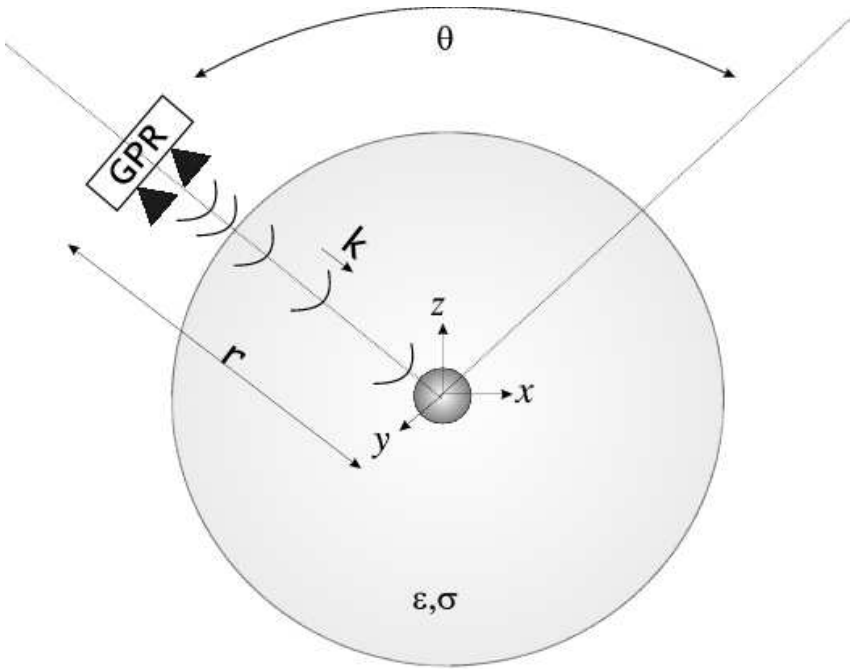

Figure 1.1: View of the GPR problem space

$$v_{rx}(t) = v_{tx}(t-\tau) \circledast g(t) \circledast m(t) \circledast T(t) \circledast m(t) \circledast g(t) \tag{1.1}$$

Both the time delay τ (which is related to the distance to the scatterer) and the impulse response of the target $T(t)$ can be extracted from the received signal. To extract the target impulse response from the received waveform, information about the properties of the medium, the transmit and receive antenna characteristics as well as the transmit waveform is needed. The time delay, τ is the two way time delay of the received waveform and is related to distance between the radar and the target by $\tau = 2\frac{r}{v}$ seconds - where v is the velocity in the medium ($\mathrm{m.s^{-1}}$) and r is the distance between the GPR and the target. The impulse response $T(t)$ can be used to provide unique information about the target. This information can either be viewed as range profiles on an A-scope display or alternatively fitted to some model to determine unique features to recognize the target. For example, if a model for the target scattering mechanisms could be derived, the measured scattered data ($T(t)$) could be fitted to the model to ob-

tain estimates for the parameters describing the model. This is the approach taken in this thesis.

An important point to note is that the transmit waveform acts simply as an information carrier that samples the impulse response (or reflectivity profile [29, 30]) of the target. Hence in deciding what signal to transmit one must consider a waveform that will maximize the information returned from the target. Various researchers have shown that the Stepped Frequency Continuous Wave modulation offers greater mean transmit power, spectral control, sensitivity and dynamic range than equivalent modulation systems [31, 3]. Since convolution in the time domain is multiplication in the frequency domain, choosing a transmit waveform with a greater bandwidth will sample more of the impulse response of the target. In addition illuminating the target for an extended period of time will provide more power on the target which can result in more signal power at the receiver.

In the above argument only the case of viewing the target from a single illumination angle has been considered. If the radar is moved over an azimuth angle θ, the target scattering parameters are sampled over a greater number of illumination angles - providing more information regarding the target. Similarly, the radar can be rotated about the elevation angles ϕ and the complete three dimensional scattering from the target can be captured.

Based on a knowledge of the measurement setup and properties of the medium, a three dimensional image of the subsurface can be created. By illuminating the target with an orthogonal polarization basis, it is possible to capture the complete polarimetric response of the target. This provides an additional set of information to characterize the target.

Since most GPR applications require one to locate, detect and to identify subsurface features and then possibly relate the data to some physical phenomena - the more information that the sensor captures the greater the chance of solving the problem.

Practically, the information captured from the target is limited by the properties

of the media (σ, ε). Most subsurface media will exhibit increased losses with increased frequency. This places a practical limit on the maximum bandwidth of the transmit waveform. In addition it is only possible to sample a target over a limited set of azimuth and elevation angles. The GPR sensor information available to identify the target, is thus limited to a fraction of the target impulse response.

1.2 Thesis Objectives

The objective of this thesis is to develop a signal processing technique to extract polarimetric feature vectors from Stepped Frequency Continuous Wave (SFCW) GPR data. Since the sensor determines the quality of the measured data, and its cost and size the usability of the sensor, it is clear that it would be necessary to investigate the development of low cost, compact and low power SFCW GPR hardware.

1.3 Approach

It is important to note that this thesis approaches the data modelling based on the requirements to use computationally efficient algorithms to determine the parameters of the model. These models then provide better understanding of the signal processing techniques as applied to SFCW GPR, which is often ignored in the literature [2]. Some may argue that one should increase the complexity of the model by solving Maxwell's equations using the various mathematical solutions. However, the problem of determining these model parameters is computationally extensive requiring many hours of computer time with current technology and hence not practically viable. In addition solutions are not always guaranteed. The author also believes that it is important to understand a simpler problem before increasing its complexity.

This section details the approach taken to meet the objectives of the thesis.

1.3.1 Signal Processing

Currently most SFCW GPR systems use the Inverse Discrete Fourier Transform (IDFT) [32, 2] to transform the spatial frequency domain data into the time domain, in order to create synthetic range (reflectivity) profiles [27]. The reflectivity profile is simply the impulse response of the complete radar system (including the target space). In an attempt to improve the radar resolution, various GPR researchers have used so called *super-resolution* techniques [33] to overcome the observed limitations of the IDFT processing [2, 3, 34]. Resolution itself is often a dangerous measure of the GPR performance since it only describes how the radar bandwidth relates to the width of the radar impulse response (see Appendix B for a detailed discussion of this topic). A better way to understand *Super-resolution* techniques is to consider that most of these techniques are based on parameter estimation algorithms that provide computationally efficient algorithms to extract parameters from the assumed model that describes the data. When using these techniques, most researchers seem only to present an understanding of the processing from a signal processing point of view and provide little or no information on how these techniques relate to the interaction of the electromagnetic signals between the medium and target.

The development of a simple model for signal processing based on the underlying electromagnetics is an area of SFCW GPR research which has been greatly ignored [17, 35, 36, 37]. In this thesis a single polarization signal processing model is developed based on the electromagnetic propagation in a lossy medium. It is shown that for low loss materials, the wavenumber in the media can be approximated by a linear function of frequency. Using this approximation together with SFCW modulation theory, this model is shown to be equivalent to the exponential model found in signal processing theory [33, 38, 39, 40]. This model not only provides the important link to the exponential modelling theory found in signal processing literature, but also provides valuable insight into the extraction of subsurface parameters. Numerous techniques exist to extract the parameters from the exponential model. Chiang [40] has shown that most of these techniques are equivalent and suggests the Matrix Pencil-of-Function Method (MPM) for

best performance in noisy data [40].

Single polarization measurements are limited since they only provide information about the projection of the reflected EM wave onto the antenna polarization. The use of polarimetry in GPR is not new, and has been shown to provide valuable additional radar target information [24, 25, 2, 23, 41]. For this reason, the single polarization model is extended to a fully polarimetric SFCW GPR model. A multi-snapshot extension of the MPM method is used to extract estimates for the scattering matrix from the raw radar data [40].

The theory of polarimetry is used to transform the measured scattering matrix to the Huynen diagonal matrix - providing feature vectors which can be divided into parameters that are independent and dependent of the properties of the medium. This is similar to the information used by Higgins [41]. However, a far more detailed analysis is provided. The performance of the algorithm is investigated for varying conductive and dielectric losses. The algorithms are also applied to measured data captured with the radar developed in this thesis and laboratory equipment.

1.3.2 Hardware Design

The success of SFCW GPR technology is dependent on the availability of cost effective and portable hardware. Currently there are only two known companies that commercially sell SFCW GPRs - however they do not seem to have a large market presence [18, 42]. In addition, the current academic GPR systems are large and bulky[21, 23]. This is due mostly to the high cost and complexity of the systems. These issues are addressed here by designing a system that is low cost with a simple architecture, that allows for the construction of small, compact and low power systems. The radar uses a dual synthesizer heterodyne architecture. This effectively reduces the problem of RF harmonics to filtering at a single IF. Careful design and novel insight ensures that the phase at the IF is coherent with the reference oscillator without the requirements of a second reference channel. The IF is undersampled and IQ demodulated using a simple

and fast coherent demodulation technique. The designed radar system operates over a 200-1600 MHz bandwidth. The radar is implemented using off-the-shelf RF and digital components. It is small, compact and low power (0.5 A at 24 V). It connects via a fibre optic link to a portable computer. A graphical user interface has been written to provide real time processing and display of the received data. The antenna used is broadband bowtie structure. Measurements of various targets were performed and these results are presented.

1.4 Thesis Overview

Chapter 2 details the development of a subsurface radar model, based on the considerations of both the scattering targets and the propagation of EM waves in a lossy medium. This model is related to the exponential model found in signal processing theory. The determination of these parameters from measured data is shown to be a least squares estimation problem. The Matrix Pencil-of-Function Method (MPM) is used to extract the model parameters from the measured data. The GPR model is also used to understand the Inverse Discrete Fourier Transform when used as a parameter estimation technique for SFCW GPR. Simulations are presented that examine the performance of the MPM algorithm for targets buried in a medium with increasing conductive and dielectric losses. The algorithm is also applied to real radar data captured with the radar developed in this thesis.

In **Chapter 3** the single polarization subsurface model is extended to a fully polarimetric SFCW GPR model. This model is related to the multi-dimensional exponential model found in signal processing theory. The MPM algorithm is used to extract the scattering matrix parameters from the raw stepped frequency data. The Huynen target parameters are extracted from estimated scattering matrices. These parameters relate to various target scattering measurements. They are categorized into medium dependent and independent target parameters. Simulations are performed to examine the performance of the algorithm for increasing conductive and dielectric losses. The algorithms are also applied to

measured data of a number of targets buried a few centimeters below the ground surface.

The design and development of a SFCW radar is presented in **Chapter 4**. The emphasis of the chapter is to provide an overview of the system and hardware design of a 200 MHz to 1600 MHz radar sensor (excluding the antennas). It focuses on the fundamental aspects of the design, highlighting the various novel techniques which simplify and enhance the performance of this radar. Results of various targets are presented.

Finally in **Chapter 5** conclusions are drawn and future work is discussed.

1.5 Statement of Originality

The candidates original contributions in this thesis are summarized as follows.

- The development of a signal processing model based on linear approximations to the wavenumber in the medium, and relating the model to the exponential model found in signal processing theory. Previous GPR research into *Super-resolution* techniques have simply applied algorithms to measured and simulated data and observed the results. Chapter 2 provides a detailed theoretical development of the underlying theory for the use of these techniques on SFCW GPR data. The MPM algorithm is used to extract the model parameters from the measured data. The General Pencil-of-Function (GPOF) algorithm has been applied to a Frequency Modulated Continuous Wave GPR by Hauschild [34], however this was a few years after which the author originally publish the work [43]. In addition Hauschild [34] simply applied the GPOF algorithm, without the fundamental understandings provided in this document.

- The extension of the single polarization model to a fully polarimetric SFCW GPR model, and relating the model to a multidimensional exponential signal processing model. The multi-snapshort MPM algorithm is used to

extract the scattering matrix from the measured data. The Huynen target invariant parameters are extracted from the estimated scattering matrix. Similar parameters have been used by Higgins to serve as feature vectors for recognizing unexploded ordinances [41], however this was a few years after the idea was originally published by the author [44, 43].

- The development of a low cost and small SFCW Ground Penetrating Radar. The initial results of this work were published at a Piers conference in 1998 [45]. The system was completely developed by the author independently of other SFCW GPR technology. The system presented in this thesis was a second generation SFCW GPR developed with the aid of two masters students [46, 47]. Its primary novelty lies in the use of off-the-shelf mobile communication technology, a single channel synchronous demodulator and a simple computationally efficient IQ demodulator.

Chapter 2

Single Polarization GPR Model Based Processing

2.1 Introduction

An important requirement of any Ground Penetrating Radar system is the ability to identify or determine the shape, size and material composition of buried targets. This is essential to separate the target return echoes from the radar reflections from rocks, subsurface layers, roots and other radar clutter. In order to achieve this it is necessary to relate the target returns to the physical parameters describing the target.

The development of a simple model for signal processing based on the underlying electromagnetic principles, is an area of Stepped Frequency Continuous Wave Ground Penetrating Radar research which has been greatly ignored [17, 35, 36, 37]. Current models are based more on signal processing demands, rudimentary free space electromagnetic (EM) propagation and radar modulation theory. There are occasions where the properties of the subsurface medium are addressed [35, 3]. However, these are related very simplistically to the signal processing. Models are particularly important in Stepped Frequency Continuous Wave Radar when transforming the raw frequency data into the spatial domain.

In this chapter a more complete signal processing model is developed based on the radar geometry and approximations to electromagnetic propagation in a lossy medium. The model is shown to be equivalent to the exponential model found in signal processing theory [33, 38, 39]. The exponential model parameters are clearly related to the physical electromagnetic model derived in the thesis. This enhances the understanding of applying *Super-resolution* techniques to SFCW GPR data. The MPM algorithm is used to extract the exponential model parameters from the raw noisy data.

The chapter begins by providing a motivation for the development of the signal processing model. This is followed by the development of the model for GPR using any modulation scheme. Section 2.5 uses the model to describe the received signal for a SFCW GPR. These equations are related to the exponential model found in parameter estimation theory. The MPM algorithm, which is used to extract the model parameters, is described. Simulations are presented to examine the performance of the MPM algorithm on simulated data for targets buried in a medium with varying ionic and dielectric conductivity. Finally results for real GPR measurements are presented.

2.2 Contributions

In this chapter the following original contributions are made:

- The development of a single polarization GPR model based on linear approximations to the wavenumber in the medium. Depolarization due to the medium and/or target is not considered.

- The extension of the model to describe the received signal for a SFCW GPR.

- The comparison of the GPR model parameters with the model parameters of an exponential model found in signal processing theory.

- The use of the Matrix Pencil-of-Function Method to extract the target parameters from the raw SFCW GPR data.

2.3 Motivation

Chapter 1 provided an overall understanding of various fundamental concepts of GPR. GPR processing involves extracting the impulse response of the target. Ideally one would like to relate this target impulse response to the physical target parameters. These can be used as features in automatic target recognition problems. One approach is to solve the inverse scattering problem [48]. However this is a difficult problem that is computationally extensive with many unknown parameters. Another approach is to consider simpler models that relate certain target characteristics to the target impulse response. The reduced model complexity allows one to use more computationally efficient algorithms to extract the model parameters. A classic example is the point target response in radar theory [27] or the exponential models used by Moses [39] for automatic target recognition.

Models also provide valuable insight into understanding the behavior and performance of a SFCW GPR system without the complexity of determining closed form analytic solutions or performing complex simulations. By providing a simple model one is providing an understanding. Models have been used in GPR to provide basic understanding of radar propagation and the prediction of radar performance [3, 49, 50]. Models are particularly important in SFCW waveforms when transforming the raw frequency data into the spatial domain. This is an area of SFCW literature [32, 35, 42] which is often neglected.

2.4 Simple GPR Scattering Model

This section develops a single polarization GPR model for depth profiles, based on the radar/target geometry and approximations to the propagation of a trans-

verse electromagnetic (TEM) plane wave in a lossy medium.

Consider a GPR sensor situated at the ground/air interface and some target buried at r metres below the surface. Figure 2.1 shows this radar/target geometry.

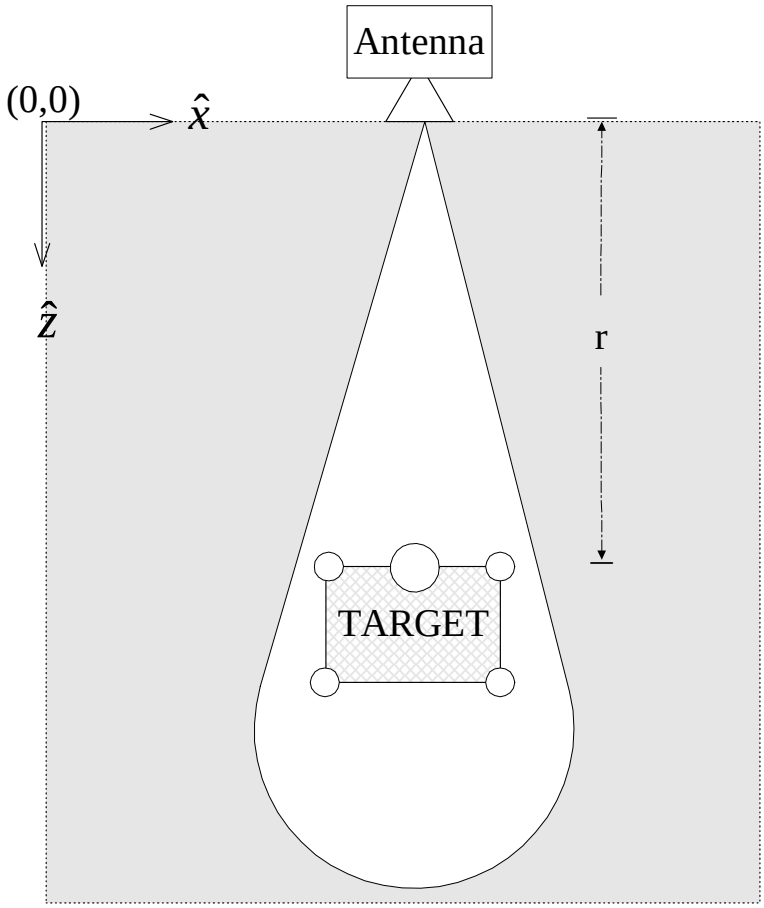

Figure 2.1: GPR/target geometry

The model requires the following assumptions:

- *Soil medium* consists of a single layer. The target is buried in this layer.
- The soil is a linear, isotropic and low loss medium and can be represented by a constant complex permittivity ε_r, ionic conductivity σ_m and the relative permeability $\mu_r = 1$ (non magnetic material).

- The radar is located at the air ground interface or can be buried in the medium.
- The target's radar cross-section, $\sigma_{\{xy\}}(\omega)$ is a function of frequency and polarisation defined by the polarisation basis $\{xy\}$.
- There are no target multiple reflections.

In the rest of the section these assumptions will be used to develop a simple electromagnetic model.

2.4.1 Approximation for an EM Wave Propagating in a Lossy Medium

Consider a plane wave propagating through a linear, homogeneous and non-dispersive medium which can be characterized by its complex permittivity ε and complex conductivity σ. The electric far field $\mathbf{E}$[1] at a distance r meters from the source is given by Equation 2.1,

$$\mathbf{E}(\mathbf{r}) = \mathrm{Re}\left[\frac{\mathbf{E}_o}{|\mathbf{r}|}e^{j\left(\omega t - k_m \hat{\mathbf{k}}\cdot\mathbf{r}\right)}\right] \tag{2.1}$$

where,

- $\mathbf{r} = \hat{\mathbf{x}}x + \hat{\mathbf{y}}y + \hat{\mathbf{z}}z$ is the displacement vector and $r = |\mathbf{r}| = \sqrt{x^2 + y^2 + z^2}$
- $\hat{\mathbf{k}}$ is the unit direction vector of k_m
- k_m is wavenumber in the medium described by,

$$k_m = \frac{\omega}{v}\sqrt{1 - j\tan\delta} \tag{2.2}$$

- v is the velocity in the medium, ω is the angular frequency and $\tan\delta$ is the loss tangent of the EM wave in the medium.

[1] The magnetic field $\mathbf{H}$ can simply be determined from $\mathbf{E}$ using Maxwell's equations [51].

Writing $\varepsilon = \varepsilon^{'} - j\varepsilon^{''}$, $\tan\delta$ can be expressed as:

$$\tan\delta = \frac{\sigma^{'} + \omega\varepsilon^{''}}{\omega\varepsilon^{'}} \tag{2.3}$$

From Equation 2.2 it can be seen that for a linear, homogeneous and non-dispersive medium, k_m is a non-linear function of ω, $\tan\delta$ and v. Since a radar determines range information by transmitting energy over a frequency band, non-linearities in ω will distort the returned echoes from the targets. It is possible to make certain simplifications to Equation 2.2 based on either the magnitude of $\tan\delta$ or $\frac{\omega}{v}$.

Writing $k_m = \beta_m - j\alpha_m$ and performing a Maclaurin series expansion on Equation 2.2, α_m and β_m can be written as

$$\alpha_m = -\sum_{n=0}^{n=\infty} \frac{\mathrm{Im}\left(f^{(n)}(0)\right)}{n!} (\tan\delta)^n \frac{\omega}{v} \tag{2.4a}$$

$$\beta_m = \sum_{n=0}^{n=\infty} \frac{\mathrm{Re}\left(f^{(n)}(0)\right)}{n!} (\tan\delta)^n \frac{\omega}{v} \tag{2.4b}$$

where $f(x) = \sqrt{1 - jx}$ and $k_m = \beta_m - j\alpha_m$.

The next few sections derive some of the standard EM propagation models used in GPR literature. Finally the low loss constant Q attenuation model [52, 49] is extended to a more general model which is only limited by the conductive losses in the medium.

Lossless Media

The simplest approximation for α_m and β_m is to assume that the medium is lossless. Under these conditions $\sigma_m = 0$ S/m, $\varepsilon^{''} = 0$ F/m and hence $\tan\delta = 0$. Taking only the first term of β_m, Equation 2.1 can be simplified as shown in Equation 2.5.

$$\mathbf{E}(\mathbf{r}) \approx \frac{\mathbf{E}_o}{|\mathbf{r}|} \cos\left(\omega t - \frac{\omega}{v}\hat{\mathbf{k}} \cdot \mathbf{r}\right) \tag{2.5}$$

Low Loss Media

A more appropriate model is to include the first term of α_m as well as the first term of β_m from Equation 2.4a and 2.4b,

$$\alpha_m \approx -\frac{1}{2}\frac{\omega}{v}\tan\delta \approx -\frac{1}{2}\frac{\omega}{v}\frac{\varepsilon''}{\varepsilon'} - \frac{1}{2}\frac{\sigma'}{v\varepsilon'} \tag{2.6a}$$

$$\beta_m \approx \frac{\omega}{v} \tag{2.6b}$$

Hence, the electric field described by Equation 2.1 can be re-written as shown in Equation 2.7.

$$\mathbf{E}(\mathbf{r}) \approx \frac{\mathbf{E}_o}{|\mathbf{r}|} e^{-\frac{1}{2}\frac{\omega}{v}\tan(\delta)\hat{\mathbf{k}}\cdot\mathbf{r}} \cos\left(\omega t - \frac{\omega}{v}\hat{\mathbf{k}}\cdot\mathbf{r}\right) \tag{2.7}$$

For these simplifications to be valid, $\tan\delta < \zeta$, where ζ is chosen to ensure the desired model accuracy. The values for ζ can be obtained from Figure 2.2, which shows the model error of α_m and β_m as a function of $\tan\delta$. The model error is represented as a percentage deviation from the theoretical value using the formula for k_m.

Figure 2.2 shows that the model error is less than 10 % for $\tan\delta < 1$. This first order approximation to k_m is the constant Q attenuation model described by Turner [49] which compares well with attenuation in real geological materials over the radar bandwidth. This model was also discussed by Noon [3] and used by him in a later paper [53] to analyze antenna ring-down (damping of antenna ringing) for stepped frequency GPRs. If the losses in the medium are purely conductive losses, then Equation 2.4a reduces to

$$\alpha_m \approx -\frac{1}{2}\frac{\sigma'}{v\varepsilon_e} \tag{2.8}$$

Equation 2.8 implies that α_m is a constant. This approximation is often used to remove material losses and enhance the dynamic range of the GPR image [54].

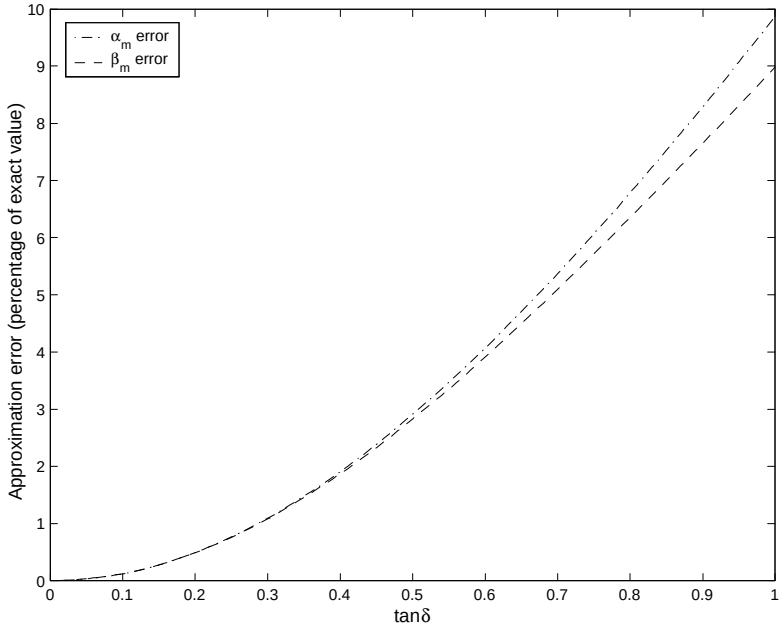

Figure 2.2: Plot of the percentage model error as a function of $\tan\delta$

High Frequency and Low σ_m Approximation to α_m and β_m in a Lossy Medium

This section extends the low-loss or constant Q attenuation model described by Turner [49] to a model which has important implications for signal processing theory developed later in the chapter. It is possible to derive a more general approximation to α_m and β_m at high operating frequency or low σ_m, by considering the binomial expansion of $\tan\delta$ described in Equation 2.4a and 2.4b. Assuming that $\frac{1}{\omega v}\left(\frac{\sigma}{\epsilon'}\right)^2 << 1$ and $\tan\delta < 1$, it can be shown that (Appendix A),

$$\alpha_m \approx -\sum_{n=0}^{N} \mathrm{Im}\left(\Psi_n\right)\psi^n\frac{\omega}{v} - \sum_{n=0}^{N-1} \mathrm{Im}\left(\Psi_n\right) n\psi^n\frac{\sigma^{'}}{\varepsilon^{''}v} \tag{2.9}$$

$$\beta_m \approx \sum_{n=0}^{N} \mathrm{Re}\left(\Psi_n\right)\psi^n\frac{\omega}{v} + \sum_{n=0}^{N-1} \mathrm{Re}\left(\Psi_n\right) n\psi^n\frac{\sigma^{'}}{\varepsilon^{''}v} \tag{2.10}$$

where

- $\psi = \frac{\epsilon''}{\epsilon'}$.
- $\Psi_n = \frac{f^{(n)}(0)}{n!}$ and $f^n(0)$ is the n^{th} derivative of $f(x)$ evaluated at $x = 0$.
- $f(x) = \sqrt{1 - jx}$.

Note that the Maclaurin series has been truncated to N terms of k_m, where N is chosen to ensure a certain model accuracy. The choice of N depends on $\left(\frac{\epsilon''}{\epsilon'}\right)^n \frac{\omega}{v}$. For $N = 0$, Equation 2.9 and 2.10 describe α_m and β_m for a lossless medium, while for $N = 1$ the wavenumber approximations are the same as for constant Q model [49]. The choice of N is less important than the dependence of α_m and β_m on frequency. Noting the assumption that $\varepsilon', \varepsilon''$ and σ'_m are independent of frequency, Equations 2.9 and 2.10 can be simplified to,

$$\alpha_m(\omega) \approx \alpha_{m1}\frac{\omega}{v} + \alpha_{m2} \tag{2.11a}$$

$$\beta_m(\omega) \approx \beta_{m1}\frac{\omega}{v} + \beta_{m2} \tag{2.11b}$$

This shows that both α_m and β_m are linear functions of frequency. This is an important result, particularly for the signal processing theory developed in Section 2.5. Figure 2.3 plots the percentage model error and two way propagation loss as a function of medium conductivity. The model error is calculated by determining the maximum error between Equation 2.2 and a linear function that best fits (in a least squares sense) Equation 2.2.

In general soil permittivity will vary with frequency [55, 56, 57, 58, 59, 60, 61, 62, 63] and some media will have a significant magnetic response [50]. However the assumptions used to derive this model still provide valuable insight into the performance and processing in a GPR system. In addition, these assumptions are used extensively in GPR studies [3, 35, 2] and hence provide a common framework for comparing the techniques proposed in the chapter) with previous work [3, 35, 2].

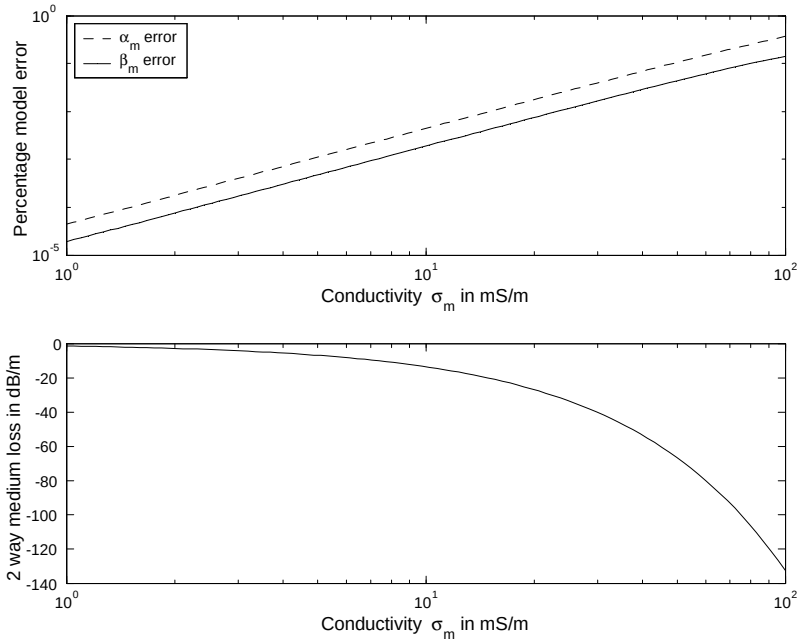

Figure 2.3: Plot of percentage model error and 2 way medium loss as a function of conductivity (σ_m)

2.4.2 Scattering from a Target

The relationship between physical target parameters and the target impulse response ($T(t)$) is typically very complex. Closed form solutions only exist for simple targets. Numerical techniques can be used to examine the scattering from more complex targets, however solving the inverse scattering problem for these target spaces is computationally intensive and difficult [48, 24]. Various models have appeared in the literature to describe scattering mechanisms. The simplest model is the point target scatterer [26], used in most radar applications. The model assumes that the target can be modelled as the sum of a number of point target reflectors, whose radar cross section (RCS) is constant with frequency.

Researchers from Ohio State University [64, 40] use the GTD (Geometric Theory of Diffraction) model to estimate the scattering from a target with dimensions greater than a wavelength. GTD predicts that the scattered electric field will have a $(jf)^{\alpha}$ dependence, where α is an integer multiple of a $\frac{1}{2}$ [64]. Hence the radar cross-section ($\sigma_{\{xy\}}$) of the target can be described as

$$\sigma_{\{xy\}} = \sigma^{\circ}_{\{xy\}} \left(\frac{k}{k_o} \right)^{\alpha} \tag{2.12}$$

The reference wavenumber, k_o ($k_o \rightarrow k(\omega_o)$) is chosen to ensure consistency of units. Hurst [65] reports that there are several types of scattering mechanisms which cannot be adequately treated using the GTD model. He suggests that in most practical cases the RCS can be modelled using a damped exponential.

$$\sigma_{\{xy\}} = \sigma^{\circ}_{\{xy\}} \exp\left(\gamma^{'}_{\{xy\}} k_m \right) \tag{2.13}$$

Hurst showed that the exponential model could be used to locate the corners of a square plate for frequencies such that $0.8 < \frac{a}{\lambda} < 4.2$, where a is the width of the plate [65]. Chiang [40] showed that this model is a first order approximation to the GTD model. The scattering coefficient of the target for a particular polarization basis defined by $\{xy\}$, is related to the RCS by $\left| s_{\{xy\}} \right| = \sqrt{\sigma_{\{xy\}}}$. Noting that $\gamma^{'}_{\{xy\}} = 2\gamma_{\{xy\}}$, $s_{\{xy\}}$ can be written as,

$$s_{\{xy\}} = s_{\{xy\}o} \exp\left(\gamma_{\{xy\}} k_m\right) \tag{2.14}$$

where $\gamma_{\{xy\}}$ is the target damping coefficient in the medium and $s_{\{xy\}o} = \sqrt{\sigma_o} \exp\left(j\tau_{\{xy\}}\right)$.

2.4.3 Received Signal at GPR

Consider a target at a distance d metres beneath the surface, illuminated by a horizontally polarized electric field E_x^t. The received electric field (E_x^r) at the radar origin, can then be described by Equation 2.15

$$E_x^r(\omega, d) \approx \mathrm{Re}\left\{ \frac{s_x E_{x0}^t}{d^2} \exp\left[-2\alpha_m(\omega)d\right] \exp\left[j\omega t - 2\beta_m(\omega)d\right] \right\} \tag{2.15}$$

Given that the wavelength is small compared to the size of the target space[2], the latter can be modelled as a number of dominant scattering centres situated at discrete locations from the radar (as shown in Figure 2.1). The received electric field can be expressed as,

$$E_x^r(\omega) \approx \sum_{p=0}^{P-1} E_x^t(\omega, d_p) \tag{2.16}$$

where

- $E_x^r \rightarrow E_x^r(\omega)$ is the received electric field at the radar antenna
- P is the number of discrete targets.
- $E_x^r(\omega, d_p)$ is the approximate electric field contribution from the p^{th} target at position d_p.

[2]The target space refers to the subsurface region that is being probed

2.5 SFCW Modulation

The model developed in the previous section is a general propagation model that is independent of the radar system modulation. This section extends the model to include the SFCW modulation scheme.

A SFCW radar determines the distance to a target by sequentially measuring the coherent electromagnetic returns from a target for a number of stepped operating frequencies [43].

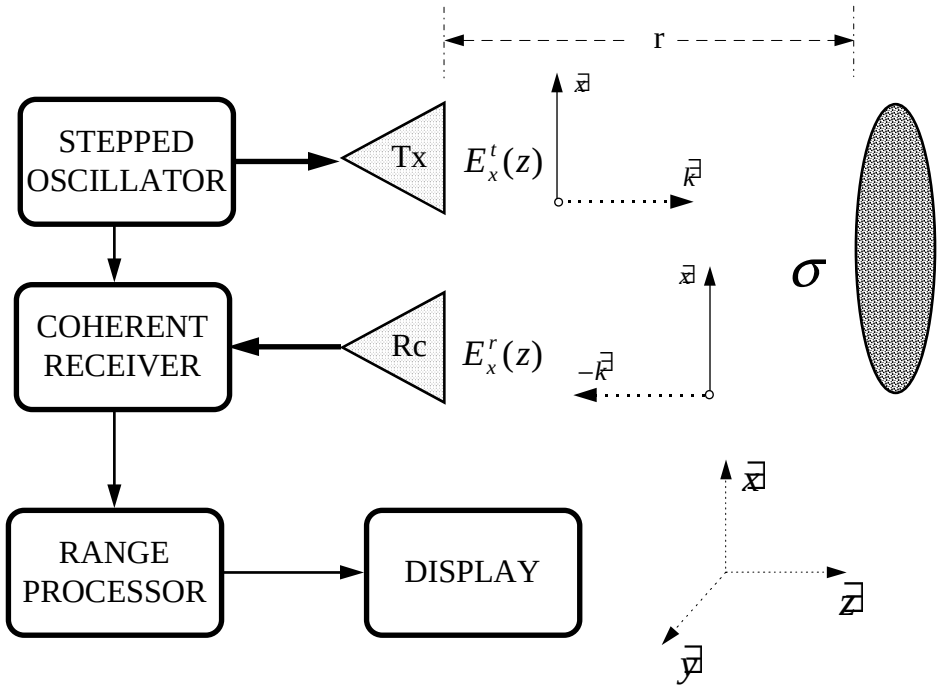

Figure 2.4: Conceptual block diagram of a SFCW GPR

Conceptually the radar is made up of three main modules:

1. **A step-frequency oscillator:** This module is responsible for generating the N frequency steps, with a frequency step size of Δf , starting at f_o and extending over the required measurement bandwidth.

2. **The coherent receiver***:* This module mixes the required received signal down to baseband and then measures the amplitude of the reflected target backscatter. A SFCW radar then uses a quadrature modulation scheme to determine both the in-phase (I) and quadrature (Q) components of the reflected target energy [35].

3. **A range/target extractor:** This module transforms the raw data from the frequency domain to the spatial domain or extracts the target parameters.

The electric field at the receive antenna for a single polarization and P discrete target reflectors can be determined by substituting Equation 2.15 into Equation 2.16,

$$E_x^r(\omega) \approx \sum_{p=1}^{P-1} \mathrm{Re}\left\{ \begin{array}{c} \frac{(s_p)_x E_{x0}^t}{d_u^2} \exp\left[-2\left(\alpha_{m1}\frac{\omega}{v} + \alpha_{m2}\right) d_p\right] \times \\ \exp\left[j\omega t - 2\left(\beta_{m1}\frac{\omega}{v} d_p + \beta_{m2}\right) d_p\right] \end{array} \right\} \tag{2.17}$$

The received electric field $E_x^r(\omega)$ is then converted to voltage by the receiver. In the coherent receiver the signal is then mixed down to baseband using an IQ (inphase/quadrature) demodulator. Since the received signal is bandlimited, the I and Q channels can be combined to form an analytic signal [28]. Including the effects of the thermal noise at the input to the radar receiver, modelled as a zero mean Gaussian process ($n_x(f)$), the received signal at the input to the radar processor for a single polarization is given by:

$$\begin{aligned} v_x^r(f) \approx G_s(f) G_{tx}(f) G_{rx}(f) v_{xo}^t \sum_{p=1}^{P-1} \frac{(s_p)_x}{d_p^2} \times \\ \exp\left[-4\pi\alpha_{m1}\frac{f}{v} d_p - 2\alpha_{m2} d_p\right] \times \\ \exp\left[-j\left(\frac{4\pi f}{v}\beta_{m1} d_p + 2\beta_{m2} d_p\right)\right] + n_x(f) \end{aligned} \tag{2.18}$$

where

- $G_{tx}(f)$ and $G_{rx}(f)$ are the transmit and receive antenna voltage gains.
- $G_s(f)$ is the radar electronics voltage gain.
- v_{xo}^t is the RMS voltage at the terminals of the transmit antenna.

It is possible to remove the effects of the system and antenna gain responses from the measured data by dividing the received data $v_x^r(f)$ by the measured antenna and radar electronics response,

$$v_x^{'r}(f) \approx \frac{v_x^r(f)}{v_{xo}^t G_s(f) G_{tx}(f) G_{rx}(f)} \tag{2.19}$$

Consider the transmission of N discrete frequencies over a bandwidth B from a start frequency f_L to $f_L + B$, such that the current frequency $f = f_o + n\Delta f$. Substituting these parameters into Equation 2.18 and 2.19, yields the sampled voltage at the receiver, described by Equation 2.20.

$$\begin{aligned} v_x^{'r}[n] \approx \sum_{p=1}^{P-1} \frac{(s_p)_x}{d_p^2} \exp\left(-2\alpha_{m2} d_p\right) \times \\ \exp\left(-4\pi\alpha_{m1} \frac{f_o + n\Delta f}{v} d_p\right) \times \\ \exp\left(-j\left(4\pi \frac{f_o + n\Delta f}{v} \beta_{m1} d_p + 2\beta_{m2} d_p\right)\right) + n_x^{'}[n] \end{aligned} \tag{2.20}$$

Equation 2.20 is simply the standard exponential model with noise, as found in the signal processing literature [33, 39, 66, 67, 68, 69]. This can be seen more clearly by rewriting Equation 2.20 as,

$$v_x^{'r}[n] \approx y[n] + n_x^{'}[n] \tag{2.21}$$

where the exponential model is given by $y[n]$,

$$y[n] = \sum_{p=0}^{P-1} (b_p) z_p^n \tag{2.22}$$

and

$$b_p = A_p \exp(j\theta_p) \tag{2.23}$$

$$z_p = \exp\left[(\lambda_p + j2\pi r_p)\Delta r\right] \tag{2.24}$$

and

$$A_p = \frac{|s_p|}{d_p^2} \exp\left(-2\alpha_{m2} d_p + 2\pi\alpha_{m1} r_o d_p\right) \exp\left(\gamma_p \beta_{m2} - \pi\gamma_p \beta_{m1} r_o\right) \tag{2.25}$$

$$\theta_p = \angle b_p = -\tau_m - 2\beta_{m2} d_p + 2\pi\beta_{m1} r_o d_p - \gamma_p \alpha_{m2} + \pi\gamma_p \alpha_{m1} r_o \tag{2.26}$$

$$\lambda_p = 2\pi\alpha_{m1} d_u - \pi\gamma_p \beta_{m1} \tag{2.27}$$

$$r_p = \beta_{m1} d_p + \frac{1}{2}\gamma_p \alpha_{m1} \tag{2.28}$$

$$\Delta r = -\frac{2\Delta f}{v} \tag{2.29}$$

$$r_o = -\frac{2f_o}{v} \tag{2.30}$$

The parameter A_p is the target amplitude, θ_p is the target absolute phase, λ_p is the target damping factor, d_p is the free space target position and p is the p^{th} target. Given the parameters of the medium, $\alpha_{m1}, \alpha_{m2}, \beta_{m1}$ and β_{m2}, the target damping factor γ_p and scattering amplitude s_p can be determined. Note that the target position d_p is a function of both the model parameter z_p and the target damping parameter, γ_p. One can also define the signal-to-noise ratio for the received signal $v_x^{'r}[n]$ as,

$$SNR = \frac{\sum_{p=0}^{P-1} \sum_{n=0}^{N-1} |y_p[n]|^2}{\sum_{n=0}^{N-1} |n'_x[n]|^2}$$

In Section 2.7 displays the results of simulations using the above model in terms of power into a 50 Ω load measured in dBm and not in terms of the received voltage as derived in this section. The power in dBm, P_{dBm} is related to the root mean square voltage (RMS), v_{RMS} at the receiver with a 50 Ω by the following Equation,

$$P_{dBm} = \frac{v_{RMS}^2}{50}$$

2.6 Parameter Estimation

In the previous section it was shown that the SFCW GPR model relates to the exponential model parameters (Φ_p), where $\Phi_p = (b_p, z_p)$ and $p = 0, 1, \cdots, P-1$. The problem of estimating a parameter Φ_p is a complex non-linear problem. Given the measured data $x[n]$ (for $n = 0, 1, \cdots N-1$) made in the presence of some disturbances (noise $n'_x[n]$), the objective is to find some model $y[n, \Phi_p]$ that estimates the value of $x[n]$ in some sense. The function $y[n, \Phi_p]$ is called the estimator. The value of the function is termed the estimate. The estimation error corresponding to the estimate $y[n, \Phi_p]$ is

$$v_x^r[n]_e \triangleq x[n] - y[n, \Phi_p] \tag{2.31}$$

Given $x[n]$, one needs to determine the model parameters Φ_p. To achieve this goal the likelihood function (or non-Bayesian) approach will be considered. In this case one constructs a likelihood function (LF) of the parameter

$$J(\Phi) \triangleq p(\mathbf{V}|\Phi) \tag{2.32}$$

which measures how *likely* a parameter value is for the observations that are made [70].

A common estimation procedure for non-random parameters is the least squares (LS) method. The LS method chooses the parameter set $\mathbf{\Phi}$ such that the estimated value $y[n, \Phi_p]$ is closest to the measured data $x[n]$ in a least squares (LS) sense, such that

$$J(\mathbf{\Phi}) = \sum_{n=0}^{N-1} \left(x[n] - y[n, \mathbf{\Phi}]\right)^2 \tag{2.33}$$

where $\mathbf{\Phi} = (\Phi_o, \Phi_1, \cdots, \Phi_{P-1})$ and the observation interval is assumed to be $n = 0, 1, \ldots, N-1$ and corresponds to the frequency steps over the measurement bandwidth.

It is important to note that this estimator makes no probabilistic assumptions about the data, and the method is equally valid for both Gaussian and non-Gaussian observation noise $n_x'[n]$ [70]. However, the performance of the estimator ultimately depends on the type of noise. For Gaussian noise the least sqaures estimator (LSE) is equivalent to the maximum likelihood estimate.

Solving for $\mathbf{\Phi}$ is, in general, a complex non-linear LS squared problem, which can be solved with complex and computationally expensive optimization algorithms [40, 71]. The complexity of this problem has led to the development of many computationally efficient, but statistically suboptimal estimation solutions [71]. The use of the exponential model allows one to reduce the complexity of the problem by applying the separability principle [70]. This simply states that one can determine $\mathbf{z}$ and $\mathbf{b}$ independently, where $\mathbf{\Phi} = \{\mathbf{z}, \mathbf{b}\}$**.** For a fixed $\mathbf{z}$, J is quadratic in the complex amplitude vector $\mathbf{b}$, and hence the estimation of $\mathbf{b}$ becomes a linear least square problem solvable using the pseudo-inverse [64]. The model, however is still non-linear in $\mathbf{z}$. A number of methods exist which allow one to determine the parameter $\mathbf{z}$**,** which do not rely on complex optimization

algorithms [72, 67, 69, 66, 73, 38, 74]. Chiang states that even though these techniques are suboptimal statistical solutions, the statistical accuracy of these methods typically approaches the Cramer-Rao lower bound for moderate data lengths and signal-to-noise ratio [40, 71, 69]

These methods include, subspace-based approaches such as the MUSIC [72] method, subspace-rotation methods (ESPRIT) [75], maximum likelihood methods, minimum norm methods and numerous variants of the Prony method [67, 68, 76]. There have been a number of papers to evaluate the performance of these methods quantitatively [77, 69]. All of these techniques rely on the fact that one can represent Equation 2.22 as a linear combination of its past P samples, known as the linear difference equation [33].

$$\sum_{p=0}^{P} c_p x\left(i-P\right)=0 \qquad i=P,\cdots,N-1 \tag{2.34}$$

where c_p are the coefficients of the characteristic polynomial equations whose solution provides estimates for z_p. By analyzing the data matrices constructed from Equation 2.34, the various estimators solve for z_p in a least squares sense.

In this thesis the Matrix Pencil-of-Function Method (MPM) [73, 69] will be used to determine the poles (z_p). Hua showed that the MPM method is more computationally efficient, less restrictive about the signal poles and less sensitive to noise than the polynomial method [69]. Chiang [40] also showed the equivalence between (T)LS-Prony, Matrix Pencil and State Space methods and suggests the use of the TLS-Method, based on improved computational efficiency and performance over the Prony methods and improved computational efficiency over the State Space Methods. The TLS-MPM is a heuristic extension to the MPM to improve the performance of the MPM method in noise - however no proof is provided for the improved performance. For this reason the MPM method will be used. For theoretical details of the MPM and TLS-MPM the reader is referred to [73, 69, 64, 40]. For completeness, the implementation of the MPM method will be described.

2.6.1 Matrix Pencil-of-Function Method

Consider the following set of measurement vectors,

$$\mathbf{x}_o, \mathbf{x}_1, \ldots, \mathbf{x}_L \tag{2.35}$$

where

$$\mathbf{x}_i = [x_i, x_{i+1}, \ldots, x_{i+N-L-1}]^T \tag{2.36}$$

and L is defined as the pencil parameter. Based on these vectors the MPM defines two matrixes $\mathbf{X}_1$ and $\mathbf{X}_2$ with dimension $(N-L) \times (L+1)$ as

$$\mathbf{X}_1 = \left[\mathbf{x}_{L-1}, \mathbf{x}_{L-2}, \ldots, \mathbf{x}_0\right] \tag{2.37}$$

$$\mathbf{X}_2 = \left[\mathbf{x}_L, \mathbf{x}_{L-1}, \ldots, \mathbf{x}_1\right] \tag{2.38}$$

Chiang [71] suggests a pencil length of $L = \frac{N}{3} > P$, based on first order perturbation analysis. Using Singular Value Decomposition (SVD) the pseudo-inverse $\mathbf{X}_1^+$ of the matrix $\mathbf{X}_1$ can be determined,

$$\mathbf{X}_1^+ = \mathbf{V}\mathbf{D}^{-1}\mathbf{U}^H \tag{2.39}$$

where $U = [\mathbf{u}_1, \mathbf{u}_2, \ldots, \mathbf{u}_L]$, $V = [\mathbf{v}_1, \mathbf{v}_2, \ldots, \mathbf{v}_L]$ (left and right matrix of singular vectors), $D = diag\,[\boldsymbol{\sigma}_1, \boldsymbol{\sigma}_2, \ldots, \boldsymbol{\sigma}_P]$ and H denotes the conjugate transpose. For noisy data the singular values should be chosen to be the P largest values, and the resulting matrix $\mathbf{X}_1^+$ is called the truncated pseudo-inverse of the matrix $\mathbf{X}_1$. The TLS-MPM determines $\mathbf{X}_1^+$ by computing the singular valued decomposition of a matrix $\mathbf{X} = [\mathbf{x}_L|\mathbf{X}]$, since $\mathbf{X}_1$ and $\mathbf{X}_2$ are derived from $\mathbf{X}$**.** This effectively takes into account the noise in both matrices [40, 71].

The complex model parameter z_p (Equation 2.24) can then be determined by calculating the eigenvectors of the matrix $\mathbf{Q}$**,** where

$$\mathbf{Q} = \mathbf{D}^{-1}\mathbf{U}^{H}\mathbf{X}_2\mathbf{V} \tag{2.40}$$

Hua [73] adds that the number of poles P, can be estimated from the decreasing amplitude of the singular values , $\boldsymbol{\varphi}_0 \geq \boldsymbol{\varphi}_1 \geq \cdots \geq \boldsymbol{\varphi}_{P-1} \geq \cdots \geq \boldsymbol{\varphi}_{\min(N-L-1,L-1)}$, since $\boldsymbol{\varphi}_P = \cdots = \boldsymbol{\varphi}_{\min(N-L-1,L-1)} = 0$ for noiseless data. Another way to determine P is to consider that the the singular values represent the energy in each eigenvector. Choosing P such that $\eta(P)$ (Equation 2.41) is larger than a certain threshold close to unity will ensure that most of the information is in the P largest eigenvectors [78]

$$\eta(P) = \frac{\sum_{p=0}^{P-1} \left|\varphi_p\right|^2}{\sum_{p=0}^{\min(N-L-1,L-1)} \left|\varphi_p\right|^2} \tag{2.41}$$

Substituting the poles z_p into Equation 2.22 and rewriting in matrix form, the parameter $\mathbf{b}$ can be determining be solving the matrix equations in a least squared sense,

$$\mathbf{b} = \left(\mathbf{Z}^{H}\mathbf{Z}\right)^{-1}\mathbf{Z}^{H}\mathbf{x}_o \tag{2.42}$$

Given the properties of the medium and assuming the received data has been calibrated as shown in Equation 2.19, it is then possible to determine the target parameters from $\mathbf{b}$ and $\mathbf{z}$.

$$\lambda_p = \frac{1}{\Delta r} \ln |z_p| \tag{2.43}$$

$$r_p = \frac{1}{2\pi\Delta r} \angle z_p \tag{2.44}$$

$$A_p = |b_p| \tag{2.45}$$

$$\theta_p = \angle b_p \tag{2.46}$$

$$d_p = \frac{\beta_{m1}}{\alpha_{m1}^2 + \beta_{m1}^2} r_p + \frac{\alpha_{m1}}{\alpha_{m1}^2 + \beta_{m1}^2} \frac{\lambda_p}{2\pi} \tag{2.47}$$

$$\gamma_p = \frac{1}{\pi\beta_{m1}} \left(2\pi\alpha_{m1} d_p - \lambda_p\right) \tag{2.48}$$

$$\tau_p = \theta_p - 2\beta_{m2} d_p + 2\pi\beta_{m1} r_o d_p - \gamma_p \alpha_{m2} + \pi\gamma_p \alpha_{m1} r_o \tag{2.49}$$

$$s_p = A_p d_p^2 \exp\left(2\alpha_{m2} d_p - 2\pi\alpha_{m1} r_o d_p\right) \exp\left(-\gamma_p \beta_{m2} + \pi\gamma_p \beta_{m1} r_o\right) \tag{2.50}$$

Equations 2.43 - 2.50 provide valuable understanding of the parameters of the exponential signal processing model and how they relate to the GPR model parameters. Equation 2.47 shows that the estimated target position is dependent on the medium parameters and the target damping γ_p (since γ_p is related to λ_p). The target damping is a function of the attenuation in the medium, the propagation constant β_{m1} and the estimated model damping λ_p. The scattering phase and amplitude (τ_p and s_p) are dependent on the medium parameters, as well as the damping factor and position of the target.

2.6.2 Model Error

In Section 2.4.3 is was shown that based on certain approximations to the wave number k_m, the received signal model $v_x^r(f)$ can be can be approximated by,

$$v_x^r(f) \approx G\left(f\right) v_{xo}^t \sum_{p=1}^{P-1} \frac{\left(s_p\right)_x}{d_p^2} \exp\left(-2j\widehat{k}_m d_p\right) \tag{2.51}$$

$$v_x^r(f) \approx G\left(f\right) v_{xo}^t \sum_{p=1}^{P-1} \frac{\left(s_p\right)_x}{d_p^2} \exp\left(-2jk_m d_p\right) \exp\left(-2jk_{m_e} d_p\right) \tag{2.52}$$

where $\widehat{k}_m = k_m - k_{m_e}$ and k_{m_e} is the wavenumber error. Equation 2.52 shows that the model error distorts the poles of the exponential model - which will map to errors in the estimates of their amplitude. From Equation 2.31 and 2.52, it can be seen that the model error $(v_x^r(f)_e)$ is a complex function of the radar operating frequency f, the medium parameters $(\sigma_m, \varepsilon_r)$ and the target location, d_p. Since the approximations to k_m are dependent on the medium conductivity (k_m is exact for $\sigma_m = 0$ mS/m), the model error dependence can be reduced to f, σ_m and d_p. In addition since $\tan\delta$ is a function of the ratio of $\frac{\sigma}{\omega}$, one only needs to consider the model error at a single frequency for changing conductivity. The model error for other frequencies can be interpolated from graphs of conductivity at a single frequency i.e. the model error for $\sigma_m = 10$ mS/m at 1 GHz is the same for $\sigma_m = 20$ mS/m at 2 GHz.

For simplicity, all results in this section will assume the following radar parameters – $f_{start} = 600$ MHz, $\Delta f = 4$ MHz and $N = 140$. These were chosen since they correspond to the radar parameters of the real radar measurements presented later in this chapter.

Figure 2.5 in Section 2.4.1 showed that for conductivity less than 100 mS/m k_{m_e} is less than 1 % of k_m. This will map to a certain model error $v_x^r(f)_e$, of which the sum of the magnitude squared over the radar bandwidth is minimized in Equation 2.33. Figure 2.5 plots the normalized least squared error $J(\mathbf{\Phi})$ (relative to the signal power of the ideal radar model) as a function of conductivity for two targets, with $s_{1,2} = 1$ m, $\tau_{1,2} = 0$ rad, $\gamma_{1,2} = 0$, $d_0 = 1$ m and $d_1 = 1 + \Delta z$ m, where $\{\Delta z \, \epsilon \, \Re : 0.01 < \Delta z < 10\}$ m.

Figure 2.5 shows that for $\sigma_m < 100$ mS/m, the model error is less than 1 %. However, neither Figure 2.3 nor Figure 2.5 provides insight into model parameter estimation errors due to increasing model error.

In this section the effects of model errors on the estimated parameters will be investigated. Since the model is exact for dielectric displacement currents, only the errors due to the conductive currents will be presented. For simplicity, the analysis will be limited to the error of a target space consisting of two targets -

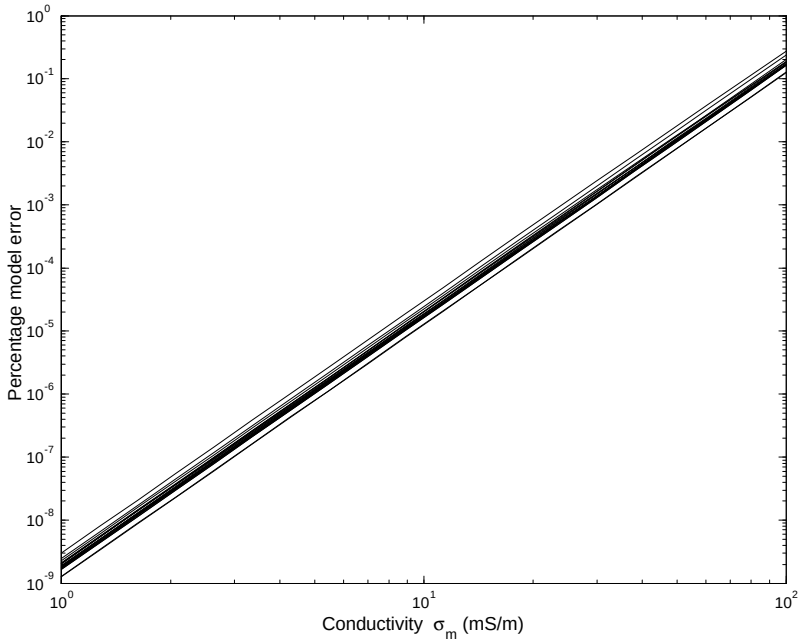

Figure 2.5: Plot of percentage model error as a function of conductivity for two targets with increasing target separation

as is reported in most of the literature in this field [69, 40]. The errors will be presented for changing target positions, different scattering amplitudes, scattering phase and target damping. Due to the complexity of the MPM algorithm, only a numerical analysis is provided.

Errors Due to Target Positions

Two target scenarios will be considered, namely

1. $d_{1,2}$, such that $|d_2 - d_1| < \dfrac{v}{2\,(N-1)\,\Delta f}$, provides a scenario for targets which cannot be resolved by standard IFFT processing techniques.
2. $d_{1,2,}$ such that $|d_2 - d_1| > \dfrac{v}{2\,(N-1)\,\Delta f}$, provides a scenario for targets which can be resolved by standard impulse processing techniques.

Results are provided to show the target parameters for a single position for each of the required cases, followed by results of the model parameter errors as a range of positions for each case. The model parameter error is the cumulative (for all target positions) root mean square error (RMS) for each of the target parameters. This error measure is greater than the error for the parameters at each individual position and hence provides an upper bound for the individual position errors. This representation was chosen to simplify the visualization of the model parameter errors for multiple targets.

Consider a simple target space, consisting of two targets situated at $d = \{1,\ 1.05\}$ m with $s_p = 1$ m, $\tau_p = 0$ rad and $\gamma_p = 0$. Figure 2.6 plots the target parameters for increasing conductivity, while Figure 2.7 plots the corresponding pole positions, z_p. Figure 2.6 shows that the model errors increase for all parameters for $\sigma_m > 30$ mS/m. Figure 2.7 shows that for increasing conductivity the poles move away from their correct value (denoted by a circle).

Increasing the distance between the two targets to 1.4 m, such that $d = \{1,\ 2.4\}$ m results in increased model parameter errors as is shown in Figures 2.8 and 2.9. Figure 2.8 shows that for $\sigma_m > 30$ mS/m the errors for all target parameters

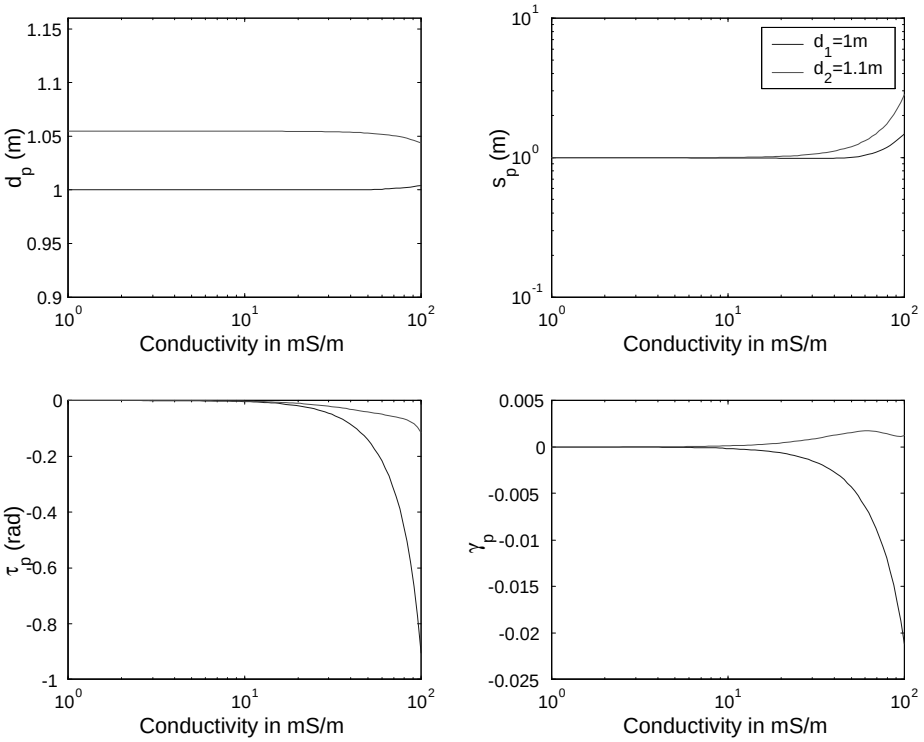

Figure 2.6: Estimated radar model parameters as a function of conductivity for targets located at 1 m and 1.05 m

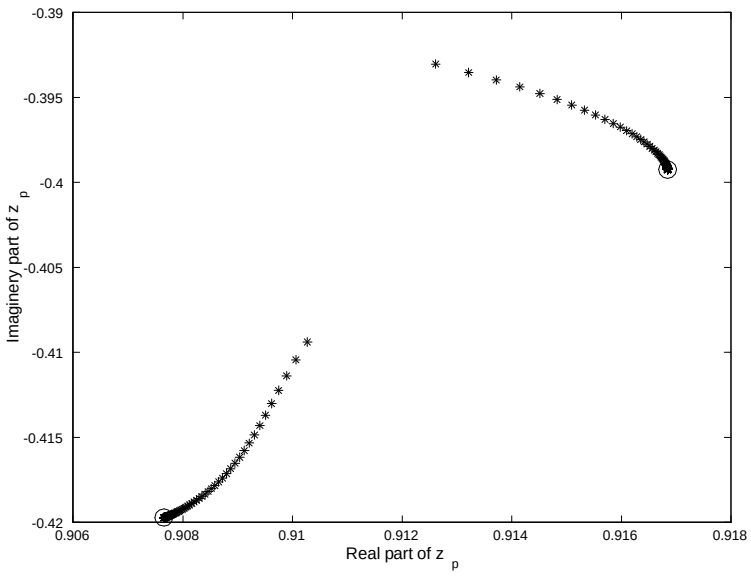

Figure 2.7: Plot of estimated poles (z_p) for increasing conductivity

increase. The target position of the far out target converges on the estimate of the close in target. This convergence of the target positions is shown by the movement of the target poles in Figure 2.8. It seems that at this point the MPM algorithm can no longer estimate the target parameters, due to increased model errors. From Figure 2.5 it can be seen that this corresponds to a model error of less than 0.0001 %.

Consider a simple target space, consisting of two targets situated at $d = \{1,\ 1 + \delta z\}$ m with $s_p = 1$ m, $\tau_p = 0$ rad and $\gamma_p = 0$, for $\delta z = \{0.01,\ 0.02,\ 0.03,\ 0.06,\ 0.1\}$ m. Figure 2.10 plots the cumulative errors for each of the estimated model parameter. Figure 2.11 plots the cumulative errors for $\delta z = \{0.05, 0.2, 0.5, 2, 5\}$ m.

Figures 2.10 and 2.11 show that the target errors decrease for increasing distance between the targets and increasing conductivity, resulting in large parameter errors for $\sigma_m < 2$ mS/m for target spacings less than $\dfrac{v}{4N\Delta f}$. The convergence of the two targets seen in Figure 2.8 for conductivities $\sigma_m > 12$ mS/m can also be observed in Figure 2.11. Figure 2.11 shows that the target error increases rapidly at a certain conductivity (depending on the target position) reaching a

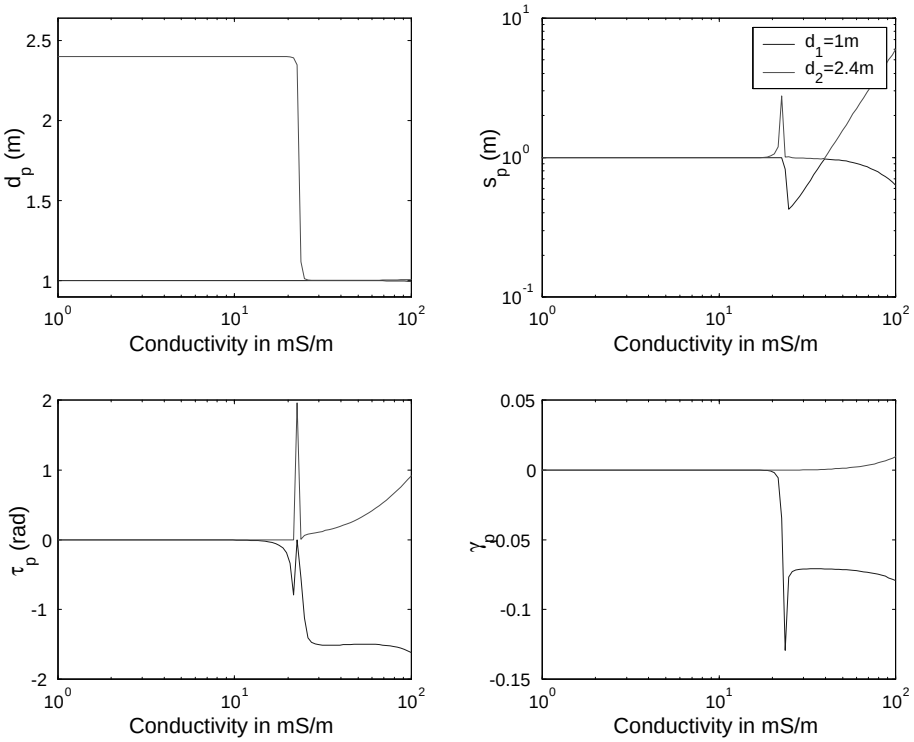

Figure 2.8: Estimated radar model parameters as a function of conductivity for targets located at 1 m and 2.4 m

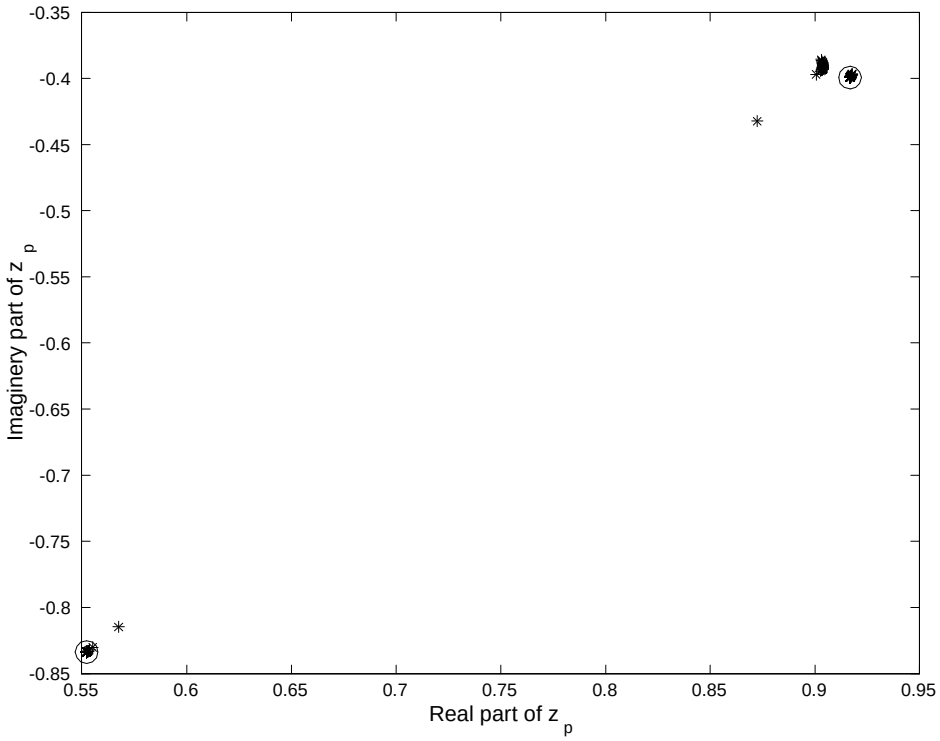

Figure 2.9: Plot of estimated pole positions (z_p) as a function of conductivity

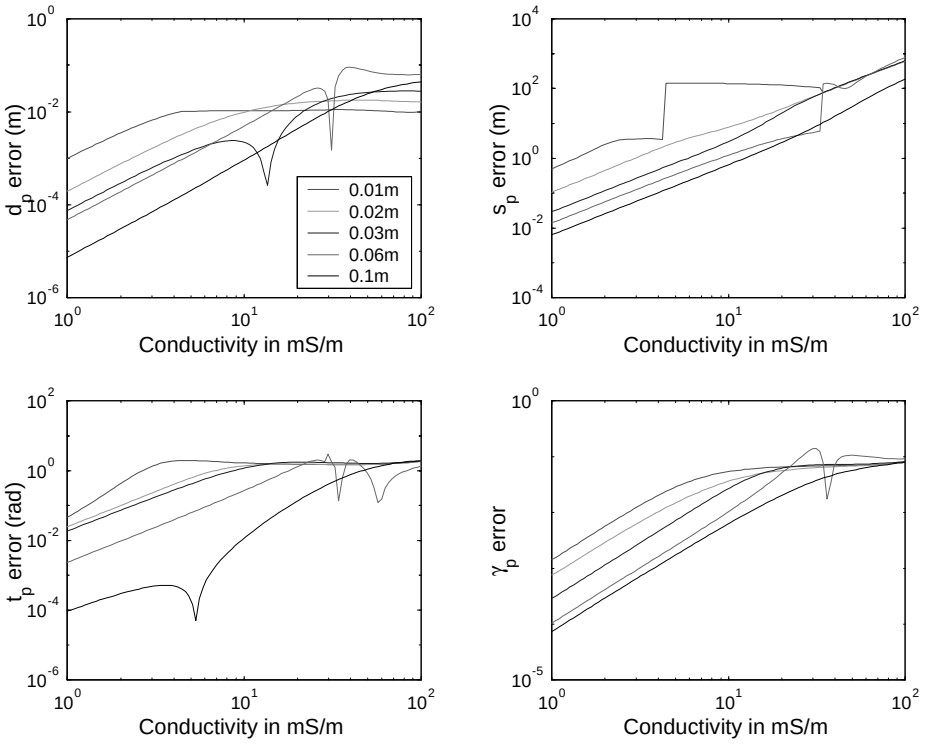

Figure 2.10: Plot of model parameter errors for increasing conductivity and for target spacing of $d_p = 0.01$, 0.02, 0.03, 0.06, 0.1 m

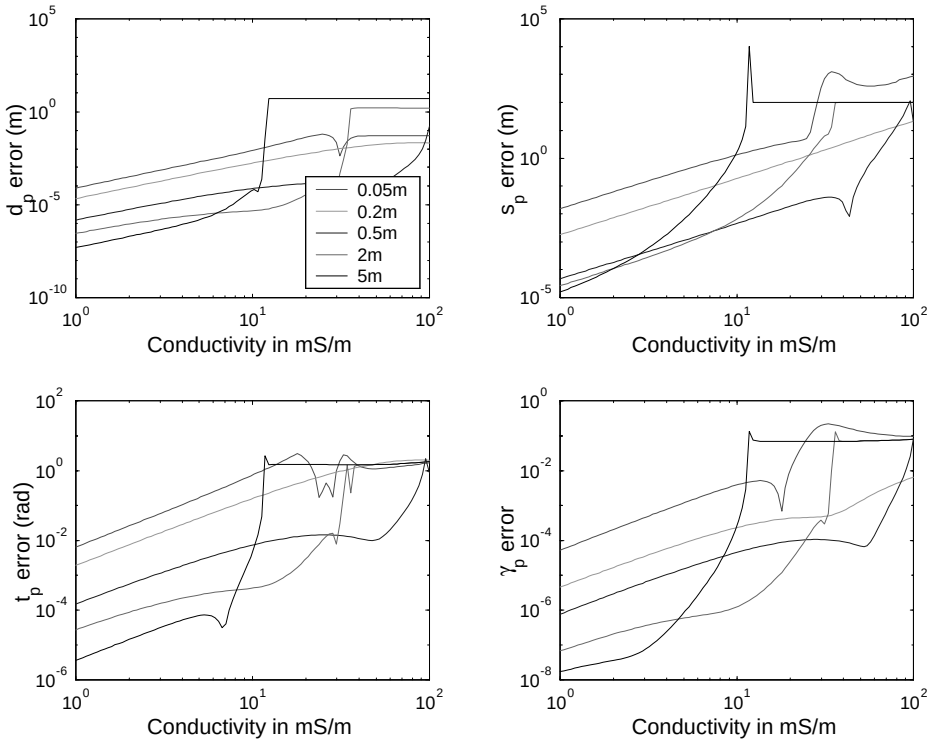

Figure 2.11: Plot of model parameter errors for increasing conductivity and for target spacing of $d_p = 0.05$, 0.2, 0.5, 2, 5 m

maximum error corresponding to the distance between the targets.

Errors due to Target Scattering Amplitude

Consider two targets at $d_p = \{1,\ 2\}$ m, with $s_1 = 1$ m, $s_2 = \{0.05,\ 0.3,\ 1,\ 3,\ 10\}$ m, $\tau_p = \{0,\ 0\}$ rad and $\gamma_p = \{0,\ 0\}$. Figure 2.12 shows the model parameter errors for increasing conductivity. It can be seen that for $\sigma_m < 20$ mS/m, the variation in the model error for the range of scattering amplitudes (s_2) is less than for the range of target positions as presented in Section 2.6.2. It is interesting to note that the error in s_p is almost constant for $\sigma_m < 10$ mS/m.

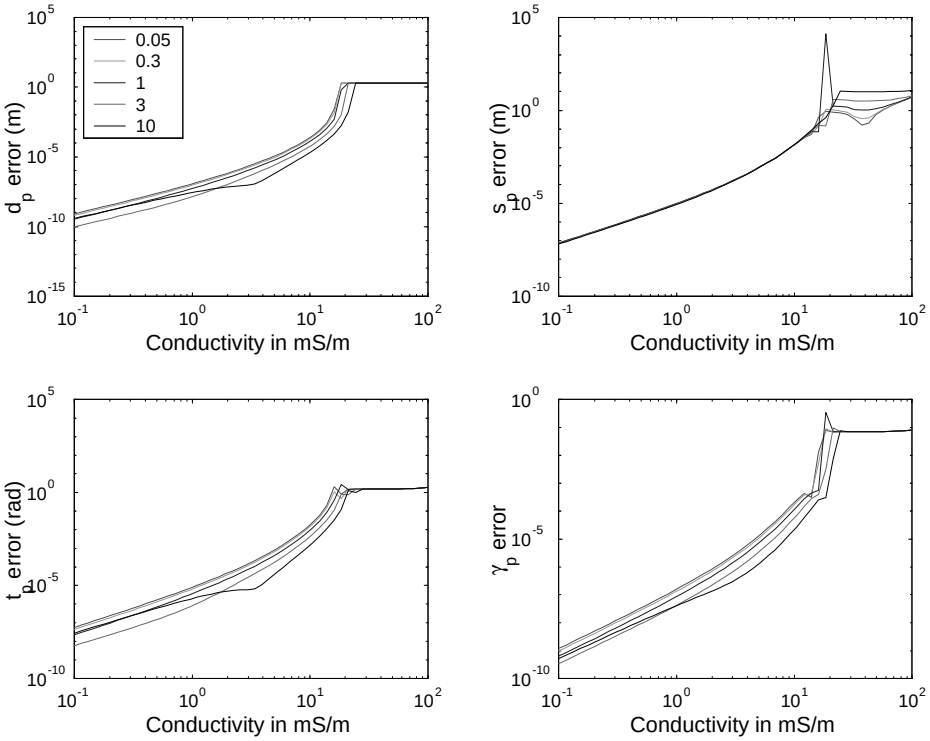

Figure 2.12: Plot of model parameter errors for increasing conductivity with $s_1 = 1$ m and $s_2 = 0.05$, 0.3, 1, 3, 10 m

Errors due to Target Scattering Phase

Consider two targets at $d_p = \{1,\ 2\}$ m, with $s_p = \{1, 1\}$ m, $\tau_1 = 0$ rad, $\tau_2 = \{-2,$ $-0.8,\ 0,\ 0.8,\ 2\}$ rad and $\gamma_p = \{0, 0\}$. Figure 2.13 shows model parameters errors for increasing conductivity. It can be seen that for $\sigma_m < 20$ mS/m the variation in the model error for the range of scattering phase values (τ_2) is less than for the range of target positions as presented in Section 2.6.2.

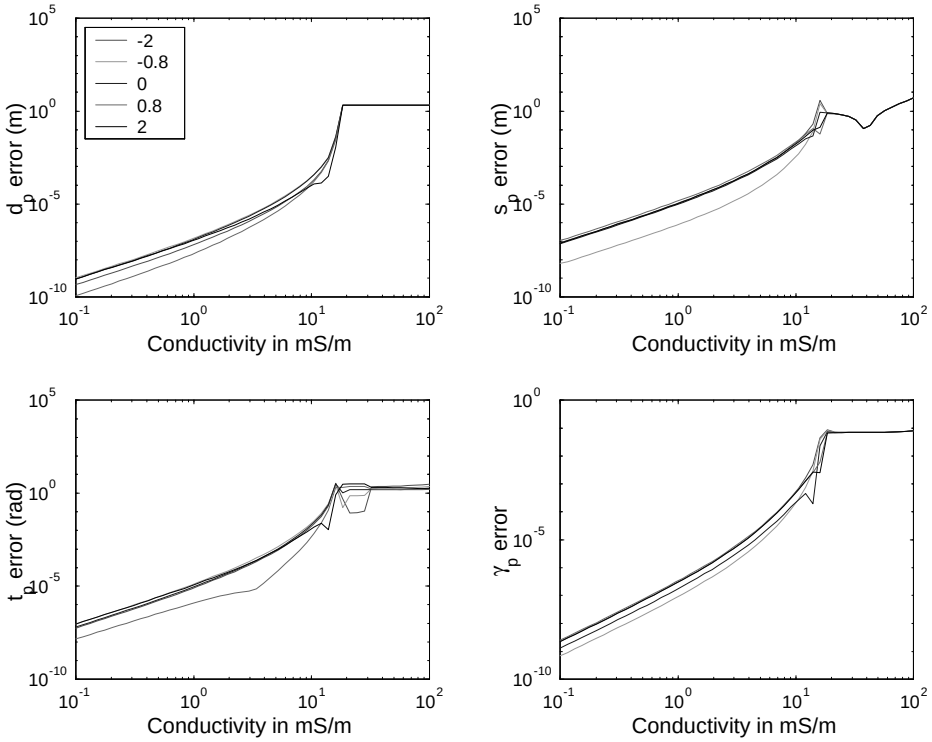

Figure 2.13: Plot of model parameter errors for increasing conductivity and for target scattering phase of $\tau_1 = 0$ rad, $\tau_2 = -2,\ -0.8,\ 0,\ 0.8,\ 2$ rad

Errors due to Target Damping

Consider two targets at $d_p = \{1,\ 2\}$ m, with $s_p = \{1,\ 1\}$ m, $\tau_1 = \{0,\ 0\}$ rad, $\gamma_1 = 0$ rad and $\gamma_2 = \{-0.001,\ -0.003,\ -0.01,\ -0.03,\ -0.1\}$. Figure 2.14 shows the model parameter errors for increasing conductivity. It shows that for an

increasing damping factor the corresponding increase in model error is greater than that for the changing amplitude and phase parameters.

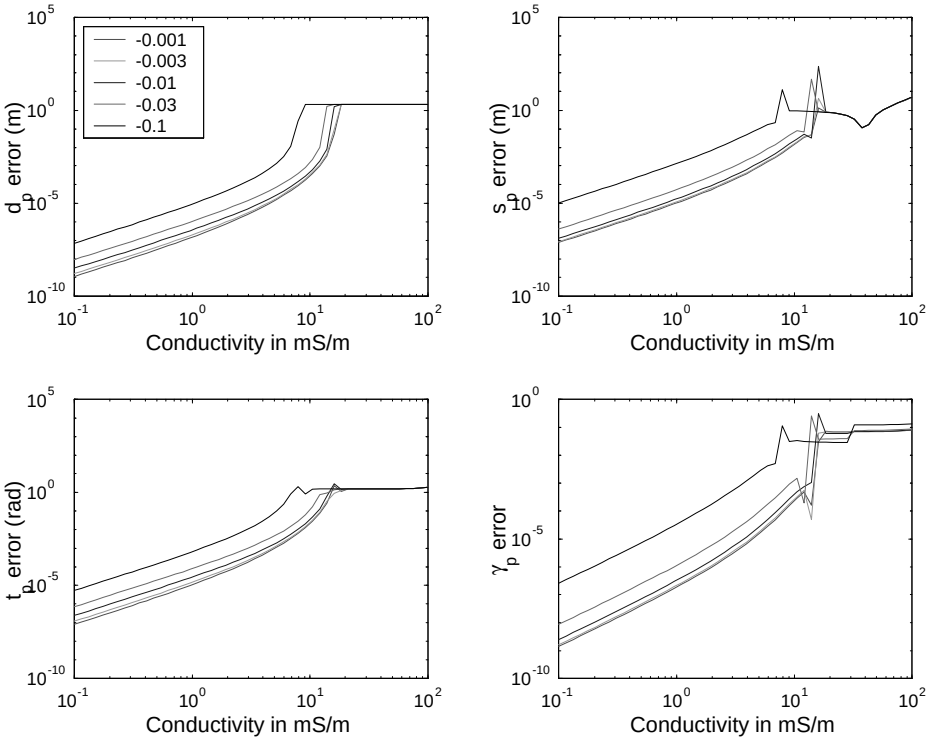

Figure 2.14: Plot of model parameter errors for increasing conductivity and for target dispersion of $\gamma_1 = 0$, $\gamma_2 = -0.001$, -0.003, -0.01, -0.03, -0.1

Discussion

This section has provided a simple analysis of the model errors. From the results, it can be concluded that the model parameter errors are complex, non-linear functions of all the model parameters, with the relative target positions and damping factor resulting in the greatest error. It can also be seen that for low conductivities ($\sigma_m < 5$ mS/m) the model errors were small for all simulations. However, it is difficult to predict an exact cutoff point where the model approximations are no longer valid. This is due to the dependence of the parameters on the error.

2.6.3 IDFT Method

In most SFCW GPR systems, the windowed Inverse Discrete Fourier Transform (IDFT) processing is used to transform the raw radar data into the spatial domain, providing the impulse response of the radar [32, 3, 79]. (Typically the Inverse Fast Fourier Transform is used, which is simply a computationally efficient implementation of the IDFT). Often the amplitudes of the resulting impulse response are related to the reflectivity of targets without consideration for the properties of the medium [32, 3, 79]. In Chapter 1 it was noted that the measured impulse response is the system impulse response, and not the target response. Given that one is able to remove the antenna and radar electronic response from the data, there is still no literature that examines the performance of the IDFT algorithm when used as a parameter estimation technique for SFCW GPR. This section considers an alternative understanding of the IDFT, that will provide insight into the performance of the IDFT for a lossy medium. Appendix D provides an analysis of the IDFT errors for a lossy medium.

The IDFT is equivalent to fitting the data to a number of orthogonal complex exponentials (with certain constraints) in a least squares sense to the received data [33]. The IDFT model can be determined from Equation 2.21 by imposing the IDFT constraints, namely

- $\left|z_p^n\right| = 1$.
- $\arg\left(z_p^n\right) = 2\pi\frac{n}{N}p$, which implies the $\lambda_p = 0$ and $r_p = p\Delta d$, where $\Delta d = \frac{1}{N\Delta r}$.
- $P = N$.

Applying these assumptions to Equation 2.21, can be written as,

$$v_x^{'r}[n] \approx \sum_{p=0}^{P-1} b_p e^{j2\pi\frac{n}{N}p} + n_x^{'}[n] \tag{2.53}$$

In other words, the inverse Discrete Fourier Transform model assumes that there are N pre-assigned and harmonically related spatial frequencies generated by targets at positions $r_p = p\Delta d$. The model thus assumes a solution to the model parameter $\mathbf{z}$, reducing the LS problem to a linear set of equations, which can be described in a matrix form as

$$\mathbf{Zb} = \mathbf{x}_o \tag{2.54}$$

where $\mathbf{Z}$ is an $N \times N$ matrix. Since $\arg\left(z_p^n\right) = 2\pi\frac{n}{N}p$, the column vectors of the matrix $\mathbf{Z}$ are orthonormal. Hence the solution to the LS Equation 2.42 is reduced to a matrix multiplication computation. Thus the impulse response of the radar can be calculated as follows,

$$\mathbf{b} = \frac{1}{N}\mathbf{Z}^H\mathbf{x}_o \tag{2.55}$$

which is simply the matrix form of the IDFT algorithm. The inverse Fast Fourier Transform (IFFT) presents a computationally efficient technique to solve for $\mathbf{b}$.

The impulse response calculated from Equation 2.55 will have high sidelobe levels due to the sharp edges of the limits of the frequency spectrum. These high sidelobes will mask smaller targets close to the main lobe of the impulse response from a stronger target. The sidelobes can be reduced by applying a windowing function to the measured data [80] at the expense of a broadening of the main target lobe. Modifying Equation 2.55 with a windowing function, the amplitudes $\mathbf{b}$ can be expressed as,

$$\mathbf{b} = \frac{1}{N}\mathbf{Z}^H\mathbf{W}\mathbf{x}_o \tag{2.56}$$

where $\mathbf{W}$ is a diagonal matrix such that $w_{i,i} = a_i$ (for $i = 0, 1, \cdots, N-1$) and α_i are the amplitude scaling factors given by the chosen windowing function. Incidentally, Equation 2.56 also describes the discrete impulse response of the system.

As mentioned above, the IDFT implies that the target dispersion $\lambda_p = 0$, and that the target positions are limited to discrete positions, Δd. The limiting of the target positions results in the classical bandwidth, resolution and sidelobe problem, discussed in most radar text books and addressed in a previous paper by the author [81].

2.7 Simulation Results

Simulations were performed to compare the impulse response of the system with the model based parameter estimation algorithm discussed above. The raw data was generated using the SFCW GPR model developed in this chapter. The radar parameters used are listed in Table 2.1.

Parameter	Value
f_L	600 MHz
N	140
Δf	4 MHz
$P_{\max}$	-30 dBm
N_s	-145 dBm

Table 2.1: Radar parameters for the single polarization simulations

$P_{\max}$ is the maximum received signal power and N_{s} is the radar noise floor. For all simulations the gain of the radar was adjusted such that the maximum signal level of -30 dBm was received for a zero loss medium. The noise is generated based on the noise floor of a typical SFCW GPR. The SNR for the radar is simply the maximum received power less the radar noise floor. It is important to note that for multiple targets the performance of the algorithm is dependent on both the SNR of the radar receiver and the relative amplitudes of the scatterers [40].

The raw radar data was generated by placing three targets in various lossy media at different depths below the radar, as shown in Figure 2.1. The target parameters used are listed in Table 2.2.

Parameter	Value
d_p (m)	$1.6, 2.1, 2.2$
s_p (m)	$1, 0.5, 2$
τ_p (rad)	$-\frac{\pi}{8}, \frac{\pi}{4}, 0$
λ_p	$-0.1, -0.04, 0$

Table 2.2: List of targets and their parameters for the single polarization simulations

The model generated data was processed using a Hamming window [80] and IFFT algorithm to determine the radar impulse response, and the MPM algorithm to extract the target parameters. The estimated medium parameters $\alpha_{m1,}$ α_{m2}, β_{m1} and β_{m1} required to determine the radar model parameters, were estimated by fitting a straight line to the calculated wavenumber k_m, in a least squared sense. In the next two sections, simulations will be presented to show the effects of both conductive and dielectric losses on the impulse response and the MPM algorithm.

2.7.1 Conductive Losses

Figures 2.15 - 2.19 show the results of the simulation for media with conductivities of $1, 5, 10, 20, 30, 40$ mS/m respectively and a relative dielectric constant of $\varepsilon_r^{'} = 6$. For each simulation two plots are presented. The first shows the received power and phase of the unprocessed data as a function of frequency. The second plot presents the radar impulse response and estimated target amplitude both as functions of distance from the radar origin. Graphs are also presented to show the estimate model parameters and their errors as a function of conductivity.

Figure 2.20 plots the estimated target parameters as a function of increasing conductivity, while Figure 2.21 plots the root mean square (RMS) error for each model parameter.

Figure 2.22 plots the singular value energy ratio, $\eta(p)$ for the various simulations.

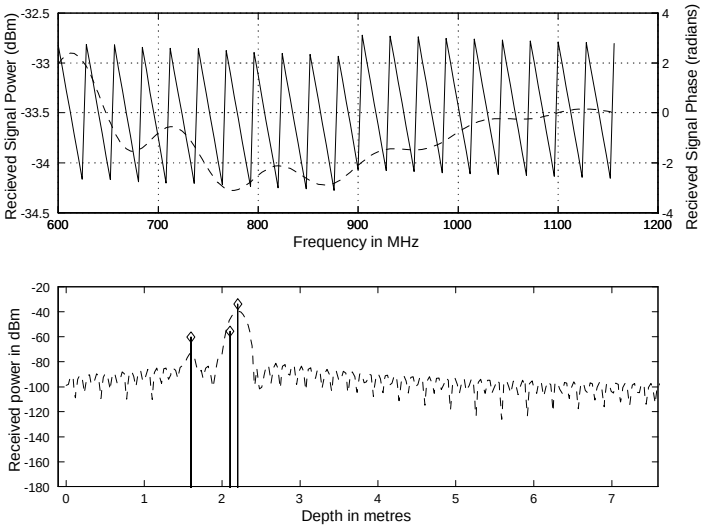

Figure 2.15: Plot of raw and processed data for a conductivity of 1 mS/m ($\tan\delta \approx 0$, $m_e \approx 0$ and SNR ≈ 111 dB)

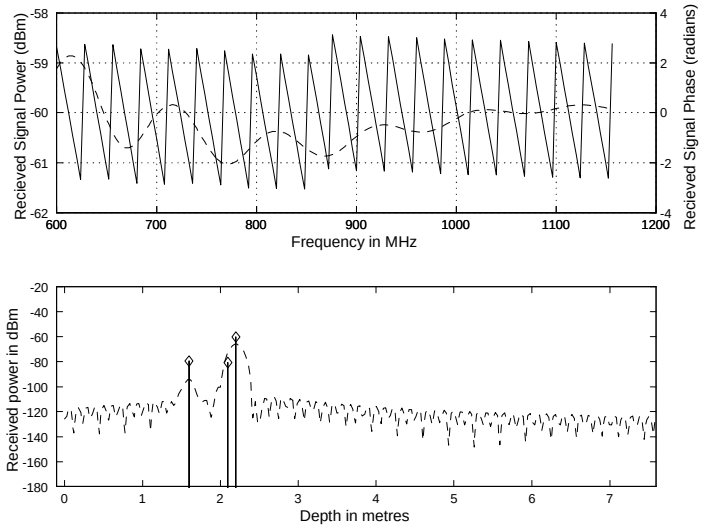

Figure 2.16: Plot of raw and processed data for a conductivity of 10 mS/m ($\tan\delta \approx 0.05$, $m_e \approx 0.01$, and SNR ≈ 85 dB)

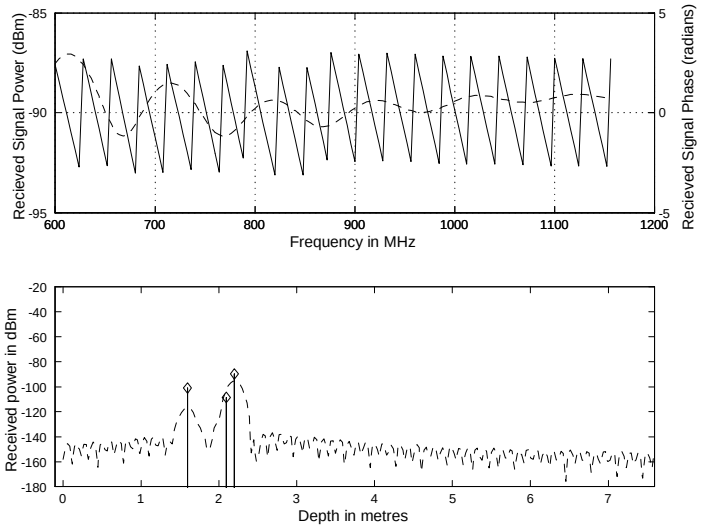

Figure 2.17: Plot of raw and processed data for a conductivity of 20 mS/m ($\tan\delta \approx 0.1$, $m_e \approx 0.04$, and SNR ≈ 56 dB)

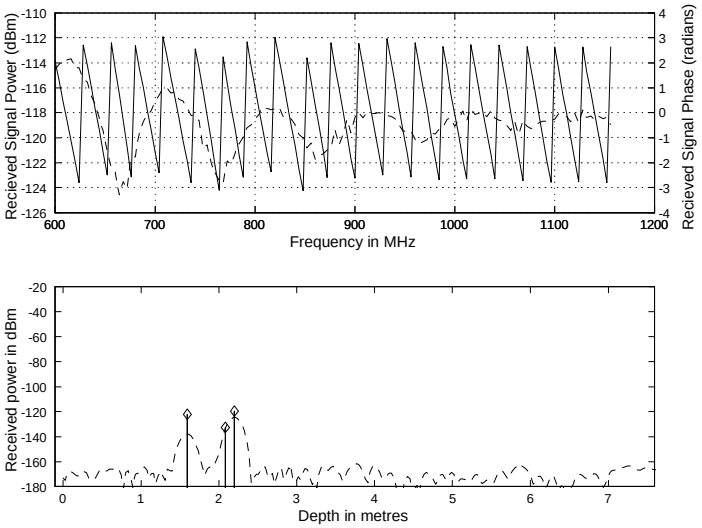

Figure 2.18: Plot of raw and processed data for a conductivity of 30 mS/m ($\tan\delta \approx 0.15$, $m_e \approx 0.09$, and SNR ≈ 27 dB).

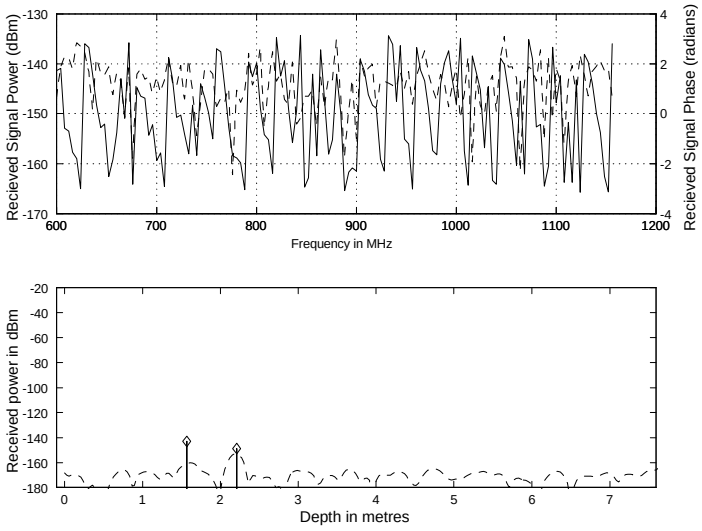

Figure 2.19: Plot of raw and processed data for a conductivity of 40 smS/m ($\tan\delta \approx 0.2$, $m_e \approx 0.15$ and SNR ≈ 2.3 dB).

Discussion

Increasing conductivity leads to an increase in medium losses which result in decreasing signal-noise-ratio for each scatterer. In addition the increasing conductivity results in increased model error. However, Figures 2.15 - 2.18 show that the MPM algorithm is still able to estimate the parameters for all simulated scatterers, resolving targets that cannot be resolved with the IFFT based processing. For a conductivity of $\sigma_m = 40$ mS/m, the signal is attenuated at more than 50 dB/m, resulting in a received SNR of 2.5 dB – however the algorithm is still able to resolve the targets at $d_p = 1.6$ m and 2.2 m. Note that the MPM algorithm can estimate the target positions and amplitudes even when it is barely visible in the radar impulse response.

Figures 2.20 and 2.21 provide a more detailed look at the performance of the MPM method for the above simulation - showing the model estimates and errors as a function of conductivity. The error estimates are small (less than 1 % of their true values) for conductivities less the 30 mS/m. This corresponds to a $\tan\delta \approx 0.1$ and a model error $m_e \approx 0.04$, which is much smaller than 1 as

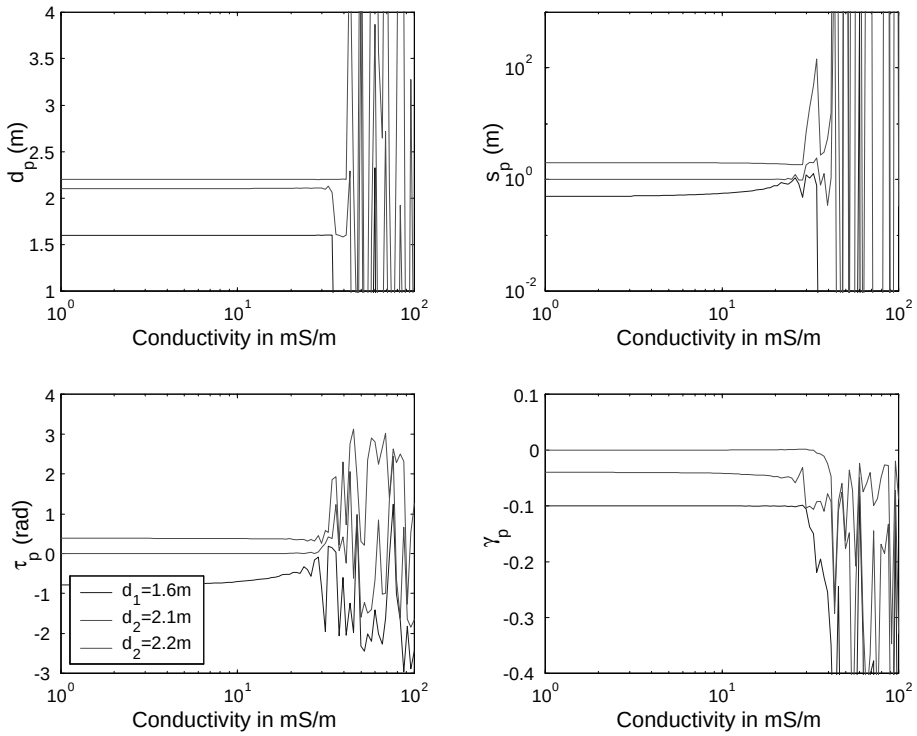

Figure 2.20: Plot of extracted target parameters as a function of conductivity

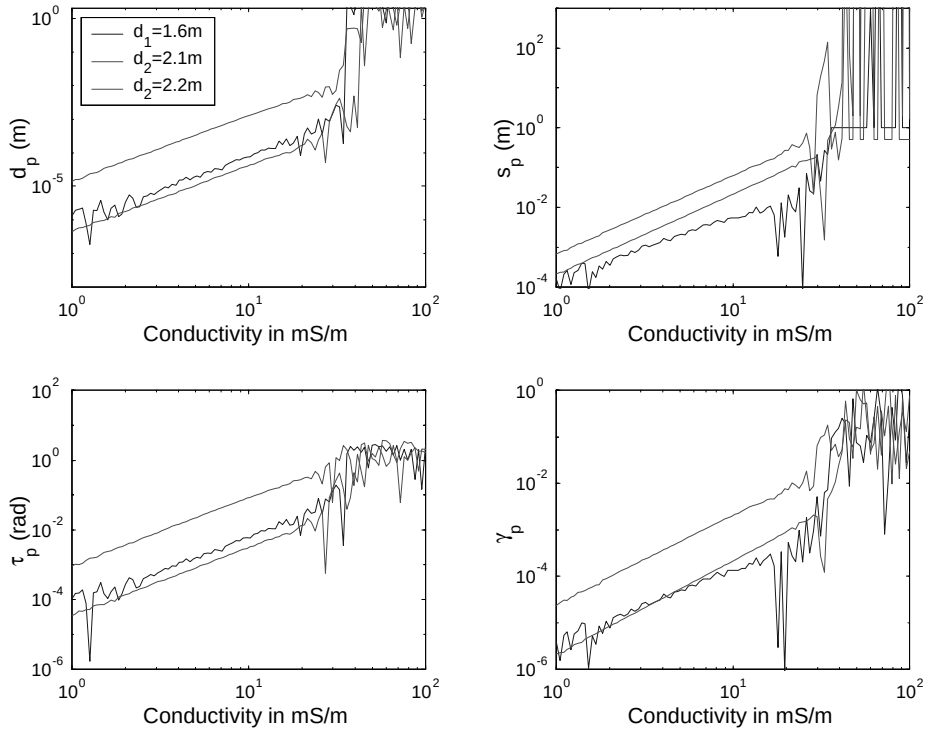

Figure 2.21: Plot of the RMS error for the model target parameters as a function of conductivity

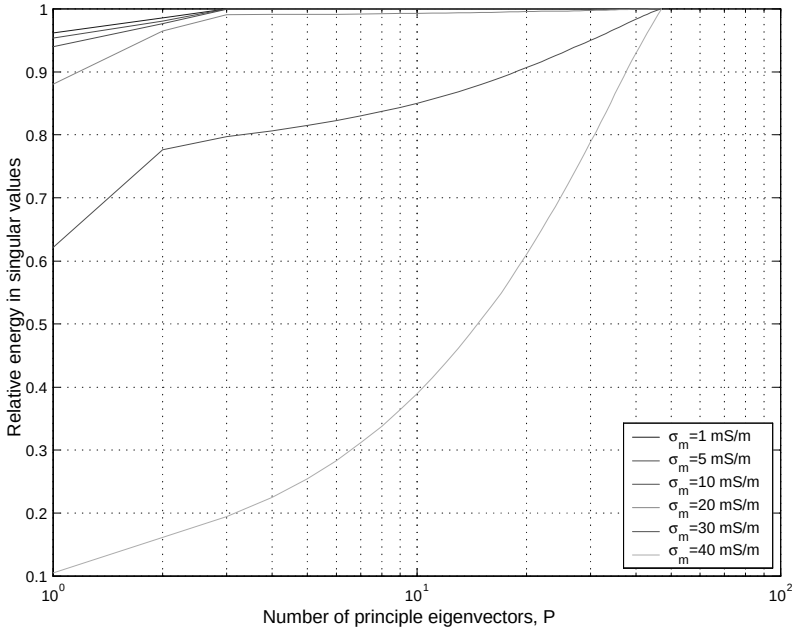

Figure 2.22: Plot of $\eta(p)$ for $p \leq l$ for $\sigma_m = 1$, 5, 10, 20, 30 and 40 mS/m

required by the approximations to linearize k_m presented in Appendix A.

Finally, Figure 2.22 shows the relative energy in the singular values, $\eta(p)$ for $p < N/3$. It can be seen that for low SNR, corresponding to low conductivity, most of the signal energy is in the first three eigenvectors, corresponding to the three targets. However as the SNR ratio increases, the energy is spread over all the eigenvalues, making it difficult to determine the number of targets from the measured data.

2.7.2 Dielectric Losses

Figures 2.23 - 2.27 show the results of the simulation for a medium with a relative real permittivity of 6, relative imaginary permittivity of -0.01, -0.1, -0.2, -0.4, -0.8, -1 and a conductivity of 0 mS/m.For each simulation two plots are presented. The first shows the received power and phase of the unprocessed data as a function of frequency. The second plot presents the radar impulse re-

sponse and estimated target amplitude as a function of position from the radar origin. Graphs are also presented to show the estimate model parameters and their errors as a function of the imaginary permittivity.

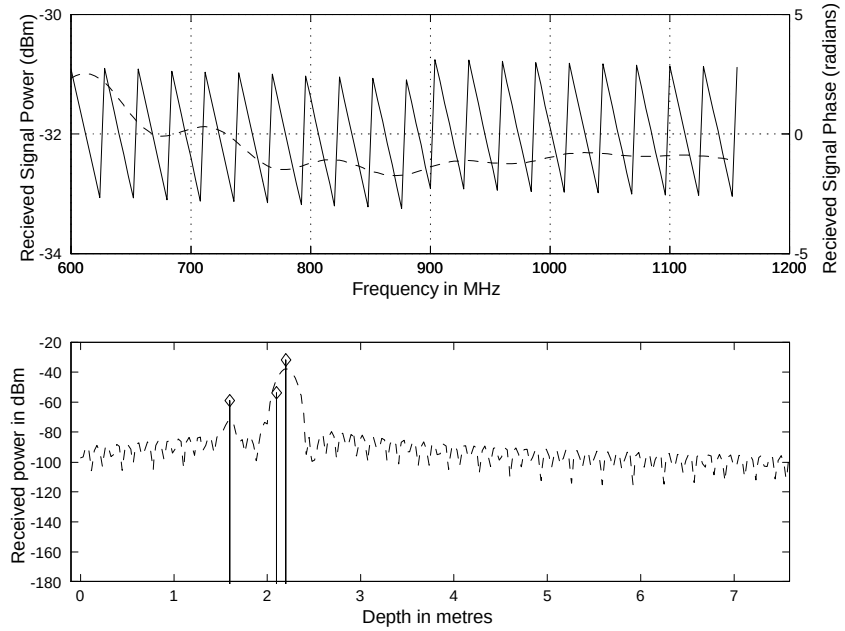

Figure 2.23: Plot of raw and processed data for $\epsilon_r = 6 - 0.01j$ ($\tan\delta \approx 0$, $m_e \approx 0$ and SNR ≈ 113 dB)

Figure 2.28 plots the estimated target parameters as a function of the increasing imaginary part of the permittivity.

Figure 2.29 plots the singular value energy ratio, $\eta(p)$ for the various lossy media.

2.7.3 Discussion

As shown in Appendix A, for conductivity $\sigma_m = 0$, the model error is zero, and hence the model is exact. The results presented in this section purely examine the performance of the MPM algorithm for decreasing SNR – since, increasing the imaginary component of the permittivity leads to an increase in the dielectric displacement current and hence an increase in medium losses and decrease in

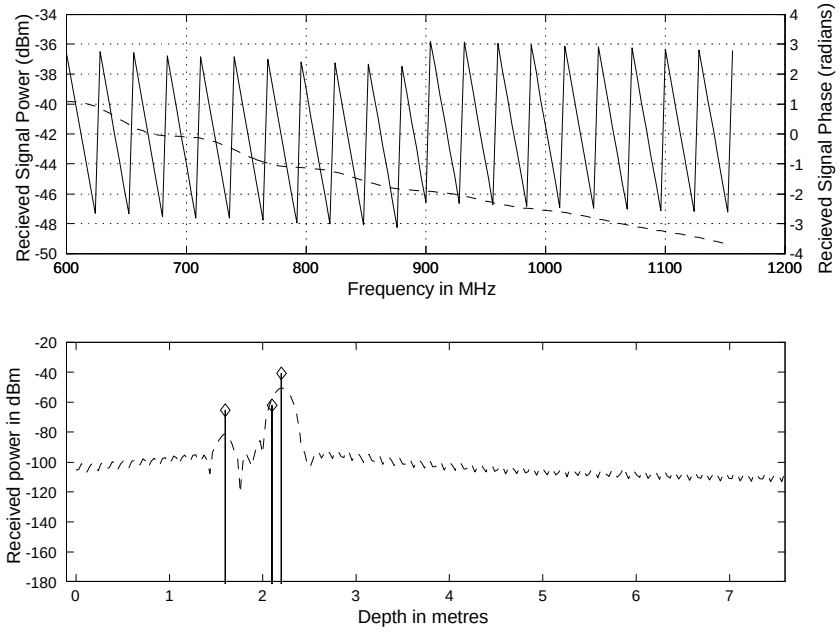

Figure 2.24: Plot of raw and processed data for $\epsilon_r = 6 - 0.1j$ ($\tan\delta \approx 0.02$, $m_e \approx 0$ and SNR ≈ 100 dB)

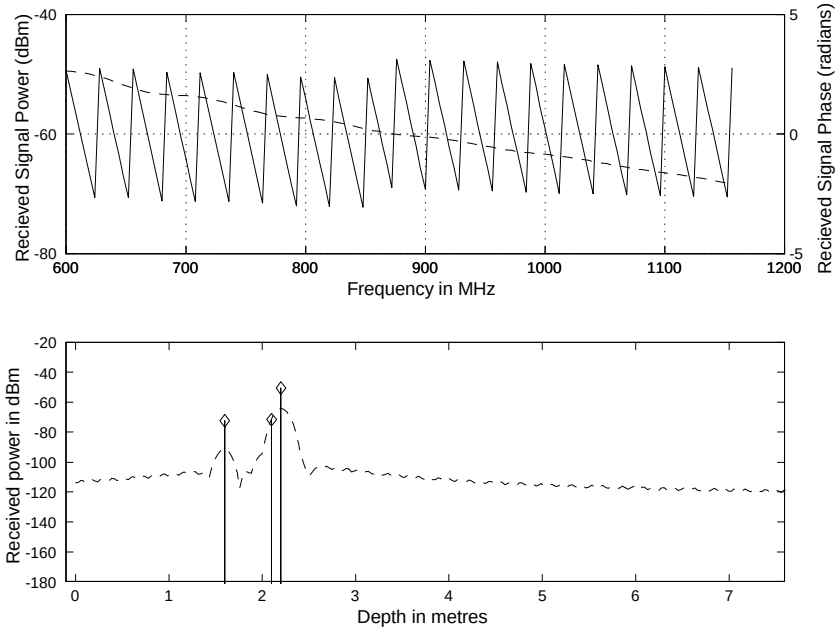

Figure 2.25: Plot of raw and processed data for $\epsilon_r = 6 - 0.2j$ ($\tan\delta \approx 0.03$, $m_e \approx 0$ and SNR ≈ 88 dB)

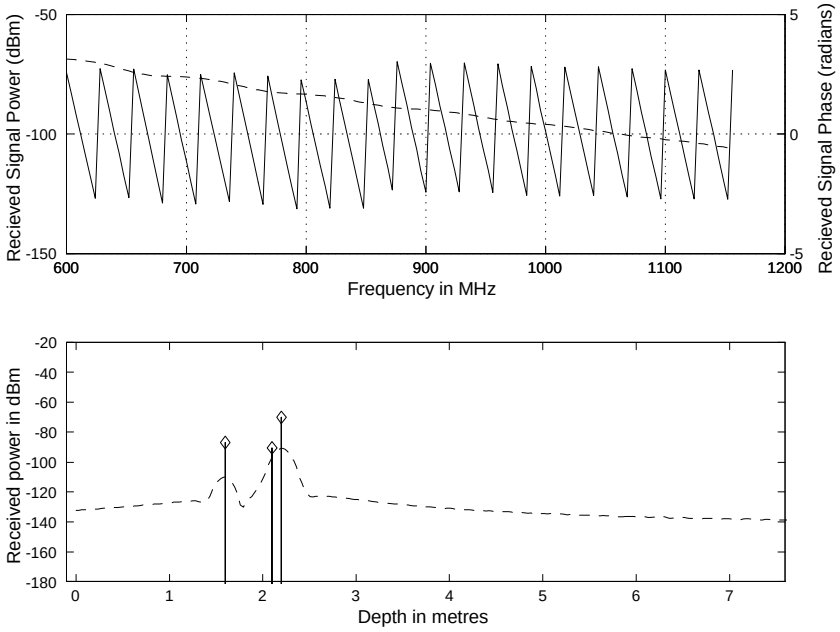

Figure 2.26: Plot of raw and processed data for $\epsilon_r = 6 - 0.4j$ ($\tan\delta \approx 0.07$, $m_e \approx 0$ and SNR ≈ 66 dB)

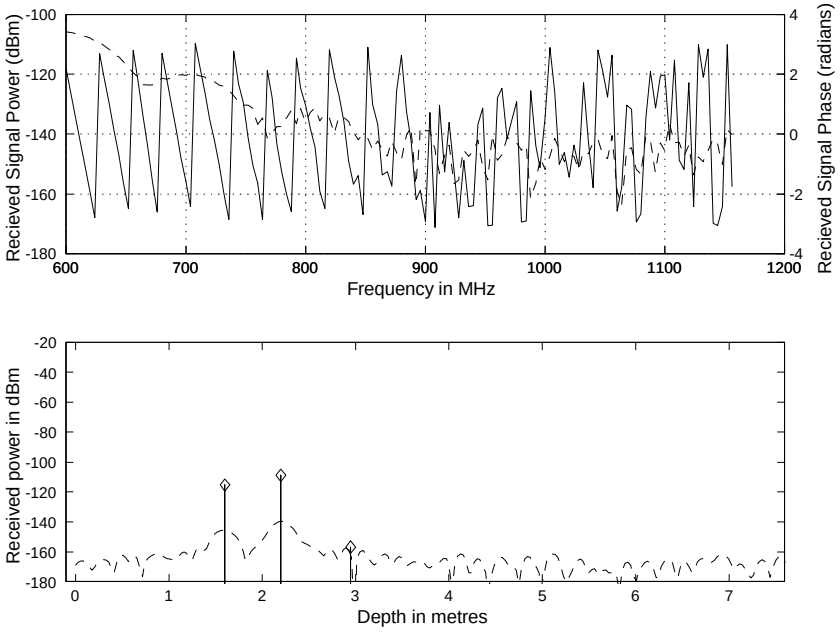

Figure 2.27: Plot of raw and processed data for $\epsilon_r = 6 - 0.8j$ ($\tan\delta \approx 0.13$, $m_e \approx 0$ and SNR ≈ 25 dB)

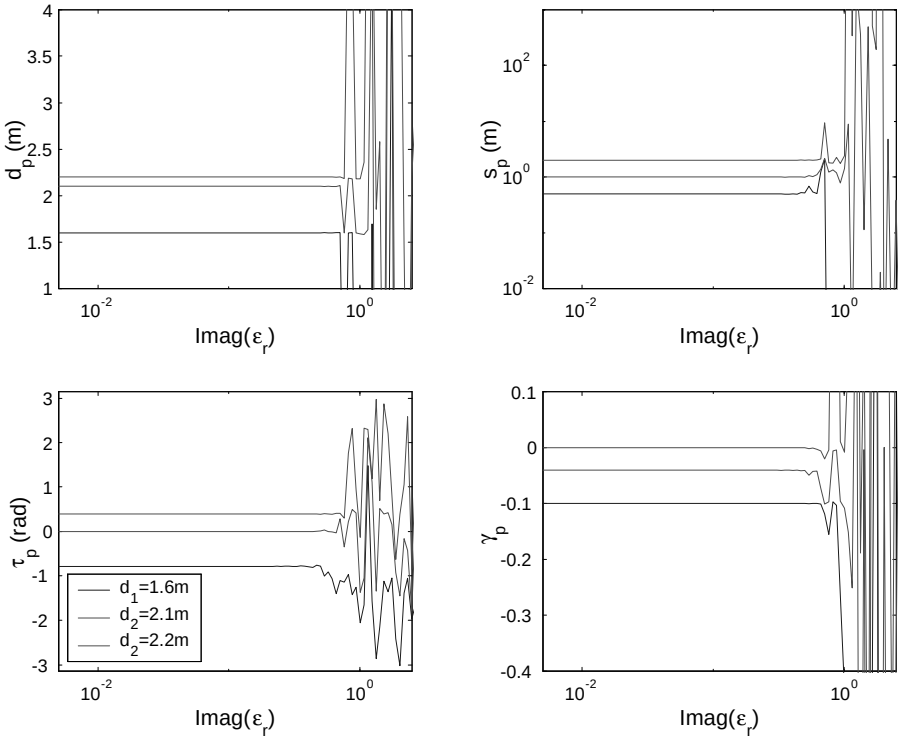

Figure 2.28: Plot of extracted target parameters as a function of the imaginery permittivity

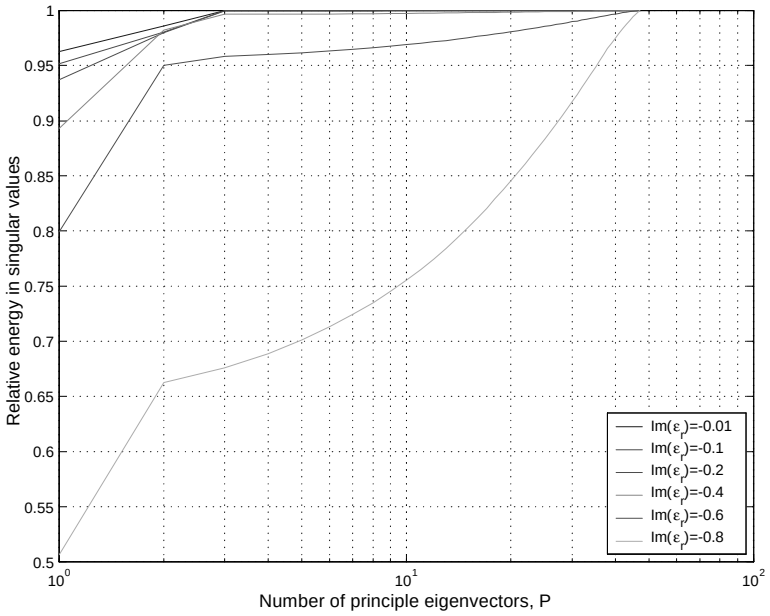

Figure 2.29: Plot of $\eta(p)$ for $p \leq l$ for $\varepsilon_r^{''} = -0.01$, 0.1, 0.2, 0.4, 0.8 and 1.0

signal-noise-ratio for each scatterer. The raw data in Figures 2.23 - 2.27 show that for increasing dielectric displacement current there is a corresponding increase in the attenuation of the high frequencies as compared to the lower frequencies – effectively low pass filtering the data. This increase in signal attenuation for increase frequency is greater than the simulations for increasing conductivity - as can be seen from Figures 2.15 - 2.18 – hence the dielectric induced conductivity results in a greater low pass filtering effect than that of ionic conductivity.

Figure 2.28 shows the predicted model parameters for increasing imaginary permittivity. The MPM algorithm is able to extract all the target parameters for SNR greater than 30 dB. This is higher than that measured for conductivity. This is due to the increased attenuation for higher frequencies, which results in the power in the upper end of the frequency spectrum falling below the radar noise floor. This effectively reduces the received radar bandwidth and hence information available to determine the model parameters. It can be seen from Figure 2.26 that the resulting signal bandwidth is less than half of the transmitted bandwidth.

Figure 2.29 shows the relative energy in the singular values, $\eta(p)$ for $p < N/3$. It can be seen that for low SNR, corresponding to low imaginary permittivity, most of the signal energy is in the first three eigenvectors, corresponding to the three targets. However as the SNR ratio increases, the energy is spread over all the eigenvalues, making it difficult to determine the number of targets from the measured data.

2.8 Measurements

In this section the results of real radar measurements are presented. Due to the limited equipment resources, it was not possible to measure all the required calibration functions (Equation 3.6), except for the radar electronics frequency response ($G_s(f)$). It was also not possible to measure the properties of the medium accurately. However, the processing still allows for the extraction of target positions and uncalibrated amplitude information. In this section two sets of results will be presented – a pipe moving on the ground surface over buried antennas and pipe buried in the ground with antennas moving over the surface. All radar data was captured using the MercuryB radar system developed by the author. The details of this system are presented in Chapter 4.

2.8.1 Buried Antenna Pipe Measurements

Figure 2.30 shows the basic measurement setup.

Each measurement profile consists of 250 frequency steps starting from 200 MHz with a step size of 4 MHz. The radar transmit and receive antennas were buried at a depth of 0.3 m below the surface. A 2 m long metallic pipe was rolled along the surface for a distance of 1.2 m. Radar data was captured at intervals of 0.05 m. Figure 2.31 shows the amplitude of the two dimensional impulse response. Both the pipe response and the transmit/receive coupling measurements are clearly visible.

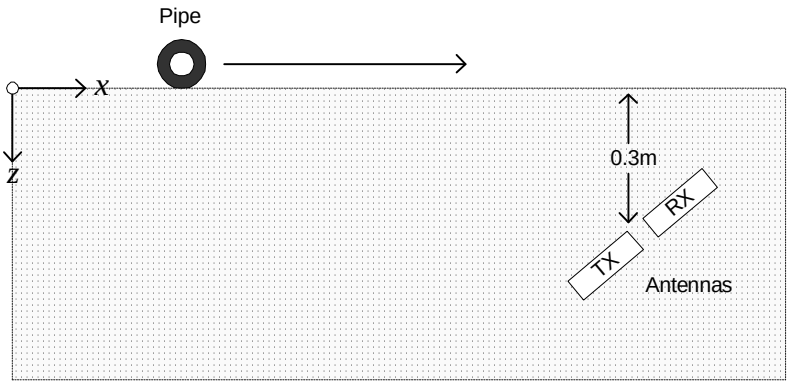

Figure 2.30: Measurement setup for buried antenna pipe measurement

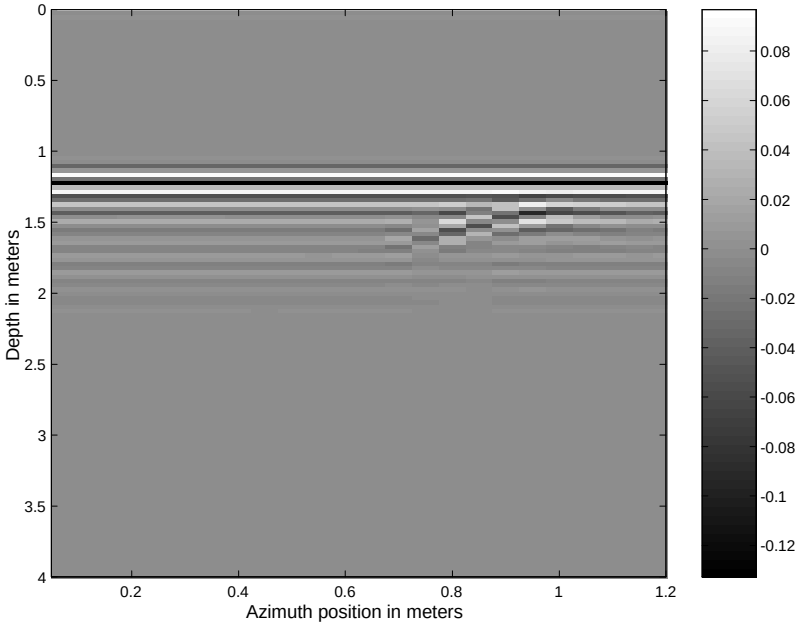

Figure 2.31: Two dimensional magnitude plot of the radar impulse response

Since the antennas are stationary, the background radar response is constant for all profiles. It is hence possible to remove the transmitter to receiver coupling by subtracting the mean profile response from all measured profiles as well as the constant background reflection from the air-ground interface. In addition, the mean profile response can be used to estimate the reference (zero) point for the data set. Figure 2.32 shows the mean profile response for the measured data.

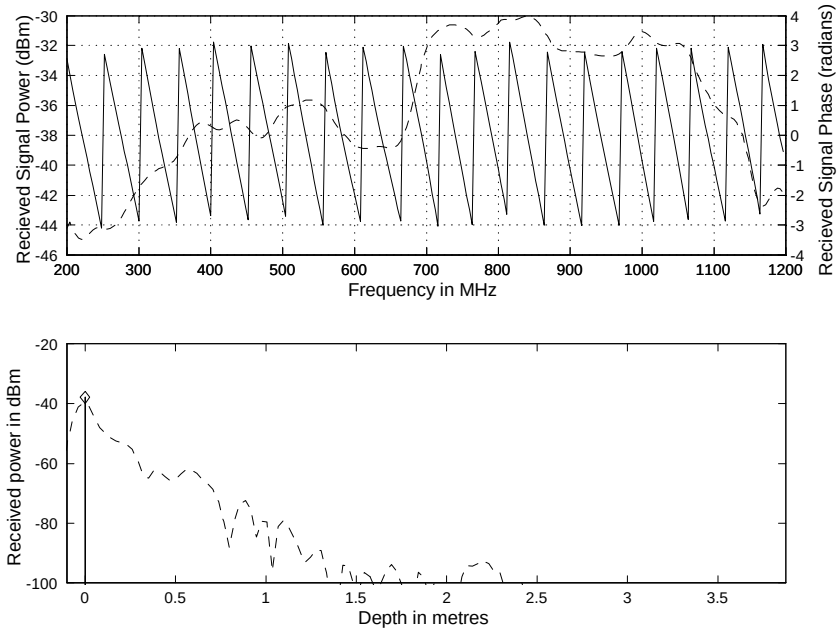

Figure 2.32: Plot of the raw and processed mean profile response of the measured data

Using the MPM algorithm and assuming a real permittivity of $\varepsilon_r = 6$, the zero point offset is 1.2 m. The calculation also assumes that the subsurface medium can be represented by an average permittivity. Also note that zero point offset is not a measure of the true electrical length of the coupling signal, but the effective electrical length for propagation through a medium with a permittivity as given above.

Figures 2.33 - 2.35 show the raw and processed data for range profiles located at 0.25 m, 0.95 m and 1.00 m from the start position of the pipe. Two principal

target vectors were assumed when processing the data with the MPM algorithm - corresponding to two expected reflections - one from the ground/pipe interface and one from the EM wave that propagates around the pipe before returning to the radar.

In Figure 2.33 the pipe is not yet in the beamwidth of the antennas. The first reflection in this figure is the earth/air interface. The second reflection is much smaller than the first, and most likely represents some scattering from some electrical discontinuity within the ground.

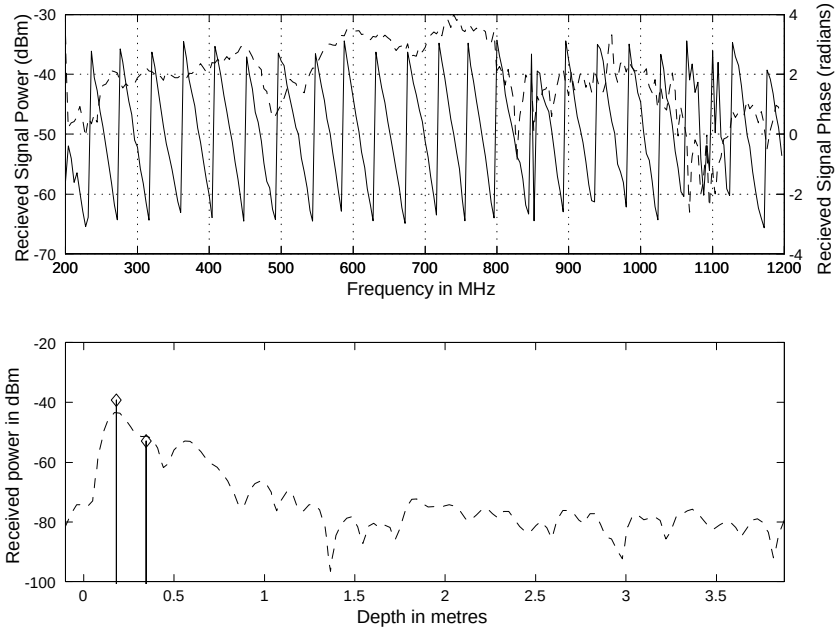

Figure 2.33: Plot of raw and processed data for the 5^{th} range profile (0.25 m)

In Figures 2.34 and 2.35 the pipe is within the beamwidth of the antenna. In both figures two reflections of similar amplitude are visible. In addition, these reflections have a constant spacing of 7 cm between the scatterers.

To further demonstrate the MPM processing, all 24 range profiles were processed. Only some of the extracted target vectors correspond to actual pipe reflections. A simple threshold algorithm was used to separate the pipe reflections from other target reflections. Consider the amplitude spectrum of the extracted target

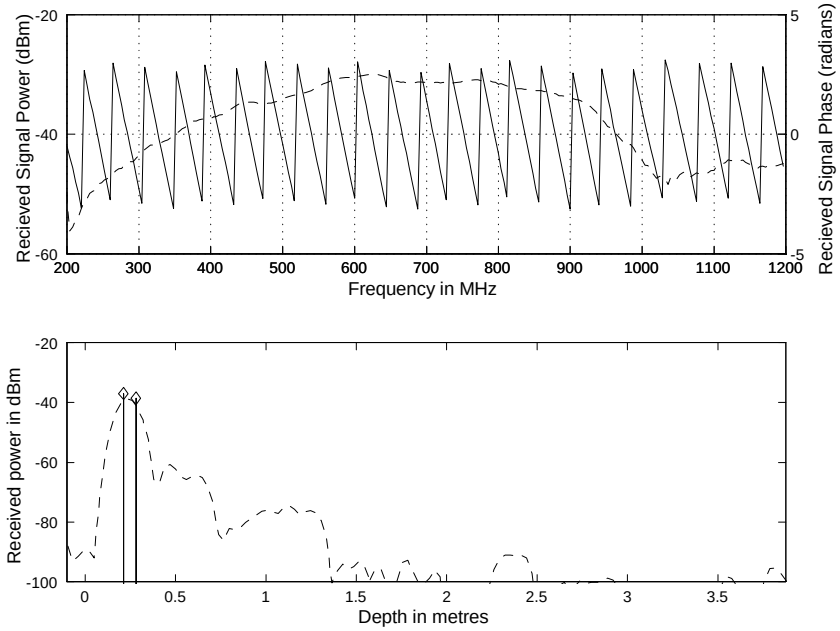

Figure 2.34: Plot of raw and processed data for the 19^{th} range profile (0.95 m)

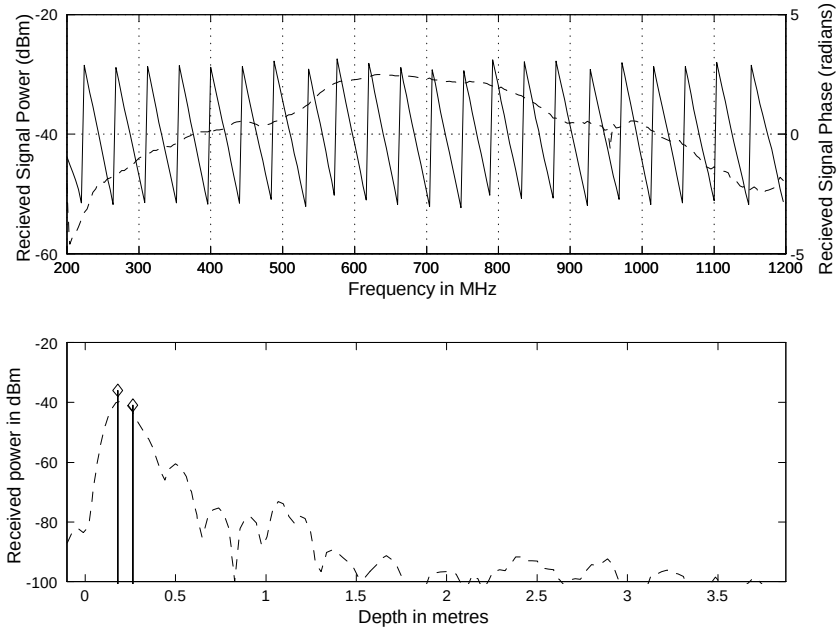

Figure 2.35: Plot of raw and processed data for the 21^{st} range profile (1.0 m)

vectors ($PV1$ and $PV2$) as a function of azimuth position as shown in Figure 2.36.

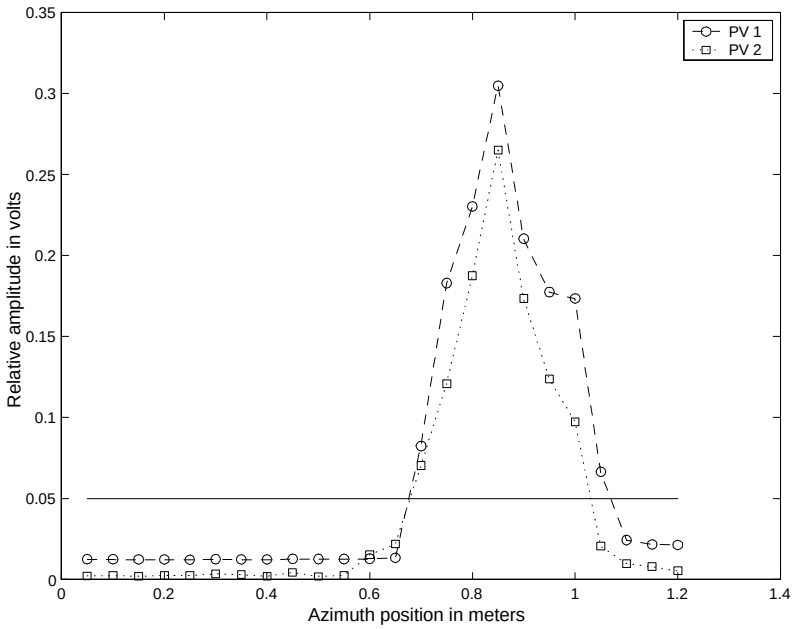

Figure 2.36: Amplitude response for each principle component vector from the MPM alogirthm as a function of pipe azimuth position

Targets with amplitudes less than 50 mV were ignored. Figure 2.37 shows the results for processing the raw data using the standard windowed FFT processing (a) and the MPM processing with amplitude target selection (b). Both Figure 2.37(a) and (b) clearly show the change in position as the pipe roles towards the antennas. In addition Figure 2.37(b) shows that the target response shown in Figure 2.37(a) is made up of two reflections – possibly the direct ground/pipe and delayed creepy wave reflection (i.e. the energy propagates around the pipe).

Figure 2.38 shows the spacing between two reflectors at the same azimuth location. This figure shows that while the pipe is within the antenna beamwidth, the spacing between the target vectors is constant and approximately equal to 14 cm (assuming the second reflection occurs in free space).

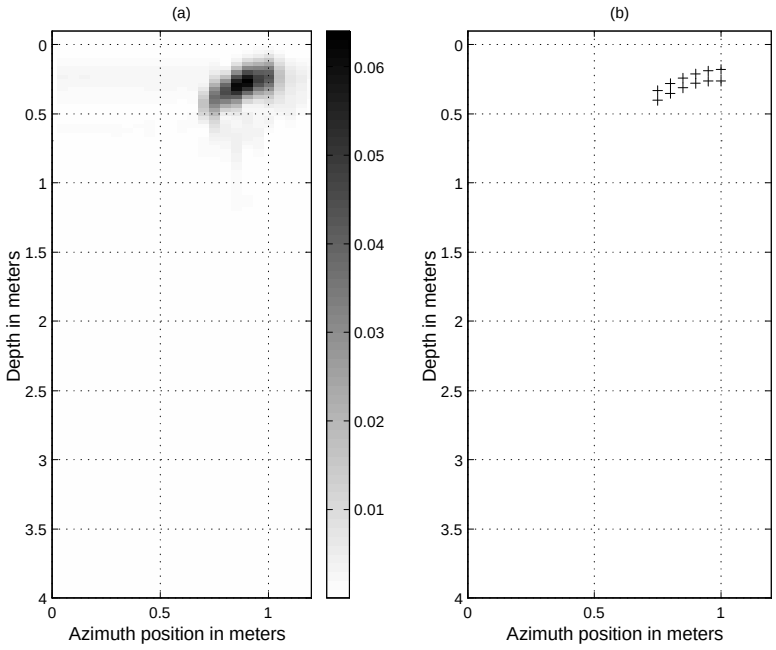

Figure 2.37: Images of the processed radar data after background subtraction. Figure (a) plots the amplitude response of the radar impulse response. Figure (b) plots the position of the target vectors estimated from the MPM algorithm as a function of position

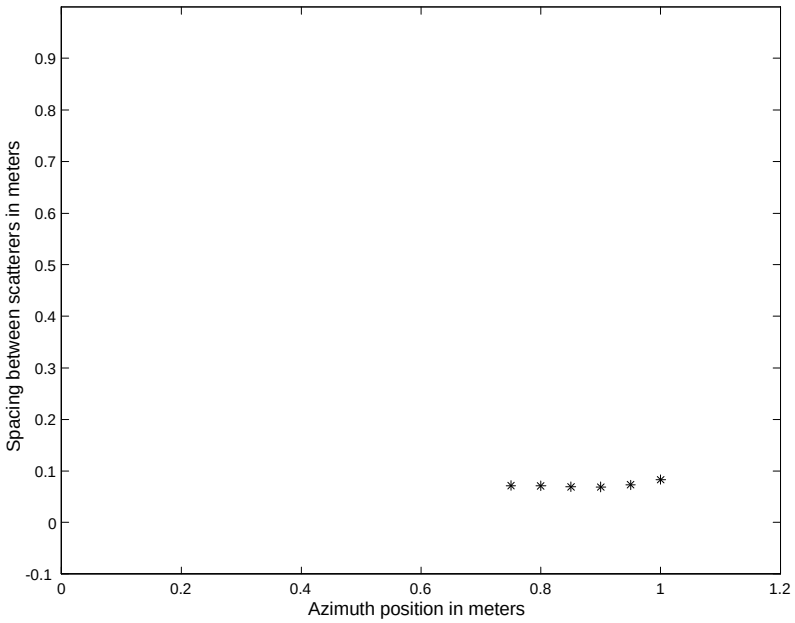

Figure 2.38: Position plot of the distance between target at the same azimuth location as a function of azimuth

2.9 Buried Pipe Measurement

Figure 2.39 shows the measurement setup for a pipe buried in a large plastic tub filled with low loss sand with an approximate real relative permittivity of 4. Figure 2.40 shows a photograph of the measurement setup showing the radar and antennas.

Each measurement profile consists of 140 frequency steps starting from 600 MHz with a step size of 4 MHz. A 2 inch diameter pipe was buried 10 cm below the surface. Radar data was captured by moving the transmit and receive antenna across the surface at position intervals of 0.02 m The antennas were standard broadband bow-tie antennas, separated by 10 cm and co-polarized with TX/RX polarization aligned with the length of the pipe. Figure 2.41 shows the results for processing the raw data using the standard windowed IFFT processing (a) and the MPM processing with amplitude target selection (b). Both Figure 2.41(a) and (b) clearly show the surface, pipe and bottom of the tub reflections, while

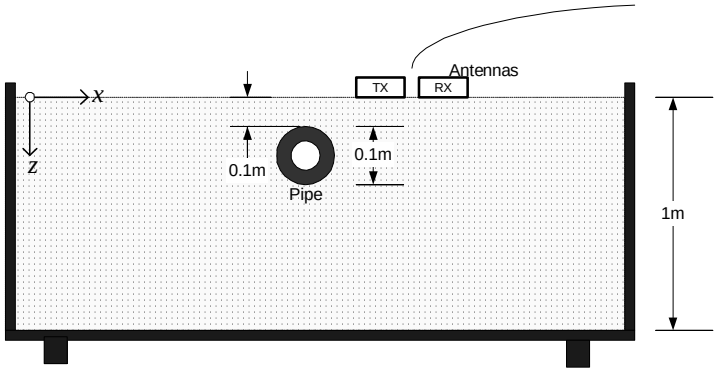

Figure 2.39: Measurement setup for pipe buried in a large plastic tub

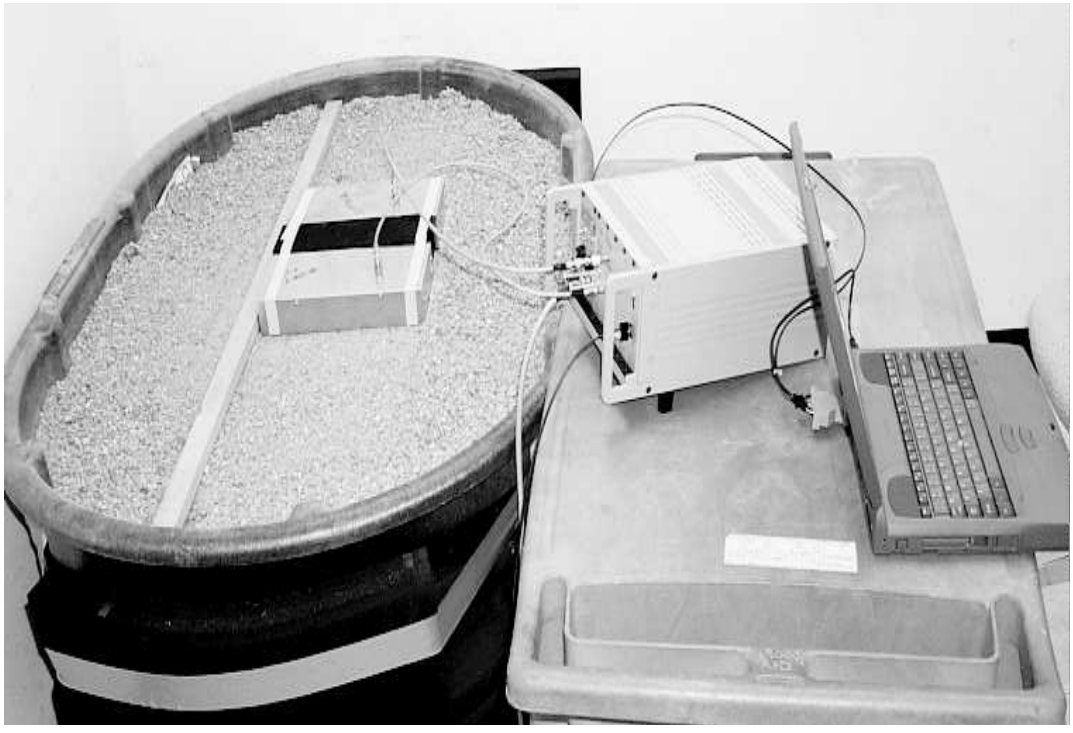

Figure 2.40: Picture of the measurement setup for the buried pipe measurement

only Figure 2.41(a) shows the side reflections from the tank walls. These reflections are not visible in Figure 2.41(b) as a result of limiting the number of principle eigenvectors based on their energy in their singular values. A cuttoff energy threshold was chosen to highlight the antenna coupling, pipe reflections and bottom of the pit. The same approach was taken when processing Figure 2.37. However as can be seen by the target positions for depths greater than 0.5m, some energy for these side reflections are evident.

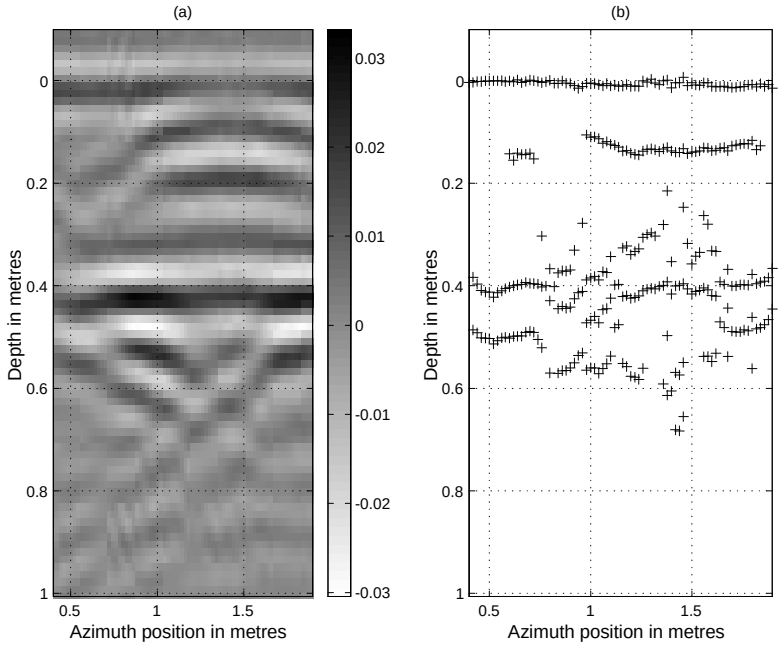

Figure 2.41: Images of the processed radar data after background subtraction. Figure (a) plots the real part of the radar impulse response. Figure (b) plots the position of the target vectors estimated from the MPM algorithm as a function of position.

Figure 2.42 shows the spacing between pipe and the surface reflectors at the same azimuth location. This figure shows that the distance between these reflections is approximately 10 cm which compares well with measured distances (assuming a relative permittivity of 4).

Figure 2.37 shows the processed results after the mean has been removed from

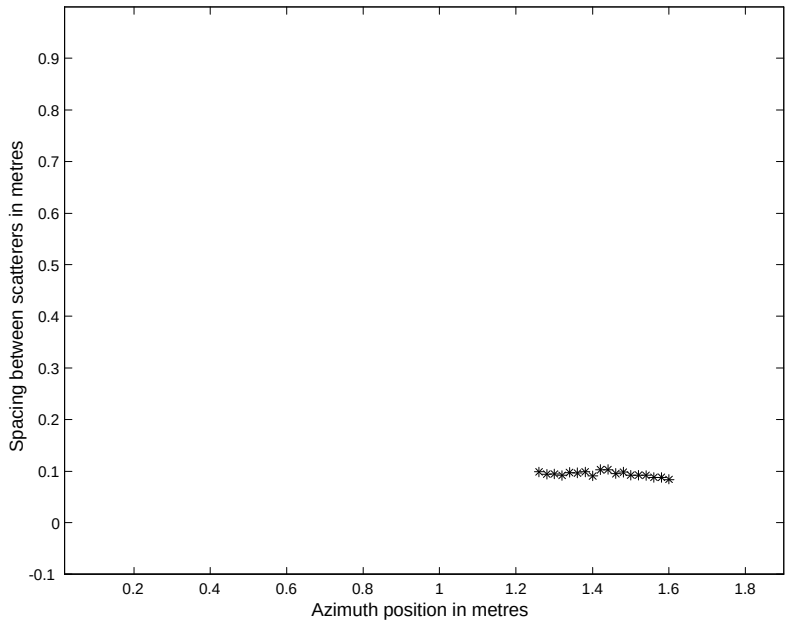

Figure 2.42: Position plot of the distance between pipe target and the ground surface at the same azimuth location as a function of azimuth.

the data. Both Figure 2.43(a) and (b) clearly show the pipe hyperbolic profile. In addition, Figure (b) shows that the target response shown in Figure 2.37(a) is made up of two reflections separated by a distance of 0.1 m assuming a relative permittivity of 4. Since this maps to a free space separation of 0.2 m, it is highly unlikely that this is the second reflection from the bottom of the pipe.

2.10 Conclusions

This chapter describes the development of a signal processing model based on the radar geometry and approximations to electromagnetic propagation in a lossy medium. The model is shown to be equivalent to the exponential model found in signal processing theory. The MPM algorithm is used to extract the parameters from the exponential model. These parameters are related to the GPR model parameters, providing valuable insight and understanding as to how these

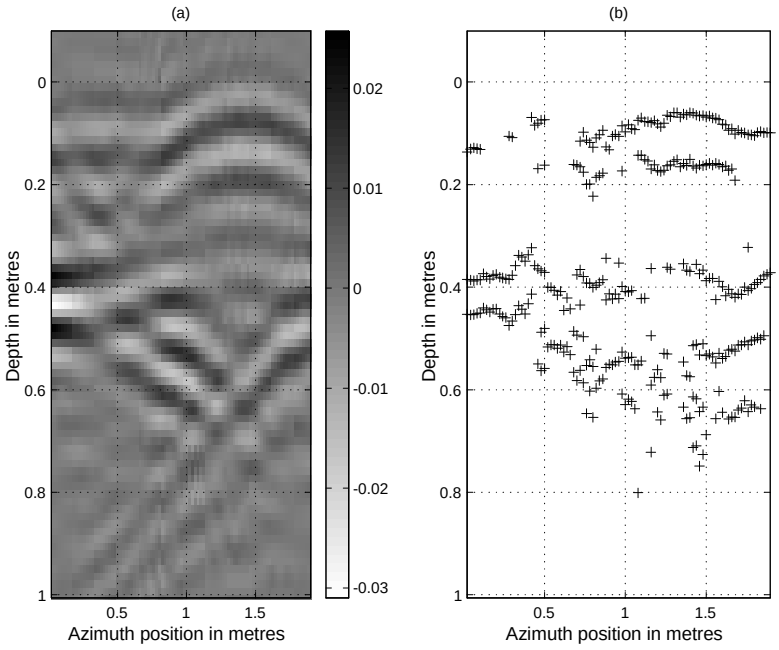

Figure 2.43: 2D Plots of the processed radar data after background subtraction. Figure (a) plots the real part of the radar impulse response. Figure (b) plots the position of the target vectors estimated from the MPM algorithm as a function of position.

parameters relate to the properties of a lossy medium. The performance of the algorithm is investigated for changing medium parameters. It is shown that the estimated parameter errors are complex functions of the conductivity of the medium, the target positions and the frequency in the medium. Based on the simulations the model approximations are valid for $\sigma_m < 1$ mS/m, for which the model error for linearizing k_m is much smaller than one. However, it is shown that it is difficult to define a cutoff conductivity for which the model is no longer valid, due to the model error dependence on the predicted model parameters. It is also recognized that a more detailed analysis of the errors is required to better understand the relationships between the model parameters and the resulting errors.

The algorithm is applied to real measured data, captured with the radar developed in this thesis. Given the constraints of limited calibration (no antenna data was available to allow its removal from the raw measured data as required by the algorithms developed in this chapter) and medium information (no material measurements were available to allow its effects to be removed from the signal processing model parameters to determine the actual GPR model parameters), the algorithm performed well for detecting the target positions for the two sets of field measurements.

Chapter 3

Fully Polarimetric GPR Model Based Processing

3.1 Introduction

A Ground Penetrating Radar is required to provide information that will allow for the detection and identification of subsurface features. In most GPR systems the only information available to perform this task is the magnitude of the target backscatter [82, 83, 16]. Some systems extract the phase of the radar returns providing the full vector nature of the received information and hence an extra dimension of information to meet the aforementioned requirements [79]. However, this is only for illumination with a single polarization.

The next logical development is to extend the received information to include the full vector nature of the scattered electromagnetic wave, and hence allow for the use of polarization sensitive processing of the GPR returns. The idea of polarization measurements in GPR is not new [54, 84]. Previous impulse systems have implemented simple polarimetric measurements by physically rotating a linearly polarized antenna [54, 84]. However, this method is both cumbersome, and limited, as it does not capture the complete scattering matrix of the target.

Roberts [24] showed the importance of GPR polarization data in his PhD dissertation on the *Analysis and Modelling of GPR Polarization*. Data was captured using a low frequency impulse GPR that simultaneously measured both the horizontal and vertical polarizations of the GPR returns. Since then various other researchers have investigated the use of polarimetric data to improve the information that can be extracted from a GPR sensor.

Narayanan and Xu [85] from the University of Nebraska developed a random noise polarimetric radar and investigated the usefulness of image processing and the Stokes matrix polarimetric representation, to enhance the target detection capabilities of their radar. Similar processing was also applied by Narayanan and Becker [86] to detect buried utilities using a SFCW GPR modified to take polarimetric measurements. More recent work at OSU [41] used the concept of scattering matrices and its characteristic features for the detection of unexploded ordinances. Radzevicius [87], in his PhD dissertation from the same university, provides both simulations and experimental results to show the significance of polarization measurements for GPR. The Technical University of Delft are also investigating the use of polarimetric data, captured using their fully polarimetric impulse radar [23], to aid in the characterization of radar returns.

Whereas most of the literature focuses on the analysis and performance of polarimetric representations, this thesis focusses on the extraction of target invariant parameters from the measured fully polarimetric data. The polarimetric feature vectors from various targets are simply compared – no complex target recognition algorithms are developed.

The chapter begins by extending the GPR model developed in the previous chapter from a single polarization to a fully polarimetric model. This model is extended to take into account the stepped frequency continuous wave (SFCW) radar modulation. The various GPR model parameters are related to the multi-snapshot exponential model parameters. A multi-channel version of the Matrix Pencil-of-Function Method algorithm is used to extract the target scattering parameters. The scattering matrices are transformed into the Huynen diagonal matrix form which the target invariant parameters are extracted. Finally real

measurements of various targets are presented and conclusions are drawn.

3.2 Contribution

The candidate's original contributions in this chapter are summarized as follows

- The development of a fully polarimetric GPR model based on approximations to the wavenumber in the medium.
- The comparison between the fully polarimetric GPR model and the multi-snapshot exponential model, which provides valuable insight into the understanding of the estimated exponential model parameters.
- The application of the Matrix Pencil-of-Function Method to fully polarimetric GPR data, using the information in all the polarization channels.
- The extraction of the Huynen target parameters for subsurface targets and the introduction of medium dependent and independent target parameters.

The authors initial findings in the field of SFCW GPR polarimetry were published at the fifth International GPR conference in Canada [88, 89] in 1994. This work looked at the co- and cross-polarization responses from measured SFCW GPR polarimetric data. The extension of this work to include the polarimetric modelling and Huynen target parameters was published later in a Landmine Detection conference in 1996 [43].

3.3 Polarimetric Model

This section extends the single polarization and single dimensional GPR model developed in Chapter 2 to a fully polarimetric radar model. A fully polarimetric radar measures the target backscatter with two linearly independent transmit and receive polarizations. Consider a GPR sensor, which includes an antenna

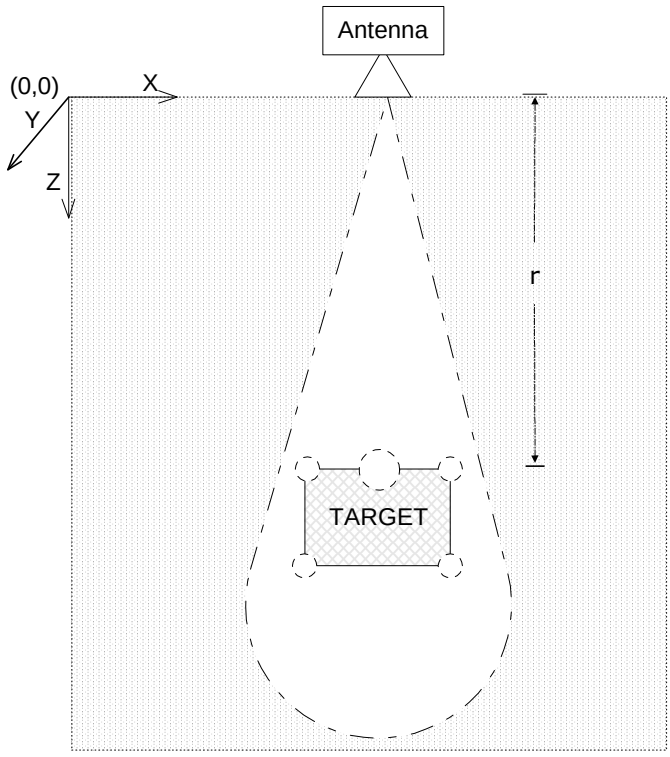

Figure 3.1: GPR/target geometry

that is capable of capturing complete polarimetric information, situated at the ground/air interface. Also consider some target buried at r metres below the surface. Figure 2.1 shows this radar/target geometry.

The model requires the following assumptions

- The soil medium has only a single layer. The target is buried in this layer.
- The soil is a linear, isotropic and low conduction loss medium.
- The radar is located such that the soil is in the far-field of the antenna. Plane wave propagation is assumed.
- The radar is located directly above the target and the direction of propagation of the EM wave is normal to the interface (i.e. $\hat{k} \cdot \mathbf{r} = z$).

- The radar cross-section of the target ($\sigma_{\{xy\}}$) is a function of frequency and polarization. The target is modelled using an exponential frequency behavior. Each target for each polarization is characterized by an amplitude and an exponential damping factor. The target damping factor is the same for all polarizations or the medium dispersion is greater than the target damping.

- There are no target to target multiple reflections.

The next section extends the single polarization model developed in Chapter 2 to a fully polarimetric model.

3.3.1 Propagation of an EM Wave in a Lossy Medium

In Chapter 2 equations were developed to describe the propagation of a horizontally polarized electric field in a lossy medium. In this section these equations are extended to describe the complete polarization of the propagating wave.

It is convenient to express the received or transmitted electric field in terms of a local coordinate system defined by the position and polarization of the radar antenna system. This is in accordance with the backscatter alignment convention (BSA) (or the radar alignment convention (RAC)) [90].

For linearly polarized antennas aligned along the $\hat{x}$ and $\hat{y}$ axis of their local Cartesian coordinate system, the electrical field propagating in the positive $\hat{z}$ direction can be described as

$$\mathbf{E}(z) \approx (\hat{\mathbf{x}}E_x + \hat{\mathbf{y}}E_y)\,\mathrm{Re}\left[\frac{1}{z}e^{j\left(\omega t - \widehat{k}_m z\right)}\right] \tag{3.1}$$

where

- $\hat{\mathbf{x}}$ and $\hat{\mathbf{y}}$ are the unit vectors that span the plane of the electric field **E.** The unit vector $\hat{\mathbf{x}}$ is defined such that it is perpendicular to the plane of

incidence [51]. The unit vector $\hat{\mathbf{y}}$ is defined, such that it is parallel to the plane of incidence.

- E_x is the electric field in the direction of unit vector $\hat{\mathbf{x}}$**,** and is often referred to as the *perpendicular (horizontal or E)* polarized component of the electric field *or the TE wave* [51].

- E_y is the electric field in the direction of unit vector $\hat{\mathbf{y}}$, and is often referred to as the *parallel (vertical or H)* polarized component of the electric field *or the TM wave* [51].

The complex amplitudes E_x and E_y can be expressed in terms of a polarization ratio. Noting that

$$\begin{aligned} \mathbf{E}(z) &\approx E_x \left(\hat{\mathbf{x}} + \hat{\mathbf{y}}\frac{E_y}{E_x}\right) \mathrm{Re}\left[\frac{1}{z} e^{j\left(\omega t - \widehat{k}_m z\right)}\right] \\ &\approx E_x \left(\hat{\mathbf{x}} + \hat{\mathbf{y}}\rho\right) \mathrm{Re}\left[\frac{1}{z} e^{j\left(\omega t - \widehat{k}_m z\right)}\right] \end{aligned} \tag{3.2}$$

and $E_x \neq 0$, the polarization ratio (ρ) can be expressed as

$$\rho = \left|\frac{E_y}{E_x}\right| e^{j\left(\varphi_y - \varphi_x\right)} = \tan\left(\alpha\right) e^{j\varphi} \tag{3.3}$$

where φ is the phase difference between the amplitude E_x and E_y, and $\tan\alpha$ is the ratio of their magnitudes. As time progresses, the peak of the electric field vector will trace out the locus of an ellipse [91], as shown in Figure 3.2. The parameters α, φ are known as the phasor descriptors of the polarization ellipse. Figure 3.2 shows that the polarization ellipse can also be described in terms of geometric descriptors, θ (orientation angle) and τ (ellipticity angle).

These parameters provide a more intuitive understanding of the ellipse shape and orientation than the phasor descriptor. The phase and geometric descriptors are related by simple trigonometric identities

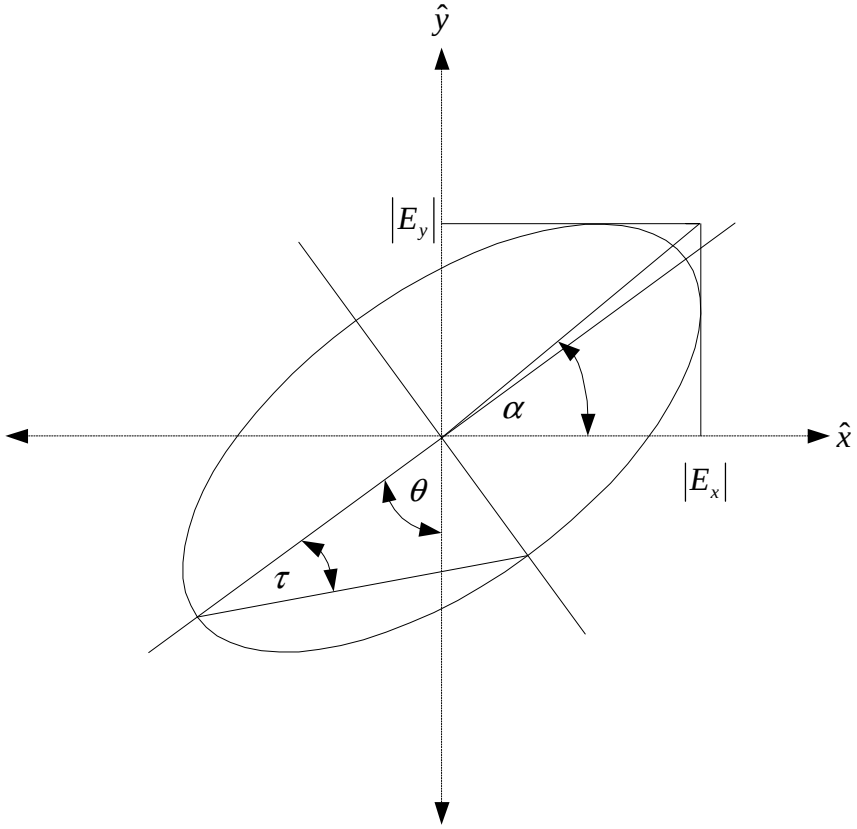

Figure 3.2: Polarizarion Elipse

$$\begin{aligned} \tan 2\theta &= \tan 2\alpha \cos\varphi \\ \sin 2\tau &= \sin 2\alpha \sin\varphi \end{aligned} \tag{3.4}$$

The above calculations lead to ambiguities in the estimation of θ, and hence it is necessary to make the following phase adjustment [39]

$$\theta = \begin{cases} \theta + \frac{\pi}{2} & if \quad \alpha > \frac{\pi}{4} \\ \theta + \pi & if \quad \alpha \leq \frac{\pi}{4} \quad and \quad \theta < 0 \end{cases} \tag{3.5}$$

3.3.2 Scattering From a Target

The target backscatter, for illumination with an arbitrary transmit and receive polarization, can be represented by the target scattering matrix, $\mathbf{s}_{\{xy\}}$ [92], such that

$$\mathbf{s}_{\{xy\}} = \begin{bmatrix} s_{xx} & s_{xy} \\ s_{yx} & s_{yy} \end{bmatrix} \tag{3.6}$$

where $(\{xy\})$ defines the polarization basis. From Chapter 2, each element of this matrix is given by

$$s_{\{xy\}} = s_{o\{xy\}} \exp\left(\gamma_{\{xy\}} \frac{k}{k_o}\right) \tag{3.7}$$

The scattering matrix is a linear transformation that maps the electric field incident on the target to the scattered electric field. For a Cartesian coordinate system spanned by the unit vectors, $(\hat{x}, \hat{y}, \hat{z})$, the scattered electric field from the target $\mathbf{E}^s$ is hence related to the incident electric field $\mathbf{E}^i$ by Equation 3.8.

$$\mathbf{E}^s(z,\omega) \approx \left[\hat{\mathbf{x}}\left(s_{xx}E_x^i + s_{xy}E_y^i\right) + \hat{\mathbf{y}}\left(s_{yx}E_x^i + s_{yy}E_y^i\right)\right] \mathrm{Re}\left[\frac{e^{j\left(\omega t - \hat{k}_m z\right)}}{z}\right] \tag{3.8}$$

It is often more convenient to express Equation 3.8 in a vector matrix form [93], such that

$$\mathbf{E}^s(z,\omega) = \begin{bmatrix} E_x^s \\ E_y^s \end{bmatrix} \approx \mathrm{Re}\left[\frac{e^{j(\omega t - k_m z)}}{z}\right] \mathbf{s}_{\{xy\}} \begin{bmatrix} E_x^i \\ E_y^i \end{bmatrix} \tag{3.9}$$

3.3.3 Complete Polarization Radar Model

Consider a target at a distance d metres beneath the surface. Given that an electric field, $\mathbf{E}^t(\omega, d)$, is transmitted, then the received electric field $\mathbf{E}^r(\omega, d)$ at the radar origin is described by

$$\mathbf{E}^r(\omega,d) \approx \mathrm{Re}\left\{ \begin{array}{c} \frac{1}{d^2}\mathbf{s}_{\{xy\}}\mathbf{E}_o^t \exp\left(-2\alpha_m(\omega)d\right) \times \\ \exp\left(j\left(\omega t - 2\beta_m(\omega)d\right)\right) \end{array} \right\} \tag{3.10}$$

where

- $\mathbf{E}^r = \begin{bmatrix} E_x^r \\ E_y^r \end{bmatrix}$ is the electric field with initial conditions $\mathbf{E}_o^t = \begin{bmatrix} E_{x0}^t \\ E_{y0}^t \end{bmatrix}$.
- $\mathbf{s}_{\{xy\}}$ is the radar scattering matrix for a target buried at a depth of d metres below the surface, where each element of the scattering matrix is characterized by a complex amplitude and an exponential damping factor

$$\mathbf{s}_{\{xy\}} = \begin{bmatrix} s_{oxx}\exp\left(\gamma_{xx}\frac{k}{k_o}\right) & s_{oxy}\exp\left(\gamma_{xy}\frac{k}{k_o}\right) \\ s_{oyx}\exp\left(\gamma_{yx}\frac{k}{k_o}\right) & s_{oyy}\exp\left(\gamma_{yy}\frac{k}{k_o}\right) \end{bmatrix}$$

Assuming that there are a number of targets situated at discrete locations (d_p) from the radar, then the received electric field, $\mathbf{E}^r(\omega)$, at the radar origin can be described as

$$\mathbf{E}^r(\omega) = \sum_{p=0}^{P-1} \mathbf{E}_p^r(\omega) \tag{3.11}$$

where

- P is the number of targets.
- $\mathbf{E}_p^r(\omega)$ is the electric field contribution from the p^{th} target at position d_p (i.e. $\mathbf{E}^r(\omega, d_p) \rightarrow \mathbf{E}_u^r(\omega)$).

Substituting Equation 3.10 into Equation 3.11 results in the complete polarization GPR model

$$\mathbf{E}^r(\omega) \approx \text{Re}\left\{ \sum_{p=0}^{P-1} \begin{array}{l} \frac{1}{d_p^2}\mathbf{s}_{\{xy\}}\mathbf{E}_o^t \exp\left(-2\alpha_m(\omega)d_p\right) \times \\ \exp\left(j\left(\omega t - 2\beta_m(\omega)d_p\right)\right) \end{array} \right\} \tag{3.12}$$

3.3.4 Target Invariant Parameters

Equation 3.6 provides the basic form of the scattering matrix. It is useful to extract target parameters from the scattering matrix that will provide unique target information that is independent of the transmit and receive antenna polarization.

Background

Numerous polarization representations exist. Early work by Sinclair and Kennaugh introduced the concept of the polarimetric representation and the null polarization states [94]. Later Graves introduced the polarization power scattering matrix and considered optimum polarization states for maximum power transmission and reception [95]. Arguably, the most important contribution was Huynen's polarimetric representation which related various parameters to physical scattering mechanisms [96, 97]. This early research has been revisited many times by numerous researchers over the past decade [98, 99, 100, 101, 102].

More recently, other polarization descriptors have been developed. In 1991 Chamberlain [103] introduced the transient polarization response (TPR) to utilize the complete polarization information for automatic target recognition of

aircraft. The TPR was defined as the locus of the far-field scattered electric field resulting from a plane, circularly polarized wideband waveform incident on a target [103]. Chamberlain claimed that the TPR was suitable for a fully polarimetric target description, based on the fact that the TPR was constructed from s_{xx}, s_{xy} and s_{yy}. However, when one compares his results to the standard Huynen diagonal matrix, it is clear that the TPR contains no information about the relative amplitude of the pseudo–eigenvalues of the scattering matrix. He seemed to overlook the fact that information is lost when combining the measured elements of the scattering matrix. The TPR was also used by Steedly [39] and later Wang [104] in combination with parametric modelling with the goal of extracting polarimetric features for automatic target recognition of aircraft.

More recently Higgins from Ohio State University [41] has characterized fully polarimetric GPR data by considering a transformation of the pseudo-eigenvalues of the scattering matrix with a linear polarization basis. He introduced the estimated linearity factor (ELF) which is simply a normalized metric between the co- and cross-polarization eigenvalues of the scattering matrix, described as,

$$ELF = \frac{\left|\lambda_{\parallel}\right| - \left|\lambda_{\perp}\right|}{\left|\lambda_{\parallel}\right| + \left|\lambda_{\perp}\right|} \tag{3.13}$$

He also extracted the orientation angle from the eigenvectors corresponding to $\lambda_{\parallel}$ and $\lambda_{\perp}$. These parameters are independent of the effect of propagation loss in the medium, and are related to the Huynen parameters used in this thesis.

Huynen [97] Target Parameters

The Huynen model (or Huynen diagonal matrix) for the p^{th} scattering matrix can be determined by transforming the scattering matrix $\mathbf{s}_{\{xy\}p}$ from one polarization basis to another $\mathbf{s}'_{\{AB\}p}$ as is shown in Equation 3.14

$$\mathbf{s}'_{\{AB\}p} = \mathbf{U}(\rho_{xnull})^{T}\mathbf{s}_{\{xy\}p}\mathbf{U}(\rho_{xnull}) \tag{3.14}$$

where:

$$\mathbf{s}'_{\{AB\}p} = \begin{bmatrix} \chi_1 & 0 \\ 0 & \chi_2 \end{bmatrix} = M \begin{bmatrix} \exp(jv) & 0 \\ 0 & \exp(-jv)\tan^2\gamma^h \end{bmatrix} \exp(-j\xi) \quad (3.15)$$

$\{AB\} = \{\rho_{xnull}\rho^*_{xnull}\}$, ρ is the polarization ration and $\mathbf{U}(\rho)$ is a 2×2 unitary polarization basis transformation matrix given by [100]

$$\mathbf{U}(\rho) = \frac{1}{\sqrt{1-\rho\rho^*}} \begin{bmatrix} 1 & j\rho^* \\ \rho & -j \end{bmatrix} \quad (3.16)$$

The formulation of $\mathbf{U}$ is such that it conforms with the IEEE standard-149 1979 [100].

The polarization state that diagonalizes Equation 3.14 is known as the characteristic cross polarization null (ρ_{xnull}) and was originally proposed by Kennaugh [91]. It describes the polarization state for maximum received power. The co-polarization values χ_1 and χ_2 are referred to as the pseudo-eigenvalues of the matrix $\mathbf{s}_{\{xy\}}$, since they are a solutions to the equation $\mathbf{sx} = \chi\mathbf{x}^*$. This differs from the standard eigenvalue equation which is of the form, $\mathbf{sx} = \chi\mathbf{x}$. The conjugate of the reflected vector is due to the difference in the coordinate systems of the incident and reflected wave [92]. It is important to note that the eigenvalues of $\mathbf{s}_m$ are not necessarily equal to χ_1 and χ_2, unless $\mathbf{s}_m$ is symmetric [101].

The six target invariant parameters, extracted from Equation 3.15 and 3.16, are listed below

- M is the backscatter amplitude, where $M = |\chi_1|$.
- ξ is the absolute phase, where $\xi = \frac{1}{2}(\angle\chi_1 + \angle\chi_2)$.
- γ^h is the characteristic angle, where $\tan\gamma^h = \left|\frac{\chi_2}{\chi_1}\right|$ and $0 \leq \gamma^h \leq 45°$. It represents the ratio of the amplitude of the diagonal elements of the matrix.
- ν is the target skip angle, where $v = \frac{1}{2}(\angle\chi_1 - \angle\chi_2)$ and $-45° \leq \nu \leq 45°$. It represents the phase difference between the diagonal elements of the matrix.

- ρ is the polarization state of the EM field that yields maximum power, described by τ and θ.

Theoretically, the Huynen target parameters provide valuable insight into a phenomenological understanding of the various scattering mechanisms [97, 105, 106]. However, practically the parameters M, ξ and v are less viable for use as feature vectors for subsurface target recognition due to the difficulty in estimating them. The parameters M and ξ represent relative measures of the amplitude and phase of the scattering matrix respectively and are dependent on EM losses and dispersion in the medium. The skip angle v is related to ξ, and is thus also dependent on the properties of the medium. In addition, for a noise contaminated scattering matrix, the variance of ξ and v is dependent on the variance of χ_1 and χ_2, i.e. $var(\xi) = var(v) = \frac{1}{2}(var(\chi_1) + var(\chi_2))$. Hence, for targets where $\chi_1 >> \chi_2$, such that the SNR of χ_2 is small, the estimates for the angle χ_1 are poor. The parameter M stills provide valuable information about the magnitude of the scattering from the target, however the properties of the medium must be taken into consideration.

The classical method for solving for the Huynen parameters is based on finding the cross-polarization nulls by setting the cross-polarization terms in the matrix $s_{\{AB\}}$ in Equation 3.15 to zero, and using the resultant polarization state to construct the Huynen diagonal matrix. However, a solution is only guaranteed for the monostatic and reciprocal radar structure [100]. Kotinski [101] provides for a solution which is valid for both monostatic and bistatic configurations that follows a similar argument to Grave [95]. The solution is based on the analysis of the received scattered EM wave, whose normalized power density for the p^{th} target $\left((P_w)_p\right)$ is given by

$$(P_w)_p = \left(\mathbf{E}_p^r\right)^H \mathbf{E}_p^r = \left(\mathbf{E}_p^r\right)^H \mathbf{G}_p \mathbf{E}_p^r \tag{3.17}$$

where $\mathbf{G}_p = \mathbf{s}_p^* \mathbf{s}_p$ (Graves power matrix [95]). Since $\mathbf{G}_p$ is a Hermitian matrix, it can be diagonalized by a similarity transform such that

$$\mathbf{G}_p^{'} = \mathbf{U}\left(\rho_{opt}\right)^{*T} \mathbf{G}_p \mathbf{U}\left(\rho_{opt}\right) \tag{3.18}$$

where $\mathbf{U}\left(\rho_{opt}\right) = \mathbf{U}(\rho_{xnull})$. Hence, the same unitary matrix that diagonalizes $\mathbf{G}_p$ by a similarity transform, diagonalizes the scattering matrix via a congruent transform [95]. The polarization state (ρ_{opt}) that maximizes the power received from the target backscatter is the same as the ρ_{xnull} which diagonalizes the scattering matrix $\mathbf{s}_{m.}$ In addition, eigenvalues of the diagonal matrix $\psi_{1,2}$ are related to the psuedo-eigenvalues of the scattering matrix by $\psi_{1,2} = \left|\chi_{1,2}\right|^2$. Evaluating Equation 3.18 and relating to the power form of the Huynen diagonal matrix, the diagonal Graves matrix can be written as

$$\mathbf{G}_p^{'} = \mathbf{s}_p^{'*}\mathbf{s}_p^{'} = \begin{bmatrix} \psi_1 & 0 \\ 0 & \psi_2 \end{bmatrix} = M^2 \begin{bmatrix} 1 & 0 \\ 0 & \tan^4 \gamma_p^h \end{bmatrix} \tag{3.19}$$

The Huynen parameters can be determined by calculating the eigenvalues and eigenvectors of the measured Graves power matrix, $\mathbf{G}_p$ [101]. The eigenvectors of this matrix $E_{opt_{1,2}}$ correspond to the optimum polarization states $\left(\rho_{opt}, \rho_{opt}^*\right)$, that result in maximum received power for a given target. In addition, $\left(\rho_{opt}, \rho_{opt}^*\right)$ is orthonormal.

Since by calculating the Graves power matrix the phase information of the eigenvalues is lost, this algorithm is not able to provide an estimate for the skip angle (v). However, one can recover the target skip angle for the monostatic and reciprocal radar case $(s_{hv} = s_{vh})$, by calculating the diagonal elements of $\mathbf{s}_{\{AB\}p}^{'}$, such that

$$\boldsymbol{\chi}_1 = \left(1 + \rho\rho^*\right)^{-1}\left(\rho^2 s_{vv} + 2\rho s_{hv} + s_{hh}\right) \tag{3.20}$$

$$\boldsymbol{\chi}_2 = -\left(1 + \rho\rho^*\right)^{-1}\left(\rho^{*^2} s_{hh} - 2\rho^* s_{hv} + s_{vv}\right) \tag{3.21}$$

The skip angle is then given by $v = \frac{1}{2}\left(\angle\chi_1 - \angle\chi_2\right)$ and $-45^\circ \leq \nu \leq 45^\circ$.

Note that the ELF parameter used by Higgins [41] relates to the Huynen characteristic angle in the following manner

$$ELF = \frac{1 - \tan^2 \gamma^h}{1 + \tan^2 \gamma^h} \tag{3.22}$$

3.4 SFCW Modulation

The model developed in the previous sections is a general propagation model that is independent of the radar system modulation. This section extends the model to include the SFCW modulation scheme.

The polarimetric radar differs from the single polarization system in that it needs to transmit and receive two orthogonal polarizations to allow it to capture the complete target scattering matrix as defined in Equation 3.6. The first step in developing these equations is to choose an orthogonal polarization basis. The polarization basis is typically determined by the radar antenna polarization and orientation. A linear polarization with a polarization basis aligned with the $\hat{x}$ and $\hat{y}$ unit vectors of the Cartesian coordinate system will be chosen. A block diagram for the radar geometry is shown in Figure 3.3.

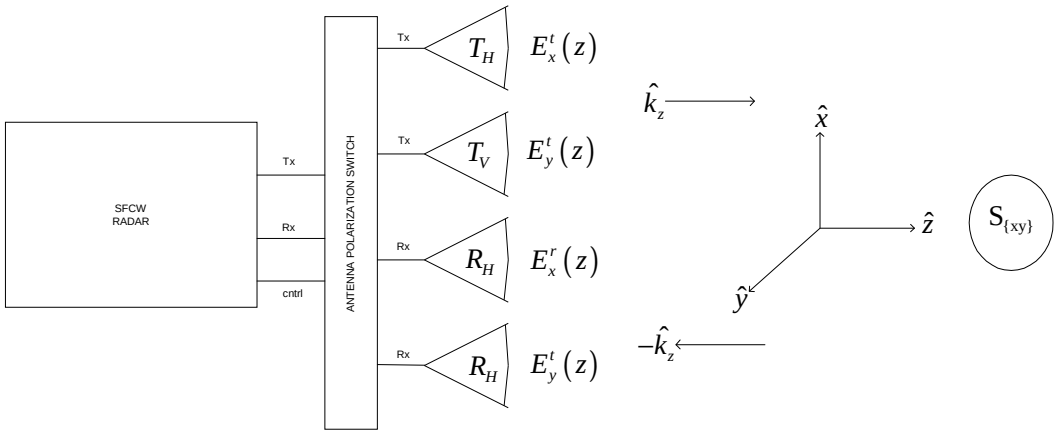

Figure 3.3: Block diagram of SFCW Polarimetric radar showing the defined coordinate system

The following measurements are required to capture the electric field correspond-

ing to the elements of the scattering matrix

- $E^r_{xx}(f)$ – transmit with the antenna aligned with $\hat{x}$ axis and receive with an antenna aligned with $\hat{x}$ axis.
- $E^r_{xy}(f)$ – transmit with the antenna aligned with $\hat{x}$ axis and receive with an antenna aligned with $\hat{y}$ axis.
- $E^r_{yx}(f)$ – transmit with the antenna aligned with $\hat{y}$ axis and receive with an antenna aligned with $\hat{x}$ axis.
- $E^r_{yy}(f)$ – transmit with the antenna aligned with $\hat{y}$ axis and receive with an antenna aligned with $\hat{y}$ axis.

Each measurement for the received electric field will consist of four electrical field measurements, namely $E^r_{xx}(f), E^r_{yx}(f), E^r_{xy}(f), E^r_{yy}(f)$, which can be written in matrix form as

$$\mathbf{E}^r(f) = \begin{bmatrix} E^r_{xx}(f) & E^r_{yx}(f) \\ E^r_{xy}(f) & E^r_{yy}(f) \end{bmatrix} \tag{3.23}$$

Since $\begin{bmatrix} E^r_{xx}(f) & E^r_{yx}(f) \\ E^r_{xy}(f) & E^r_{yy}(f) \end{bmatrix}$, and not $\begin{bmatrix} E^r_{x}(f) \\ E^r_{y}(f) \end{bmatrix}$ is measured directly, it is more convenient to write Equation 3.12 as

$$\mathbf{E}^r(\omega) \approx \mathrm{Re}\left\{ \sum_{p=0}^{P-1} \begin{array}{c} \frac{1}{d_p^2}\mathbf{s}_{\{xy\}}\mathbf{I}\mathbf{E}^t_o \exp\left(-2\alpha_m(\omega)d_p\right) \times \\ \exp\left(j\left(\omega t - 2\beta_m(\omega)d_p\right)\right) \end{array} \right\} \tag{3.24}$$

where $\mathbf{I}$ is a 2×2 identity matrix. The received electric field $\mathbf{E}^r_x(\omega)$ is converted to a voltage by the receiver. In the coherent receiver, the signal is mixed down to baseband using an IQ (inphase/quadrature) demodulator. Since the received signal is bandlimited, the I and Q channels can be combined to form an analytic signal [28]. Including the effects of thermal noise at the input to the radar receiver

(modelled as a zero mean Gaussian process, $w_{\{xy\}}(f)$), the received signal at the input to the radar processor is given by

$$\begin{aligned} v^r_{measured\{xy\}}(f) \approx G_s(f) G_{t\{xy\}}(f) G_{r\{xy\}}(f) v^t_{\{xy\}o} \times \\ \sum_{p=1}^{P-1} \frac{s_{\{xy\}}}{d_p^2} \exp\left(-4\pi\alpha_{m1}\frac{f}{v}d_p - 2\alpha_{m2}d_p\right) \times \\ \exp\left[-j\left(\frac{4\pi f}{v}\beta_{m1}d_p + 2\beta_{m2}d_p\right)\right] + w_{\{xy\}}(f) \end{aligned} \tag{3.25}$$

where

- $v^r_{measured\{xy\}}(f)$ is the RMS voltage at the terminal of the receive antenna, for each combination of the polarization channel $\{xy\}$.
- $G_{t\{xy\}}$ is the gain of the transmit antenna for the horizontal and the vertical polarization, respectively.
- $G_{r\{xy\}}$ is the gain of the receive antenna for the horizontal and the vertical polarization, respectively.
- G_s is the radar electronic gain.
- $V^t_{\{xy\}o}$ is the RMS voltage at the terminal of the horizontal and the vertically polarized transmit antenna, respectively – such that $V^t_{\{xy\}o} = \left\{V^t_{xo}, V^t_{yo}\right\}$.

It is possible to remove the effects of the system and antenna gain responses from the measured data by dividing the received data $V^r_{\{xy\}}(f)$ by the measured antenna and radar electronics responses.

$$v^r_{\{xy\}}(f) \approx \frac{v^r_{measured\{xy\}}(f)}{V^t_{\{xy\}o} G_s(f) G_{t\{xy\}}(f) G_{r\{xy\}}(f)} \tag{3.26}$$

Equation 3.24 and 3.26 assume that there is no cross-coupling between the polarization channels. In practice, this is not the case. The received scattering matrix

is typically distorted by cross-coupling between the polarization channels, such that

$$\begin{aligned} \mathbf{s}_{measured\{xy\}} &= \mathbf{R}_{\{xy\}}\mathbf{s}_{\{xy\}}\mathbf{T}_{\{xy\}} \\ &= \begin{bmatrix} R_{xx} & R_{xy} \\ R_{yx} & R_{yy} \end{bmatrix} \begin{bmatrix} s_{xx} & s_{xy} \\ s_{yx} & s_{yy} \end{bmatrix} \begin{bmatrix} T_{xx} & T_{xy} \\ T_{yx} & T_{yy} \end{bmatrix} \end{aligned} \tag{3.27}$$

where $\mathbf{R}_{\{xy\}}$ and $\mathbf{T}_{\{xy\}}$ are the transmit and receive channel distortion matrices and $\mathbf{s}_{\{xy\}}$ is the target scattering matrix. Algorithms exist to remove the distortion from the measured scattering matrix [93], however they all require knowledge of the scattering from known targets. This is a complex problem requiring an accurate measurement facility and detailed analysis of the scattering measurements of known targets, buried in different media. Due to the absence of adequate measurement facilities and the requirement to limit the scope of this thesis, calibration is assumed for all simulated data and ignored for measured data. Ignoring calibration for the measured data results in scattering matrices which differ from their theoretical values. Neither Xu [85] nor Higgins [41] present any discussion on calibration for their GPR polarimetric measurements.

Applying the calibration to Equation 3.25, Equation 3.26 can be rewritten in a more convenient matrix form

$$\begin{aligned} \mathbf{V}^r(f) \approx \sum_{p=1}^{P-1} \frac{\mathbf{s}_{\{xy\}}}{d_p^2} \exp\left(-4\pi\alpha_{m1}\frac{f}{v}d_p - 2\alpha_{m2}d_p\right) \times \\ \exp\left[-j\left(\frac{4\pi f}{v}\beta_{m1}d_p + 2\beta_{m2}d_p\right)\right] + \mathbf{W}'_{\{xy\}}(f) \end{aligned} \tag{3.28}$$

where

- $\mathbf{V}^r(f) = \begin{bmatrix} v^r_{xx}(f) & v^r_{xy}(f) \\ v^r_{yx}(f) & v^r_{yy}(f) \end{bmatrix}$ is received voltage at the input to the radar processor.

- $\mathbf{W}'_{\{xy\}}(f) = \begin{bmatrix} w'_{xx}(f) & w'_{xy}(f) \\ w'_{yx}(f) & w'_{yy}(f) \end{bmatrix}$ is the thermal noise in each channel, calibrated with reference to the antenna and radar gain characteristics.

Consider transmitting N discrete frequencies over a bandwidth B, from a start frequency f_L to $f_L + B$, such that $f = f_o + n\Delta f$. The discrete version of Equation 3.28 can then be given by Equation 3.29.

$$\begin{aligned} \mathbf{V}^r[n] \approx & \sum_{p=1}^{P-1} \frac{1}{d_p^2} \mathbf{s}_{\{xy\}} \exp\left(-2\alpha_{m2} d_p\right) \times \\ & \exp\left(-4\pi\alpha_{m1} \frac{f_o + n\Delta f}{v} d_p\right) \times \\ & \exp\left[-j\left(4\pi \frac{f_o + n\Delta f}{v} \beta_{m1} d_p + 2\beta_{m2} d_p\right)\right] + \mathbf{W}'_{\{xy\}}[n] \end{aligned} \quad (3.29)$$

Each element of $\mathbf{V}^r[n]$ has the same form as the standard exponential model found in the signal processing literature, namely

$$\begin{aligned} \mathbf{V}^r[n] = \begin{bmatrix} v_{xx}[n] & v_{yx}[n] \\ v_{xy}[n] & v_{yy}[n] \end{bmatrix} \approx & \begin{bmatrix} \sum_{p=0}^{P-1} (b_{xx})_p (z_{xx})_p^n & \sum_{p=0}^{P-1} (b_{yx})_p (z_{yx})_p^n \\ \sum_{p=0}^{P-1} (b_{xy})_p (z_{xy})_p^n & \sum_{p=0}^{P-1} (b_{yy})_p (z_{yy})_p^n \end{bmatrix} + \\ & \begin{bmatrix} w'_{xx}[n] & w'_{xy}[n] \\ w'_{yx}[n] & w'_{yy}[n] \end{bmatrix} \end{aligned} \quad (3.30)$$

If either one of the following assumptions are made, namely

- The target damping factor $\left(\gamma_{\{xy\}}\right)_p$ is the same for all polarizations i.e.

$$\gamma_p = (\gamma_{xx})_p = \left(\gamma_{yx}\right)_p = \left(\gamma_{xy}\right)_p = \left(\gamma_{yy}\right)_p \quad (3.31)$$

  or

- The dispersion due to the medium $(2\pi\alpha_{m1}d_p)$ is much greater than the dispersion due to the target i.e. $\left(2\pi\alpha_{m1}d_p >> \left(\gamma_{\{xy\}}\right)_p\right)$.

then Equation 3.30 can be simplified as follows

$$\begin{aligned}
\overline{\mathbf{V}}^{r}[n] &\approx \begin{bmatrix} (v_{xx}^{r})[n] & (v_{yx}^{r})[n] \\ (v_{xy}^{r})[n] & (v_{yy}^{r})[n] \end{bmatrix} \\
&\approx \begin{bmatrix} \sum_{p=0}^{P-1}(b_{xx})_p & \sum_{m=0}^{P-1}(b_{yx})_p \\ \sum_{p=0}^{P-1}(b_{xy})_p & \sum_{m=0}^{P-1}(b_{yy})_p \end{bmatrix} \begin{bmatrix} z_p[n] & 0 \\ 0 & z_p[n] \end{bmatrix} + \\
&\quad \begin{bmatrix} w_{xx}^{'}[n] & w_{xy}^{'}[n] \\ w_{yx}^{'}[n] & w_{yy}^{'}[n] \end{bmatrix}
\end{aligned} \tag{3.32}$$

This is the standard form for the multiple snapshot exponential model. In the absence of these assumptions, it would not be possible to apply the computationally efficient parameter estimation techniques available to detect the parameters of the multi-dimensional exponential model [39, 104, 40]. This fact is not dealt with by any of the literature [39, 104]. Steedly [39] simply assumes a model with the same form as Equation 3.30. No mention is given of the fact that the target damping factor is independent of polarization. Wang *et al.* [104] simply make the assumption that the target is point scatterer i.e., $\gamma_p = 0$, in order to make their model valid.

Comparing Equation 3.32 to Equation 3.29 and applying the assumptions described in Equation 3.31, the exponential signal processing model parameters can be related to the fully polarimetric GPR model.

This can be seen more clearly by writing Equation 3.32 as

$$\overline{\mathbf{V}}^{r}[n] \approx \overline{\mathbf{Y}}[n] + \overline{\mathbf{W}}[n] \tag{3.33}$$

where the multi-snapshot exponential model is given by $\overline{\mathbf{Y}}[n]$, such that

$$\mathbf{Y}[n] = \begin{bmatrix} \sum_{p=0}^{P-1}(b_{xx})_p & \sum_{m=0}^{P-1}(b_{yx})_p \\ \sum_{p=0}^{P-1}(b_{xy})_p & \sum_{m=0}^{P-1}(b_{yy})_p \end{bmatrix} \begin{bmatrix} z_p[n] & 0 \\ 0 & z_p[n] \end{bmatrix} \tag{3.34}$$

Noting that $\mathbf{b}_{\{xy\}p}$ and z_p are given by

$$\mathbf{b}_{\{xy\}p} = A_{\{xy\}p} \exp(j\theta_{\{xy\}p}) \tag{3.35}$$

$$\mathbf{z}_p = \exp\left[\left(\lambda_p + j2\pi r_p\right)\Delta r\right] \tag{3.36}$$

then

$$A_{\{xy\}p} = \frac{\left|\mathbf{s}_{\{xy\}p}\right|}{d_p^2} \exp\left(-2\alpha_{m2}d_p + 2\pi\alpha_{m1}r_o d_p\right) \exp\left(\gamma_p\beta_{m2} - \pi\gamma_p\beta_{m1}r_o\right) \tag{3.37}$$

$$\theta_{\{xy\}p} = -\tau_{\{xy\}m} - 2\beta_{m2}d_p + 2\pi\beta_{m1}r_o d_p - \gamma_p\alpha_{m2} + \pi\gamma_p\alpha_{m1}r_o \tag{3.38}$$

$$\lambda_p = 2\pi\alpha_{m1}d_p - \pi\gamma_p\beta_{m1} \tag{3.39}$$

$$r_p = \beta_{m1}d_p + \frac{1}{2}\gamma_p\alpha_{m1} \tag{3.40}$$

$$\Delta r = -\frac{2\Delta f}{v} \tag{3.41}$$

$$r_o = -\frac{2f_o}{v} \tag{3.42}$$

The parameter $A_{\{xy\}p}$ is the measured target amplitude for each transmit/receive polarization pair; $\theta_{\{xy\}p}$ is the target scattering phase for each transmit/receive polarization pair; λ_p is the target damping factor; d_p is the free space target position and p is the p^{th} target. Given the parameters of the medium, $\alpha_{m1}, \alpha_{m2}, \beta_{m1}$ and β_{m2}, the target damping factor γ_p and scattering amplitude s_p can be determined. Note that the target position d_p is a function of both the model parameter z_p and the target scattering damping parameter γ_p.

3.5 Parameter Estimation

In this section an algorithm is presented to extract the Huynen target parameters from the fully polarimetric raw radar data. This involves two steps. The first step estimates the target position, damping factor, scattering amplitudes and scattering phase. The second step estimates the Huynen target parameters from

the scattering matrix. The model error for the target parameter estimates, will also be presented.

3.5.1 Multi-Snapshot Matrix Pencil-of-Function Method

In Chapter 2 it was shown that there exist numerous sub-optimum statistical, yet computationally efficient, solutions to solving for the parameters of an exponential model in a least squares sense. In particular the MPM algorithm was described to provide this solution for single polarization data. This section presents a solution, based on the work of Chiang and Potter [64, 40, 71], that extends the single dimensional MPM to a fully polarimetric algorithm.

It was noted that solving for the poles of the exponential equation in a least square sense was equivalent to solving for the roots of the characteristic polynomial equation whose coefficients were the coefficients of a linear difference equation. Since Equation 3.32 is simply a matrix of four single polarization exponential models ($v_{\{xy\}}[n]$), it can be expressed as the solution to a set of linear difference equations

$$\begin{bmatrix} \sum_{p=0}^{P-1} c_p v_{xx}(i-p) & \sum_{p=0}^{P-1} c_p v_{xy}(i-p) \\ \sum_{p=0}^{P-1} c_p v_{yx}(i-p) & \sum_{p=0}^{P-1} c_p v_{yy}(i-p) \end{bmatrix} = \begin{bmatrix} 0 & 0 \\ 0 & 0 \end{bmatrix} \tag{3.43}$$

The coefficients of the linear difference equation are the same for all polarization channels (since z_n^p is constant for all polarizations). Hence, Equation 3.43 can be rewritten as

$$\sum_{p=0}^{P-1} c_p v_{xx}(i-p) = 0 \tag{3.44}$$

$$\sum_{p=0}^{P-1} c_p v_{xy}(i-p) = 0 \tag{3.45}$$

$$\sum_{p=0}^{P-1} c_p v_{yx}(i-p) = 0 \tag{3.46}$$

$$\sum_{p=0}^{P-1} c_p v_{yy}(i-p) = 0 \tag{3.47}$$

that is now in a form that one can directly apply the MPM method. The multi-snapshot LSE algorithm minimizes the sum of the errors in all channels when determining the model parameters, z_p and λ_p.

Consider a set of measurement vectors, such that

$$(\mathbf{v}_{xx})_0, (\mathbf{v}_{xx})_1, \ldots, (\mathbf{v}_{xx})_L \tag{3.48}$$

$$(\mathbf{v}_{xy})_0, (\mathbf{v}_{xy})_1, \ldots, (\mathbf{v}_{xy})_L \tag{3.49}$$

$$(\mathbf{v}_{yx})_0, (\mathbf{v}_{yx})_1, \ldots, (\mathbf{v}_{yx})_L \tag{3.50}$$

$$(\mathbf{v}_{yy})_0, (\mathbf{v}_{yy})_1, \ldots, (\mathbf{v}_{yy})_L \tag{3.51}$$

where

$$(\mathbf{v}_{xx})_i = \left[(v_{xx})_i, (v_{xx})_{i+1}, \ldots, (v_{xx})_{i+N-L-1}\right]^T \tag{3.52}$$

$$(\mathbf{v}_{xy})_i = \left[(v_{xy})_i, (v_{xy})_{i+1}, \ldots, (v_{xy})_{i+N-L-1}\right]^T \tag{3.53}$$

$$(\mathbf{v}_{yx})_i = \left[(v_{yx})_i, (v_{yx})_{i+1}, \ldots, (v_{yx})_{i+N-L-1}\right]^T \tag{3.54}$$

$$(\mathbf{v}_{yy})_i = \left[(v_{yy})_i, (v_{yy})_{i+1}, \ldots, (v_{yy})_{i+N-L-1}\right]^T \tag{3.55}$$

and L is the pencil parameter. Based on these vectors the MPM defines two matrices, $\mathbf{X}_1$ and $\mathbf{X}_2$, with dimension $4(N-L) \times (L+1)$ as

$$\mathbf{X}_1 = \begin{bmatrix} (\mathbf{v}_{xx})_{L-1} & (\mathbf{v}_{xx})_{L-2} & \cdots & (\mathbf{v}_{xx})_0 \\ (\mathbf{v}_{xy})_{L-1} & (\mathbf{v}_{xy})_{L-2} & \cdots & (\mathbf{v}_{xy})_0 \\ (\mathbf{v}_{yx})_{L-1} & (\mathbf{v}_{yx})_{L-2} & \cdots & (\mathbf{v}_{yx})_0 \\ (\mathbf{v}_{yy})_{L-1} & (\mathbf{v}_{yy})_{L-2} & \cdots & (\mathbf{v}_{yy})_0 \end{bmatrix} \tag{3.56}$$

$$\mathbf{X}_2 = \begin{bmatrix} (\mathbf{v}_{xx})_{L} & (\mathbf{v}_{xx})_{L-1} & \cdots & (\mathbf{v}_{xx})_1 \\ (\mathbf{v}_{xy})_{L} & (\mathbf{v}_{xy})_{L-1} & \cdots & (\mathbf{v}_{xy})_1 \\ (\mathbf{v}_{yx})_{L} & (\mathbf{v}_{yx})_{L-1} & \cdots & (\mathbf{v}_{yx})_1 \\ (\mathbf{v}_{yy})_{L} & (\mathbf{v}_{yy})_{L-1} & \cdots & (\mathbf{v}_{yy})_1 \end{bmatrix} \tag{3.57}$$

Again, Chiang [40] suggests a pencil length of $L = \frac{N}{3} > P$, based on first order perturbation analysis. Using Singular Value Decomposition (SVD) the pseudo-inverse $\mathbf{X}_1^+$ of the matrix $\mathbf{X}_1$ can be determined,

$$\mathbf{X}_1^+ = \mathbf{V}\mathbf{D}^{-1}\mathbf{U}^H \tag{3.58}$$

where the left and right matrix of singular vectors, U and V are defined by,

$$U = \begin{bmatrix} (\mathbf{u}_{xx})_1, (\mathbf{u}_{xx})_2, \ldots, \mathbf{u}_{(xx)L} \\ (\mathbf{u}_{xy})_1, (\mathbf{u}_{xy})_2, \ldots, \mathbf{u}_{(xy)L} \\ (\mathbf{u}_{yx})_1, (\mathbf{u}_{yx})_2, \ldots, \mathbf{u}_{(yx)L} \\ (\mathbf{u}_{yy})_1, (\mathbf{u}_{yy})_2, \ldots, \mathbf{u}_{(yy)L} \end{bmatrix}, V = \begin{bmatrix} (\mathbf{v}_{xx})_1, (\mathbf{v}_{xx})_2, \ldots, (\mathbf{v}_{xx})_L \\ (\mathbf{v}_{xy})_1, (\mathbf{v}_{xy})_2, \ldots, (\mathbf{v}_{xy})_L \\ (\mathbf{v}_{yx})_1, (\mathbf{v}_{yx})_2, \ldots, (\mathbf{v}_{yx})_L \\ (\mathbf{v}_{yy})_1, (\mathbf{v}_{yy})_2, \ldots, (\mathbf{v}_{yy})_L \end{bmatrix}$$

$D = diag\left[\boldsymbol{\sigma}_1, \boldsymbol{\sigma}_2, \ldots, \boldsymbol{\sigma}_M\right]$ and H denotes the conjugate transpose. For noisy data the singular values should be chosen to be the p^{th} largest values, and the resulting matrix $\mathbf{X}_1^+$ is called the truncated pseudo-inverse of the matrix $\mathbf{X}_1$. The complex model parameter $\mathbf{z}_p$ (Equation 3.36) can then be determined by calculating the eigenvectors of the matrix $\mathbf{Q}$, where

$$\mathbf{Q} = \mathbf{D}^{-1}\mathbf{U}^H\mathbf{X}_2\mathbf{V} \tag{3.59}$$

Substituting the poles z_p into Equation 3.34 and rewriting in matrix form, the parameter $\mathbf{b}$ can be determined by solving the matrix equations in a least squared sense

$$\mathbf{b} = \left(\mathbf{Z}^H\mathbf{Z}\right)^{-1}\mathbf{Z}^H\left[\left(\mathbf{v}_{xx}\right)_o\ \left(\mathbf{v}_{xy}\right)_o\ \left(\mathbf{v}_{yx}\right)_o\ \left(\mathbf{v}_{yy}\right)_o\right] \tag{3.60}$$

For the monostatic radar setup, the computational efficiency of the algorithm can be improved by noting that $v_{xy}[n] = v_{yx}[n]$. Hence only three data sets are required to solve for the parameters of the scattering matrix. Hence, since the size of the data matrices are reduced, the computational efficiency of the algorithm is improved. The reduced data matrices $\mathbf{X}_1$ and $\mathbf{X}_2$ are shown below

$$\mathbf{X}_1 = \begin{bmatrix} \left(\mathbf{v}_{xx}\right)_{L-1} & \left(\mathbf{v}_{xx}\right)_{L-2} & \cdots & \left(\mathbf{v}_{xx}\right)_0 \\ \left(\mathbf{v}_{xy}\right)_{L-1} & \left(\mathbf{v}_{xy}\right)_{L-2} & \cdots & \left(\mathbf{v}_{xy}\right)_0 \\ \left(\mathbf{v}_{yy}\right)_{L-1} & \left(\mathbf{v}_{yy}\right)_{L-2} & \cdots & \left(\mathbf{v}_{yy}\right)_0 \end{bmatrix} \tag{3.61}$$

$$\mathbf{X}_2 = \begin{bmatrix} \left(\mathbf{v}_{xx}\right)_{L} & \left(\mathbf{v}_{xx}\right)_{L-1} & \cdots & \left(\mathbf{v}_{xx}\right)_1 \\ \left(\mathbf{v}_{xy}\right)_{L} & \left(\mathbf{v}_{xy}\right)_{L-1} & \cdots & \left(\mathbf{v}_{xy}\right)_1 \\ \left(\mathbf{v}_{yy}\right)_{L} & \left(\mathbf{v}_{yy}\right)_{L-1} & \cdots & \left(\mathbf{v}_{yy}\right)_1 \end{bmatrix} \tag{3.62}$$

Both Steedly [39] and Wang [104] considered a similar problem to the one described above when estimating the parameters of the polarimetric TPR model. However, their algorithm has a fundamental flaw resulting from using the TPR as the input into their parameter estimation algorithm. The first step of the algorithm combines the captured polarimetric data (defined in the horizontal and vertical basis) as follows

$$\begin{bmatrix} s_{hl}(f) \\ s_{vl}(f) \end{bmatrix} = \frac{1}{\sqrt{2}} \begin{bmatrix} s_{hh}(f) & s_{hv}(f) \\ s_{vh}(f) & s_{vv}(f) \end{bmatrix} \begin{bmatrix} 1 \\ j \end{bmatrix} \tag{3.63}$$

where h, v, l are the horizontal, vertical and left circular polarization vectors and $s_{hl}(f)$ and $s_{vl}(f)$ are the frequency domain TPRs. Consider the case where the target is a left hand helix, with scattering matrix $\mathbf{s} = \frac{1}{2}\begin{bmatrix} 1 & j \\ j & -1 \end{bmatrix}$. Equation 3.63

can then be simplified as follows

$$\begin{bmatrix} s_{hl}(f) \\ s_{vl}(f) \end{bmatrix} = \frac{1}{2}\frac{1}{\sqrt{2}} \begin{bmatrix} 1 & j \\ j & -1 \end{bmatrix} \begin{bmatrix} 1 \\ j \end{bmatrix} = \frac{1}{2\sqrt{2}} \begin{bmatrix} 1+j\cdot j \\ j-j \end{bmatrix} = \begin{bmatrix} 0 \\ 0 \end{bmatrix} \tag{3.64}$$

and hence the algorithm would not be able to determine any of the required target parameters.

3.5.2 Determining the Huynen Target Parameters

Given the properties of the medium and assuming that the received data has been calibrated as shown in Equation 3.26, it is possible to determine the target parameters from $\mathbf{b}_{\{xy\}}$ and $\mathbf{z}$.

$$r_p = \frac{1}{\Delta r} \ln |z_p| \tag{3.65}$$

$$\lambda_p = \frac{1}{2\pi\Delta r} \angle z_p \tag{3.66}$$

$$A_{\{xy\}p} = \left|\mathbf{b}_{\{xy\}p}\right| \tag{3.67}$$

$$\theta_{\{xy\}p} = \angle \mathbf{b}_{\{xy\}p} \tag{3.68}$$

$$d_p = \frac{\beta_{m1}}{\alpha_{m1}^2+\beta_{m1}^2} r_p + \frac{\alpha_{m1}}{\alpha_{m1}^2+\beta_{m1}^2}\frac{\lambda_p}{2\pi} \tag{3.69}$$

$$\gamma_p = \frac{1}{\pi\beta_{m1}} \left(2\pi\alpha_{m1} d_p - \lambda_p\right) \tag{3.70}$$

$$\tau_{\{xy\}p} = \theta_{\{xy\}p} - 2\beta_{m2} d_p + 2\pi\beta_{m1} r_o d_p - \gamma_p \alpha_{m2} + \pi\gamma_p \alpha_{m1} r_o \tag{3.71}$$

$$\left|\mathbf{s}_{\{xy\}p}\right| = A_{\{xy\}p} d_p^2 \exp\left(2\alpha_{m2} d_p - 2\pi\alpha_{m1} r_o d_p\right) \exp\left(-\gamma_p\beta_{m2} + \pi\gamma_p\beta_{m1} r_o\right) \tag{3.72}$$

Letting

$$\xi_{(medium)p} = -2\beta_{m2} d_p + 2\pi\beta_{m1} r_o d_p - \gamma_p \alpha_{m2} + \pi\gamma_p \alpha_{m1} r_o \tag{3.73}$$

$$M_{(medium)p} = d_p^2 \exp\left(2\alpha_{m2} d_p - 2\pi\alpha_{m1} r_o d_p\right) \exp\left(-\gamma_p\beta_{m2} + \pi\gamma_p\beta_{m1} r_o\right) \tag{3.74}$$

where $\xi_{(medium)p}$ and $M_{(medium)p}$ are the phase and amplitude correction factors for the p^{th} target resulting from amplitude and phase dispersion in the medium. The scattering matrix for the p^{th} target can then be written as

$$\mathbf{s}_{\{xy\}p} = M_{(medium)p} e^{j\xi_{(medium)p}} \begin{bmatrix} \mathbf{b}_{xx_p} & \mathbf{b}_{xy_p} \\ \mathbf{b}_{yx_p} & \mathbf{b}_{yy_p} \end{bmatrix} \tag{3.75}$$

and the Graves power matrix for the p^{th} target is given by

$$\mathbf{G}_{\{xy\}p} = M^2_{(medium)p} \begin{bmatrix} \left|\mathbf{b}_{xx_p}\right|^2 & \left|\mathbf{b}_{xy_p}\right|^2 \\ \left|\mathbf{b}_{yx_p}\right|^2 & \left|\mathbf{b}_{yy_p}\right|^2 \end{bmatrix} \tag{3.76}$$

Applying the uniform transformation matrix $U\left(\rho_{opt}\left(\theta,\tau\right)\right)$ to Equation 3.76 transforms $\mathbf{G}_{\{xy\}_p}$ to the power form of the Huynen diagonal matrix (as described in Equation 3.19), such that

$$\begin{aligned} \mathbf{G}'_{\{xy\}p} &= M_p^2 \begin{bmatrix} 1 & 0 \\ 0 & \tan^4\gamma_p \end{bmatrix} \\ &= M^2_{(\text{medium})p} M^2_{(\text{target})p} \begin{bmatrix} 1 & 0 \\ 0 & \tan^4\gamma_p \end{bmatrix} \end{aligned} \tag{3.77}$$

Equation 3.77 shows that the parameter M_p, is dependent on estimates of the wavenumber in the medium, namely $(\alpha_{m1}, \alpha_{m2}, \beta_{m1}, \beta_{m2})$. Assuming knowledge of the medium, the true target backscatter can be determined. In Section 3.3.4 it was shown that the Huynen target parameters can be determined from Equation 3.76 by calculating the eigenvalues and eigenvectors of the measured power matrix (before it is adjusted for the medium loss and dispersion), by solving

$$\left(\mathbf{G}_p - \psi_p \mathbf{I}\right) \mathbf{E}_{opt_p} = 0 \tag{3.78}$$

where $\mathbf{E}^{1.2}_{opt_p}$ are the eigenvectors and $\psi_p^{1,2}$ are eigenvalues (where $\psi_p^1 > \psi_p^2$) of the matrix $\mathbf{G}_p$, such that

$$\mathbf{U}_p^* \left(\rho_{opt}\right) \mathbf{G}_p \mathbf{U} \left(\rho_{opt}\right) = \begin{bmatrix} \psi_p^1 & 0 \\ 0 & \psi_p^2 \end{bmatrix} \tag{3.79}$$

The parameters M_p and γ_p^h can then be determined by comparing Equation 3.77 and 3.79, such that

$$M_{\text{target}_p} = \frac{1}{M_{medium}} \cdot (\psi_1)^{\frac{1}{2}} \tag{3.80}$$

$$\gamma_p = \left(\arctan \left|\frac{\psi_2}{\psi_1}\right|\right)^{\frac{1}{4}} \tag{3.81}$$

The parameters θ_p, τ_p can then be calculated from $E^1_{opt_p}$ using Equations 3.3, 3.4 and 3.5. For the case of a monostatic and reciprocal radar configuration, the skip angle (v_p) and relative phase angle (ξ_p) can be determined from Equation 3.20 and 3.21.

In addition to the Huynen target parameters, the target position d_p and damping factor λ_p, can be used to increase the target information. Note again that λ_p and d_p are dependent on estimates of the properties of the medium, and hence must be adjusted to yield their true values.

Hence, it is possible to characterize a target by a set of parameters that can be factored into two feature vectors - those dependent on the properties of the medium, and those independent of the properties of the medium. By medium independent it is implied that these parameters can be estimated directly from $\overline{\mathbf{b}}_{\{xy\}_p}$, without knowledge of the parameters of the medium. This does not suggest that $\overline{\mathbf{b}}_{\{xy\}_p}$ is not affected by increase conductivity, since it is known that errors in z_p will cause errors in $\overline{\mathbf{b}}_{\{xy\}_p}$. The two feature vectors are listed below,

- Independent of the medium parameters – $\kappa_p^{'} = \left\{\gamma_p^h, \theta_p, \tau_p\right\}$
- Dependent on the medium parameters – $\kappa_p^{''} = \{d_p, \lambda_p, M_p, \xi_p, v_p\}$

3.5.3 Model Errors

Chapter 2 presented a discussion of the parameter estimation errors as a function of the medium conductivity for two targets. These discussions hold for the polarimetric case, since the parameter estimation is still based on minimizing model errors (LSE). In Section 3.6 graphs will be presented for the polarimetric model parameters and their corresponding errors, that reinforce this claim.

3.6 Simulations

This section presents results obtained by applying the polarimetric exponential algorithm to a single set of data comprising of multiple targets in medium with varying conductivity and permittivity. All data was generated using the polarimetric SFCW GPR model developed in Section 3.3. The radar parameters used are shown in Table 3.1.

Parameter	Value
f_L	600 MHz
N	140
Δf	4 MHz
$P_{\max}$	-30 dBm
N_s	$-\infty, -145$ dBm
Polarization	xx, xy, yx, yy

Table 3.1: Radar parameters for the fully polarimetric simulations

The simulation consists of three targets buried in a lossy medium, with a radar target geometry as shown in Figure 3.1. The targets include two linear wire targets at an angle of 40° and 80° to the $\hat{x}$ axis respectively. The angle of the wire targets can be estimated directly from the orientation angle of the optimum polarization, E_{opt}. The target parameters for the simulations are listed in Table 3.2.

Parameter	Value
d_p (m)	$1.6, 2.0, 2.1$
s_p (m)	$s_1 = \begin{bmatrix} 2j & 0.5 \\ 0.5 & -j \end{bmatrix}$ $s_2 = \begin{bmatrix} \cos^2(40°) & \frac{1}{2}\sin(80) \\ \frac{1}{2}\sin(80) & \sin^2(40) \end{bmatrix}$ $s_3 = \begin{bmatrix} \cos^2(80°) & \frac{1}{2}\sin(160) \\ \frac{1}{2}\sin(160) & \sin^2(80) \end{bmatrix}$
τ_p (deg)	$-45, 22.5, 0$
λ_p	$-0.1, -0.04, 0$

Table 3.2: List of targets and their parameters for the fully polarimetric simulations

3.6.1 Radar with no Thermal Noise ($ns = -\infty$ dBm)

This section presents the results for simulations with no thermal noise. This allows for the investigation of the parameter estimation errors resulting solely from the model errors. Since the model is exact for dielectric displacement current ($\sigma_m = 0$ mS/m), only the effects of conductivity on the model errors will be presented.

Figure 3.4 plots the target position (d_p) and the target damping factor (γ_p) and their corresponding errors as a function of conductivity. It can be seen that these errors are smaller than the position errors for the single polarization case presented in Chapter 2 (Figure 2.21). Figure 3.4 shows that the position error is less than 10 mm for $\sigma_m < 50$ mS/m, while the damping factor error is less than 1% for $\sigma_m < 30$ mS/m. The reason the damping factor error is larger is due to the fact that γ_p is relatively small, i.e. $\left|\gamma_p\right| << 1$.

Figure 3.5 plots the Huynen target parameters $M_p, \gamma_p^h, \theta_p$ and τ_p as a function of conductivity. It can be seen that the parameter M_p deviates from its correct value at a lower conductivity than the other parameters deviate from their correct values. Figure 3.6 plots the corresponding errors for the model parameters.

Figure 3.6 shows that the medium independent Huynen target parameters γ_p^h, θ_p and τ_p, have errors less than 0.02 rad for $\sigma_m < 50$ mS/m (for all scatterers), whereas the medium dependent parameter M_p has less than 100 mm error at $\sigma_m < 20$ mS/m (for all targets). These observations show that for this simulation, the medium independent parameters are more tolerant to model errors than the corresponding medium dependent parameters.

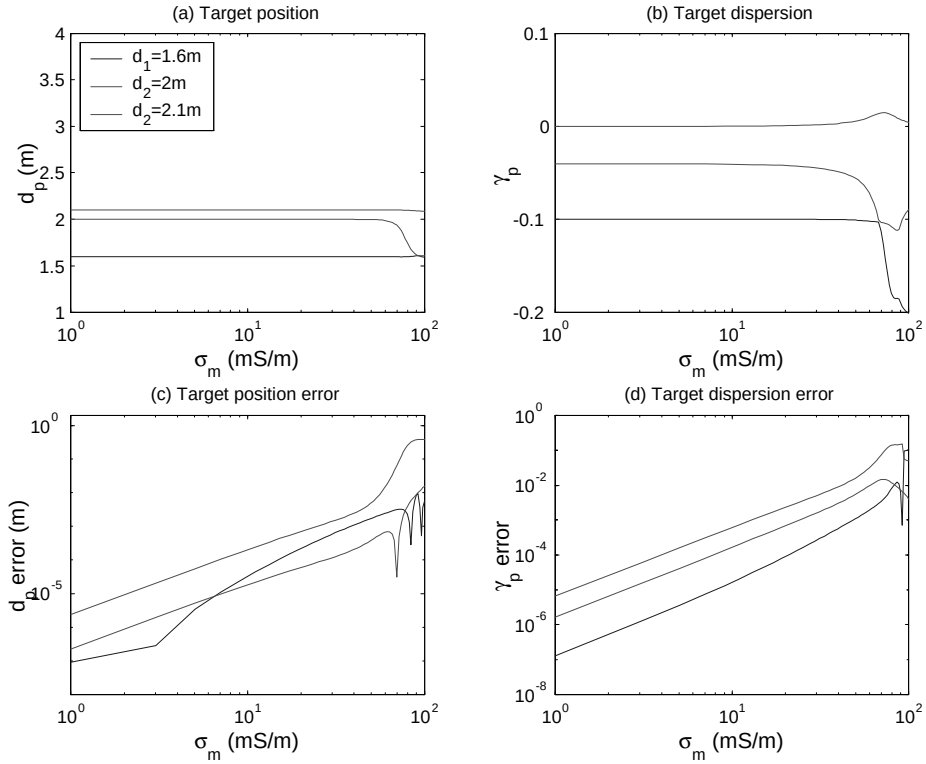

Figure 3.4: Plots of target position (d_p) and dispersion, (γ_p) and their errors as a function of conductivity (σ_m) for a radar noise floor of $-\infty$ dBm

3.6.2 Radar with Thermal Noise ($ns = -145$ dBm)

This section presents the results for simulations with thermal noise. This allows for the investigation of the parameter estimation errors resulting from both model error and noise. Two sets of results are presented. The first plots the estimated

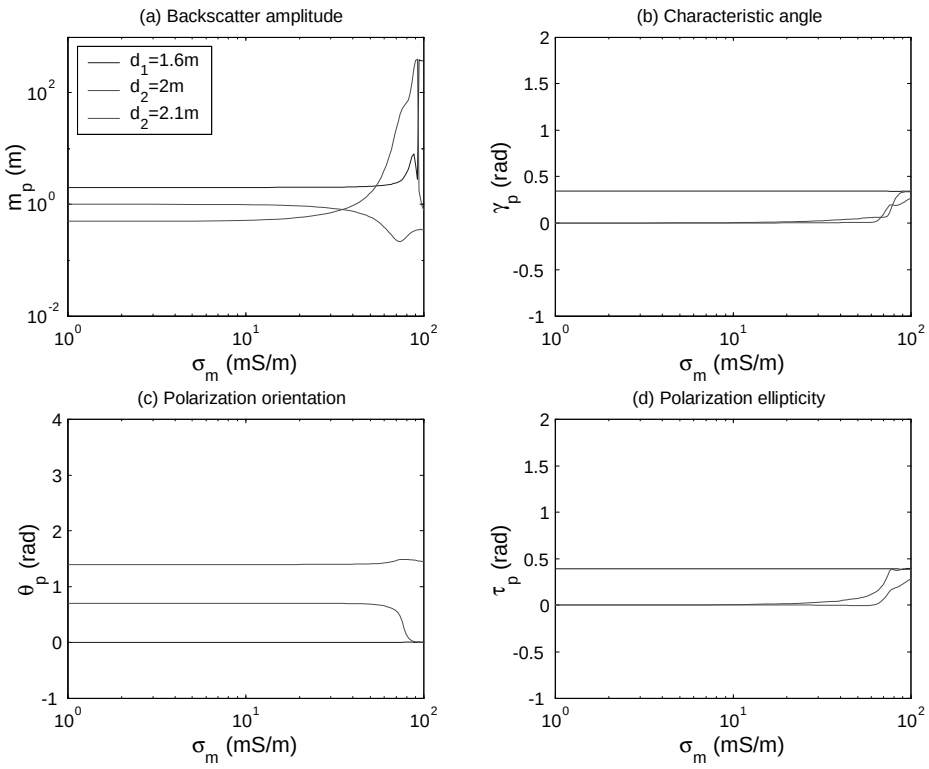

Figure 3.5: Plot of the Huynen target parameters $(M_p, \gamma_p^h, \theta_p, \tau_p)$ as a function of conductivity (σ_m) for a radar noise floor of $-\infty$ dBm

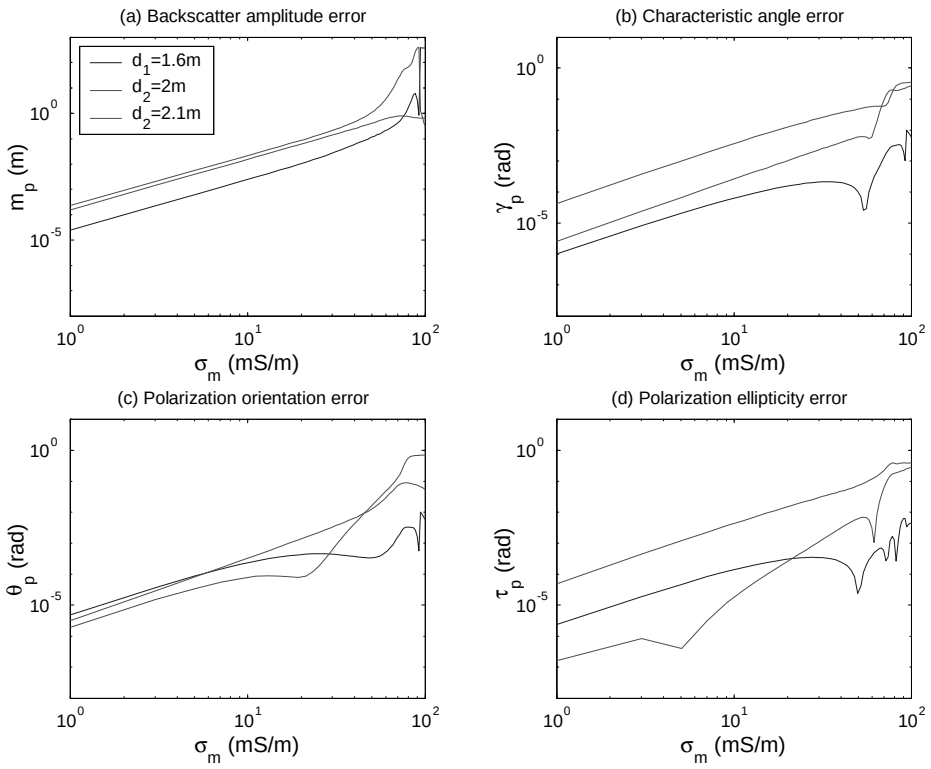

Figure 3.6: Plot of the Huynen target parameter errors (in $M_p, \gamma_p^h, \theta_p, \tau_p$) as a function of conductivity (σ_m) for a radar noise floor of $-\infty$ dBm

target parameters and their corresponding errors as a function of conductivity. The second plots the synthetic range profiles and the model positions and amplitude parameters, for various lossy media. The objective of the simulations is to compare the model based processing to the standard windowed IFFT technique, as well as to investigate the model parameter errors in the presence of thermal noise.

Model Parameters as a Function of Conductivity

Figure 3.4 plots the target position (d_p) and the target damping factor (γ_p) and their corresponding errors as a function of conductivity. The position errors increase rapidly for $\sigma_m > 40$ mS/m. This conductivity corresponds to a two way propagation loss of over 50 dB/m, resulting in a signal attenuation close to the radar noise floor. Figure 3.8 plots the Huynen target parameters $M_p, \gamma_p^h, \theta_p$ and τ_p as a function of conductivity. Figure 3.9 plots the corresponding errors for these parameters. The Huynen parameters γ_p^h, θ_p and τ_p have errors less than 0.01 rad for $\sigma_m < 30$ mS/m. Since the conductivity upper limit, for which the model parameters are valid, is lower than the noiseless case, the performance of the processing is limited by the thermal noise and not by the model errors.

Model Parameters and Synthetic Range Profiles as a Function of σ_m and ε_r''

The results of the simulation are shown in Figures 3.10 - 3.14. Each figure plots the radar impulse response and the target position and amplitudes for each element, $s_{\{xy\}}$, of the received scattering matrix. The radar impulse response is determined using the windowed (Hamming) IFFT method and is provided as a way of showing the advantages of using the parametric polarization algorithm. Results are presented for targets buried in a medium with increasing dielectric and ionic conductivity. This results in an increased signal loss and hence shows the performance of the algorithm for decreasing SNR.

The results show that the parameter estimation algorithm is able to detect all

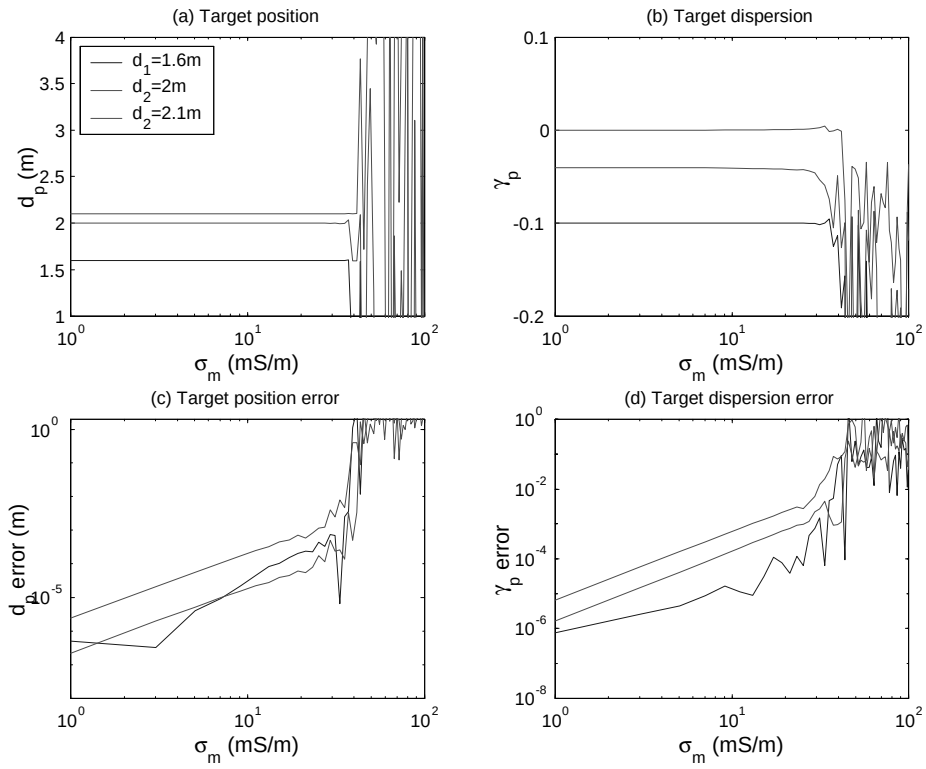

Figure 3.7: Plots of target position (d_p) and dispersion (γ_p) and their errors as a function of conductivity (σ_m) for a radar noise floor of -145 dBm

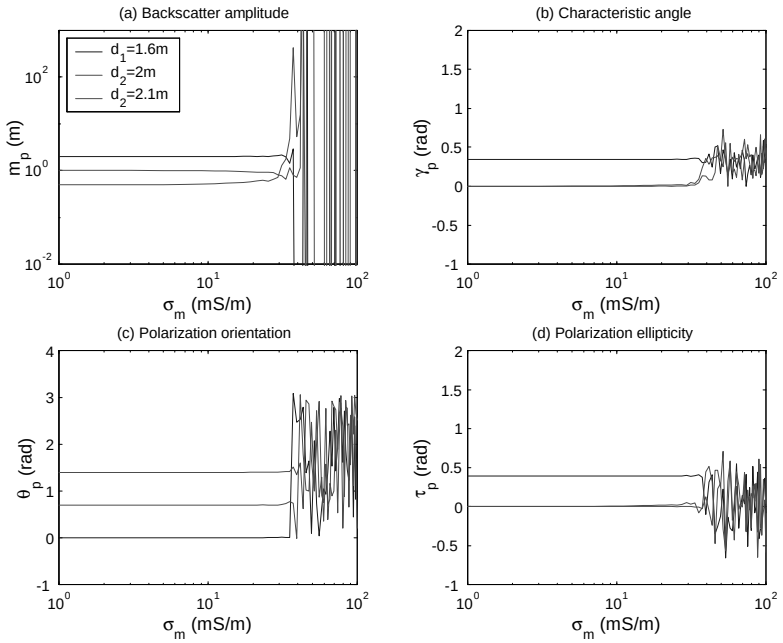

Figure 3.8: Plot of the Huynen target parameters $(M_p, \gamma_p^h, \theta_p, \tau_p)$ as a function of conductivity (σ_m) for a radar noise floor of -145 dBm

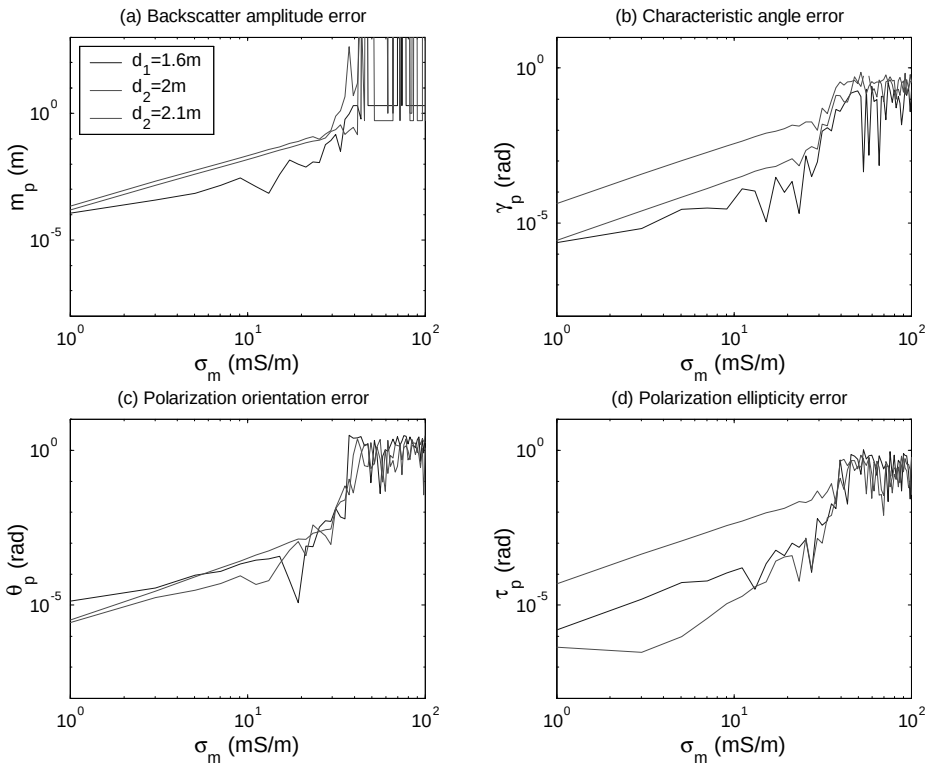

Figure 3.9: Plot of the Huynen target parameter errors (in $M_p, \gamma_p^h, \theta_p, \tau_p$) as a function of conductivity (σ_m) for a radar noise floor of -145 dBm

targets for all simulations. The algorithm is also able to resolve the targets which are not visible in the radar impulse response. It is also interesting to note that for $\sigma_m = 25$ mS/m and $\varepsilon_r = 6 - 0.3j$ all the targets are detected, even when they are barely visible in the impulse response.

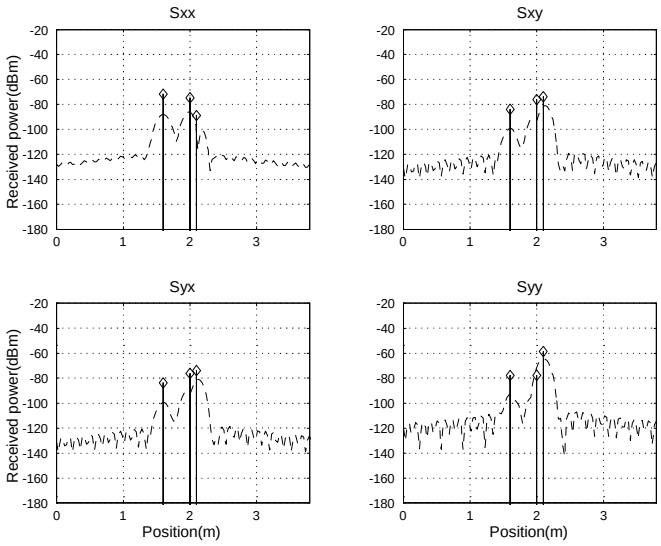

Figure 3.10: Plot of received power as a function of position for $s_{xx}, s_{xy}, s_{yx}, s_{yy}$ for $\sigma = 10$ mS/m and $\varepsilon_r = 6$

3.7 Measurements

This section shows the results of applying the theory developed in this chapter to measured radar data. Due to limited funding and equipment resources, it was not possible to construct a measurement setup that would allow one to accurately determine the exact scattering matrices for the various buried targets, or measure the properties of the medium. However, it was still felt that testing the algorithm on various physical targets with real measurement equipment was necessary, to observe the performance of the algorithm for real data.

Figures 3.15 and Figure 3.16 show a block diagram and photograph of the radar measurement setup respectively.

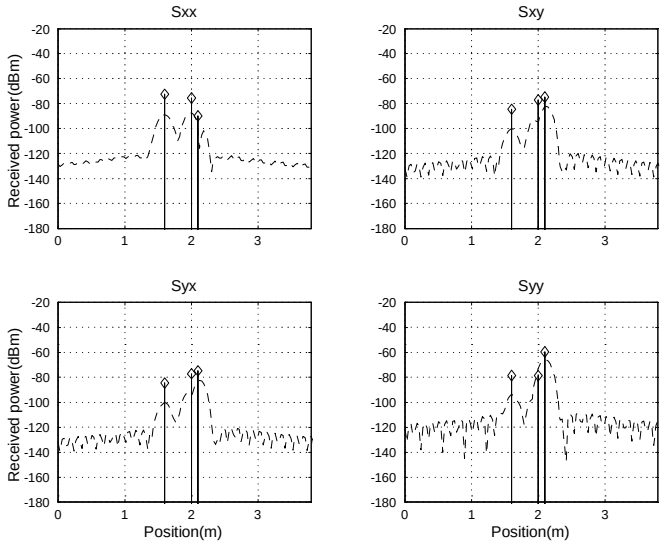

Figure 3.11: Plot of received power as a function of position for $s_{xx}, s_{xy}, s_{yx}, s_{yy}$ for $\sigma = 10$ mS/m and $\varepsilon_r = 6 - 0.1j$

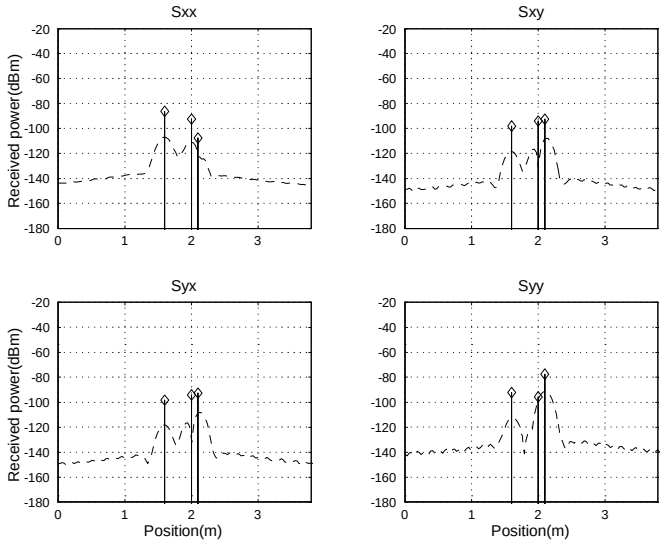

Figure 3.12: Plot of received power as a function of position for $s_{xx}, s_{xy}, s_{yx}, s_{yy}$ for $\sigma = 10$ mS/m and $\varepsilon_r = 6 - 0.2j$

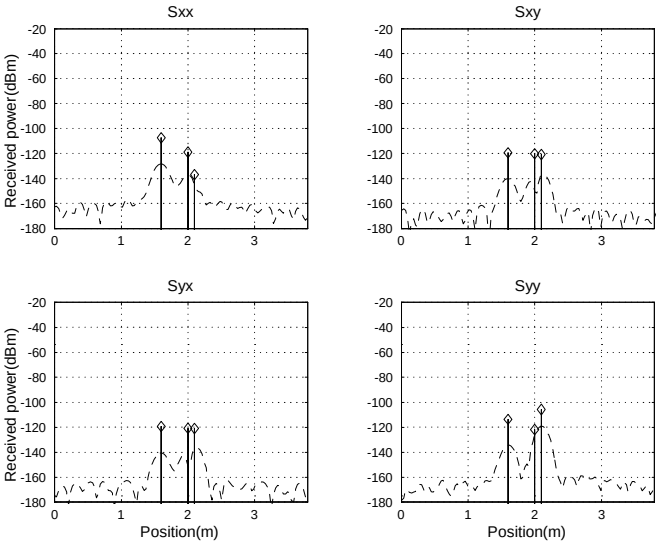

Figure 3.13: Plot of received power as a function of position for $s_{xx}, s_{xy}, s_{yx}, s_{yy}$ for $\sigma = 20$ mS/m and $\varepsilon_r = 6 - 0.2j$

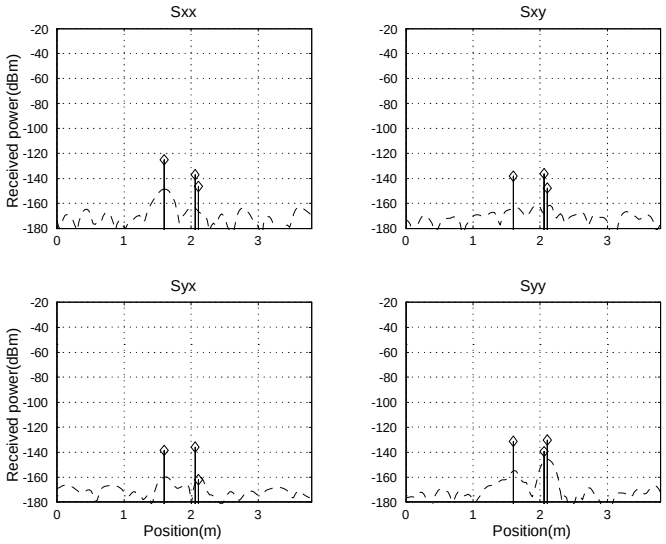

Figure 3.14: Plot of received power as a function of position for $s_{xx}, s_{xy}, s_{yx}, s_{yy}$ for $\sigma = 25$ mS/m and $\varepsilon_r = 6 - 0.3j$

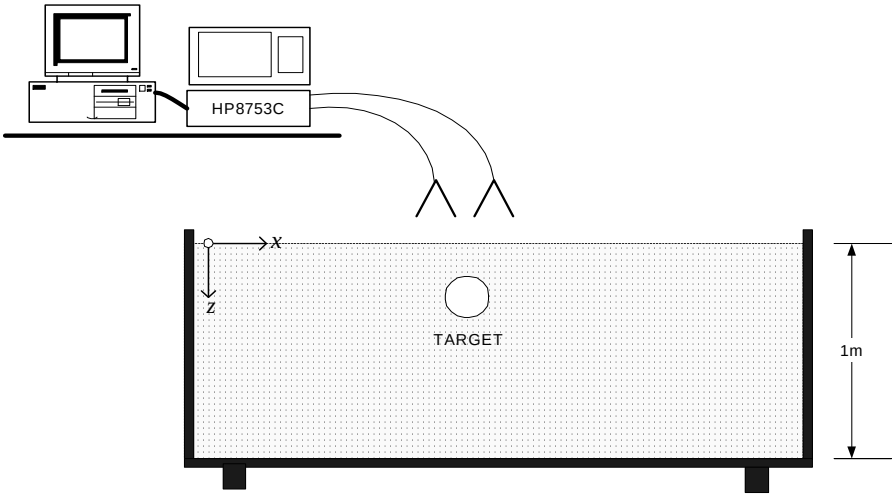

Figure 3.15: Block diagram of the polarimetric measurements setup.

Figure 3.16: Photograph of the antenna setup for the polarimetric measurements.

The measurement equipment includes: a laboratory vector network analyzer (HP8753C), a computer, two ridged horn antennas with a bandwidth from $2 - 18$ GHz and a 50° E and H plane beamwidth, and various test targets. Computer software was written to control and capture data from the HP8753C network analyzer. All data processing was performed on a personal computer with software written in Matlab^{TM}. The radar was operated over a bandwidth from $3 - 6$ GHz with a frequency step size of 20 MHz. This results in a free space resolution of approximately 4.8 mm. The antennas were mounted at a height of 5 cm above the ground surface.

Due to the limited equipment resources, it was not possible to measure all the required calibration functions (Equations 3.24 and 3.26), except for the radar electronics frequency response ($G_s(f)$). The sandpit was filled with dry sea sand with an estimated permittivity of $\varepsilon_r = 4$. The radar developed in Chapter 4 could not be used to capture the data presented in this section, due to the requirement for high frequency measurement equipment resulting from the limited size of the measurement setup.

All data was processed using the algorithm presented in this chapter. The processed data is displayed as a set of figures, showing the radar impulse response and the target position and amplitude parameters for each element $s_{\{xy\}}$ of the received scattering matrix. The radar impulse response is determined using the windowed (Hamming) IFFT method and is provided as a way of showing the advantages of using the parametric polarization algorithm. Only the medium independent target parameters as well as the target position are presented, due to the limited calibration data.

3.7.1 Results

This section shows the results of a number of different targets buried a few centimeters below the surface of the sandpit. The targets include: the ground surface, a metal disk, a metal plate, a polystyrene cylinder, a metal rod at different angles to the antenna horizontal polarization, a metal sphere and sixteen

metal screws. The different targets were chosen to provide different feature vectors to demonstrate and show the promise of the theory developed in this Chapter. The different targets were chosen to provide different feature vectors to demonstrate and show the promise of the theory developed in this section. For each measurement, the first reflection is always the antenna-to-antenna coupling, followed by the air-ground interface and the actual target. All measurements are referenced relative to the position of the antenna-to-antenna reflection. Since no measured data exists for the properties of the material, only those Huynen parameters that are independent of the properties of the medium are presented. The position of the target is presented as a point of reference.

Ground Surface

Figure 3.18 shows the processed results for the ground/surface measurements. The figure shows that two primary targets are visible in all polarization channels. These can be seen both in the radar impulse response and the estimated target position and amplitude parameters. The Huynen medium independent target parameters for the ground surface reflection are listed in Table 3.3.

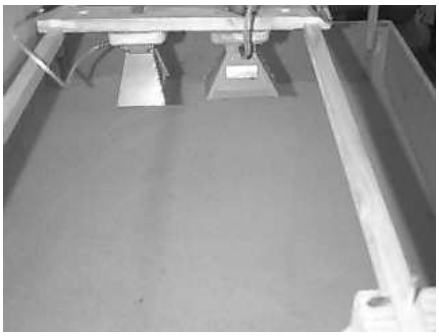

Figure 3.17: Photograph of antenna location above the ground surface

Table 3.4 lists the ground response parameters, extracted from the different target measurements. For all measurements the parameters are within a few degrees of each other, except for the metal screw results. For this measurement the target was much closer to the surface than for the other measurements, possibly

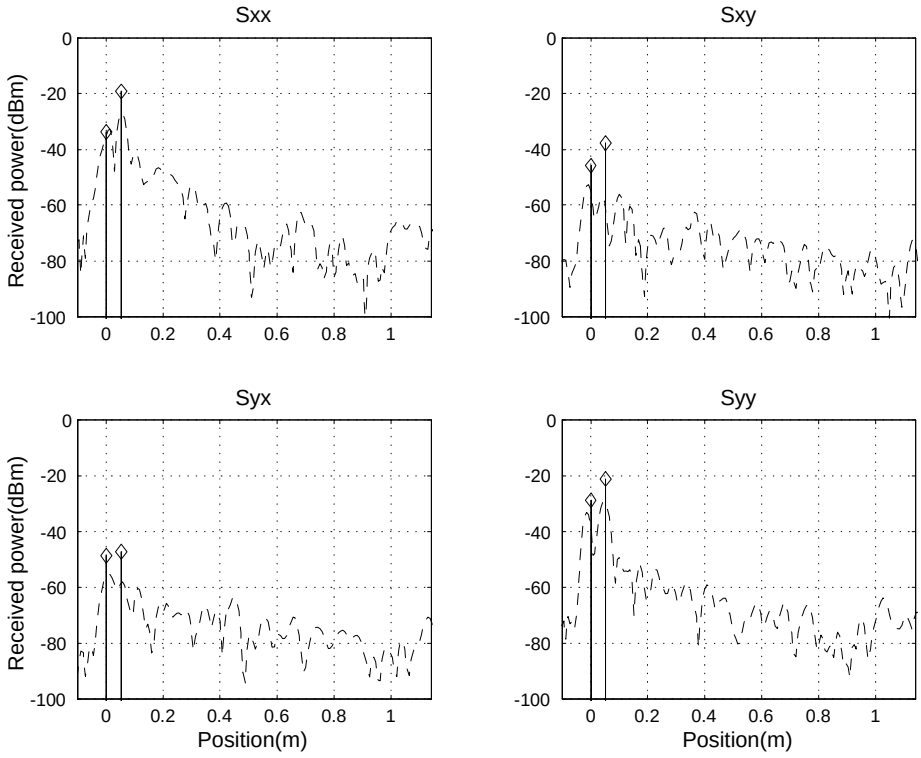

Figure 3.18: Plot of received power as a function of position for $s_{xx}, s_{xy}, s_{yx}, s_{yy}$ for ground surface measurement

d_p (m)	γ_p^h (°)	θ_p (°)	τ_p (°)
0.05	38.36	167.66	5.65

Table 3.3: Huynen medium independent target parameters for the ground surface

resulting in the observed errors.

Measurement	d_p (m)	γ_p^h (°)	θ_p (°)	τ_p (°)
Metal Disk	0.05	38.36	167.66	5.65
Polystyrene Cylinder	0.05	31.31	175.87	1.32
Metal Rod (0°)	0.05	31.6	173.30	0.23
Metal Rod (45°)	0.05	34.76	161.11	-1.83
Metal Rod (90°)	0.05	31.89	173.53	2.51
Metal Screws	0.05	36.72	141.84	-0.52
Metal Sphere	0.05	36.77	171.68	2.34

Table 3.4: Table of ground response parameters extracted from the various target profiles

Metal Disk

A small metal cylinder, 30 cm in diameter and 10 cm thick, was buried approximately 5 cm below the surface. Figure 3.20 shows that the target response consists of two reflections. These correspond to the surface/ground interface and the edges of the target. The estimated target parameters show that the optimum polarization for each target scattering centre has more than 50^o difference between the angles. The Huynen medium independent target parameters for both reflections are listed in Table 3.5.

Figure 3.19: Metal cylinder

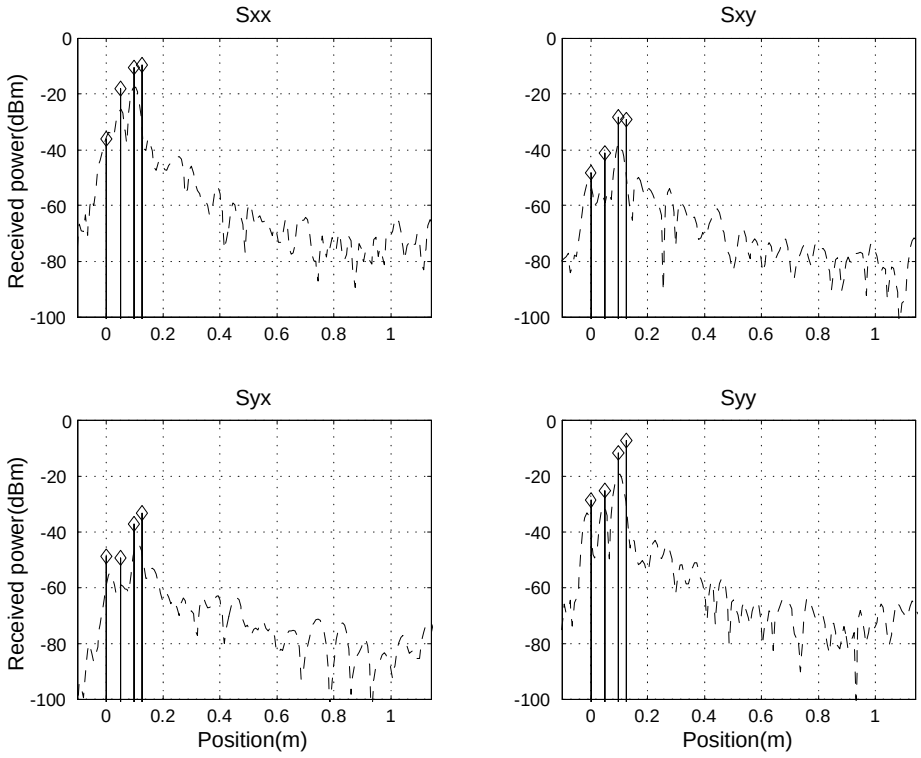

Figure 3.20: Plot of received power as a function of position for $s_{xx}, s_{xy}, s_{yx}, s_{yy}$ for a metal cylinder

d_p (m)	γ_p^h (°)	θ_p (°)	τ_p (°)
0.10	40.18	24.29	7.77
0.12	36.17	92.54	-8.86

Table 3.5: Huynen medium independent target parameters for the metal disk

Polystyrene Cylinder

A small polystyrene cylinder, 10 cm diameter and 5 cm thick, was buried 5 cm below the ground surface. Figure 3.22 shows that the single reflection from the target is detected at a distance of 5 cm below the surface. The Huynen medium independent target parameters are listed in Table 3.6.

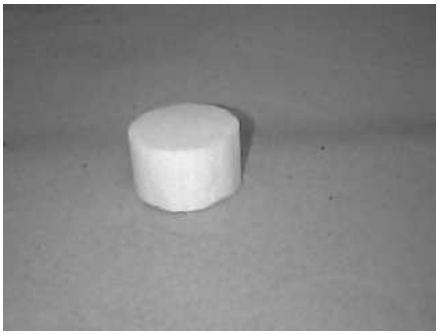

Figure 3.21: Polystyrene cylinder

$d_p\,(m)$	$\gamma_p^h\,(^\circ)$	$\theta_p\,(^\circ)$	$\tau_p\,(^\circ)$
0.1	33.20	168.9	26.49

Table 3.6: Huynen medium independent target parameters for the polystyrene cylinder

Metal Rod

A thin metal rod, 2 cm diameter and a length of 1 m, was buried approximately 7 cm below the ground surface. The target was oriented at $0^\circ, 45^\circ$ and 90° to the horizontal polarization axis. Figures 3.24, 3.25 and 3.26 show a target detected at approximately $7-8$ cm below the surface. The Huynen medium independent target parameters for the three pipe orientations are listed in Table 3.7. The extracted target parameters do not resemble the theoretical predictions (see Section 3.6), resulting from the absence of calibration to remove the effects of the antenna response and polarization coupling. However, the results do show that the parameters vary as the rod rotates.

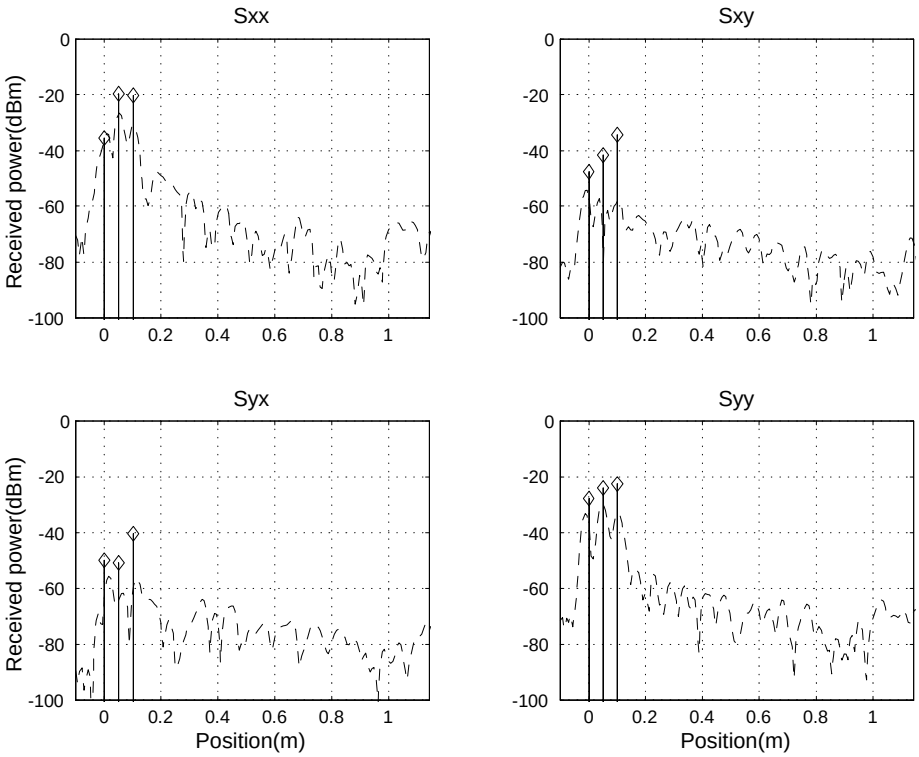

Figure 3.22: Plot of received power as a function of position for $s_{xx}, s_{xy}, s_{yx}, s_{yy}$ for a polystyrene cylinder

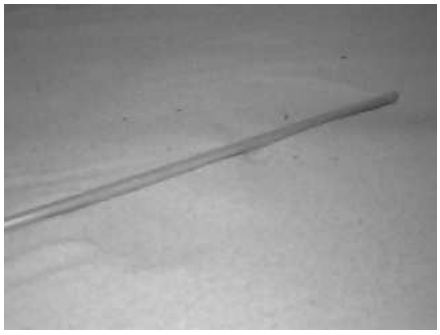

Figure 3.23: Metal rod

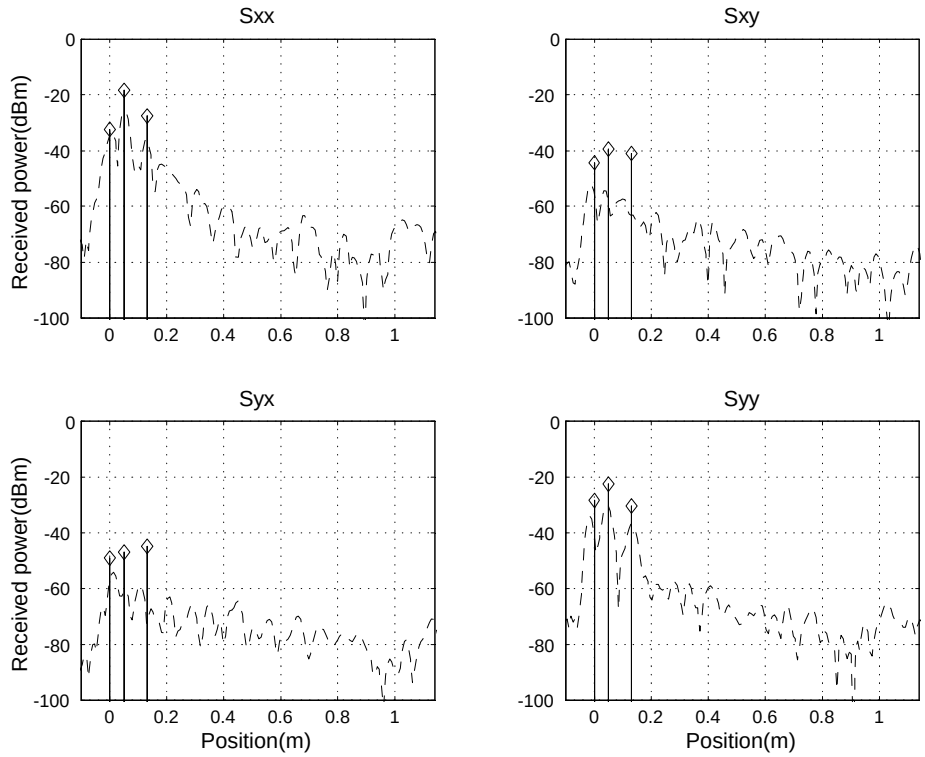

Figure 3.24: Plot of received power as a function of position for $s_{xx}, s_{xy}, s_{yx}, s_{yy}$ for a metal rod parallel to the horizontal polarization axis

Angle of rod(°)	d_p (m)	γ_p^h (°)	θ_p (°)	τ_p (°)
0	0.13	32.08	25.33	-1.96
45	0.12	21.95	7.51	39.30
90	0.11	34.71	83.25	-31.85

Table 3.7: Huynen medium independent target parameters for the metal rod

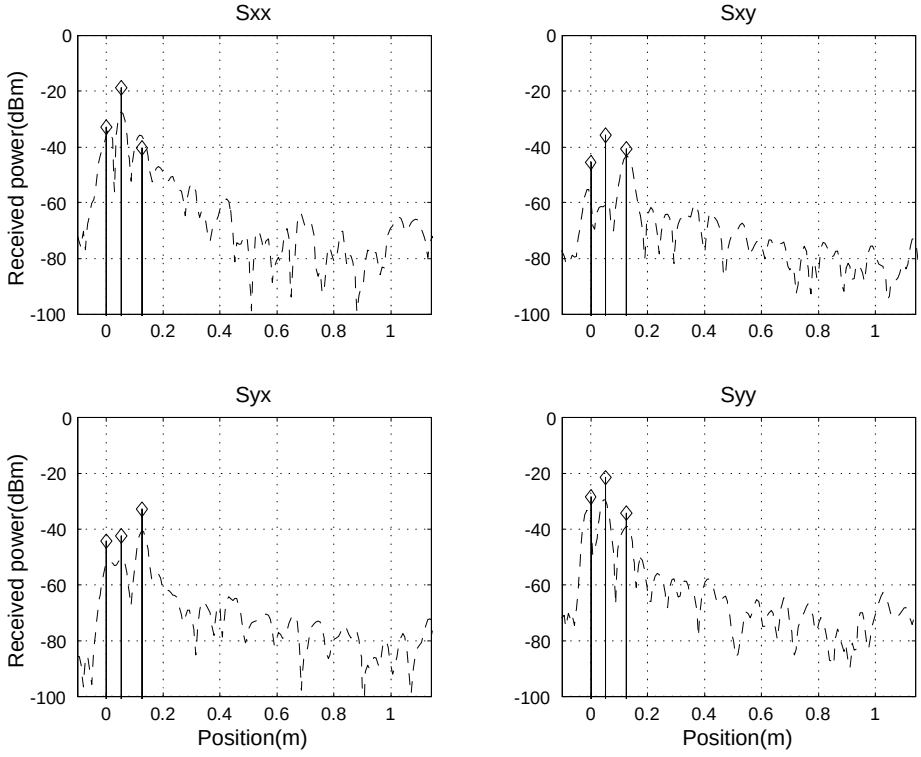

Figure 3.25: Plot of received power as a function of position for $s_{xx}, s_{xy}, s_{yx}, s_{yy}$ for a metal rod at 45° to the horizontal polarization axis

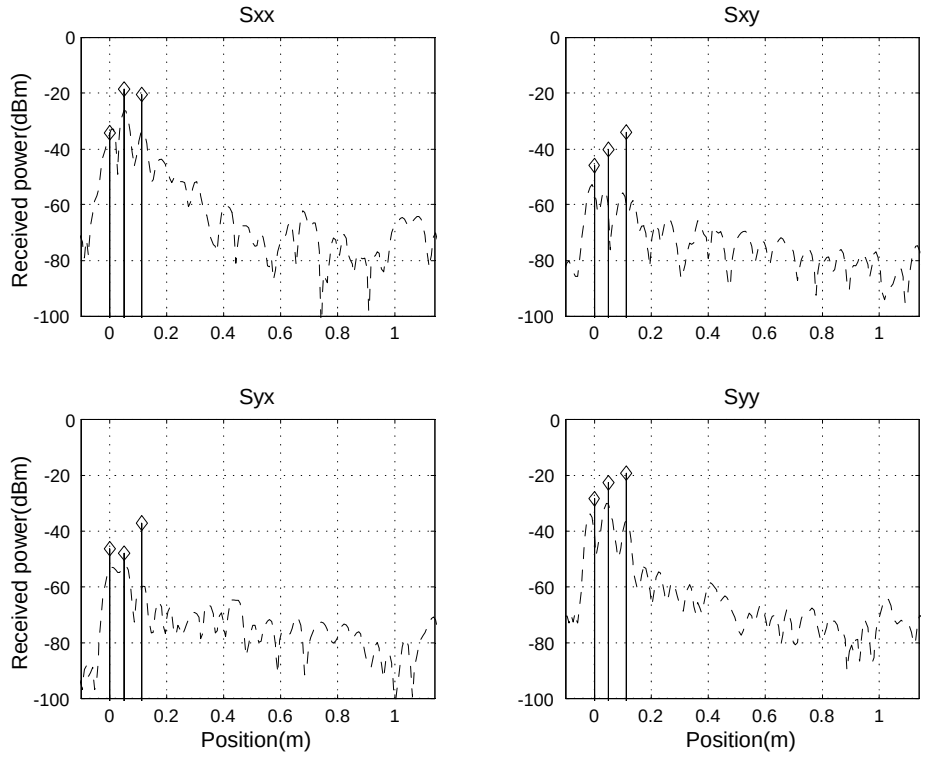

Figure 3.26: Plot of received power as a function of position for $s_{xx}, s_{xy}, s_{yx}, s_{yy}$ for a metal rod at 90° to the horizontal polarization axis

Metal Screws

A number of small metal screws, each around 7 cm in length were buried a few centimeters below the ground surface. It might seem strange to use screws as targets, however in the context of landmine detection they are useful as a simulant for bullet shells buried just below the ground surface. Figure 3.28 shows that there is a reflection 3 cm below the ground surface that corresponds to the position of the metal screws. The Huynen medium independent target parameter are listed in Table 3.8.

Figure 3.27: Sixteen metal screws

d_p (m)	γ_p^h (°)	θ_p (°)	τ_p (°)
0.08	32.11	103.31	-26.90

Table 3.8: Huynen medium independent target parameters for the metal screws

Metal Sphere

A metal sphere with a diameter of 12 cm was buried with its top edge, 5 cm below the ground surface. The processed target data is presented in Figure 3.30, and clearly shows a target reflection at 5 cm below the surface. The Huynen medium independent target parameters are listed in Table 3.9. Again, the target parameters differ from the expected parameters for a sphere, i.e. $\gamma^h = 45^o$ and with circular polarization as the optimum polarization.

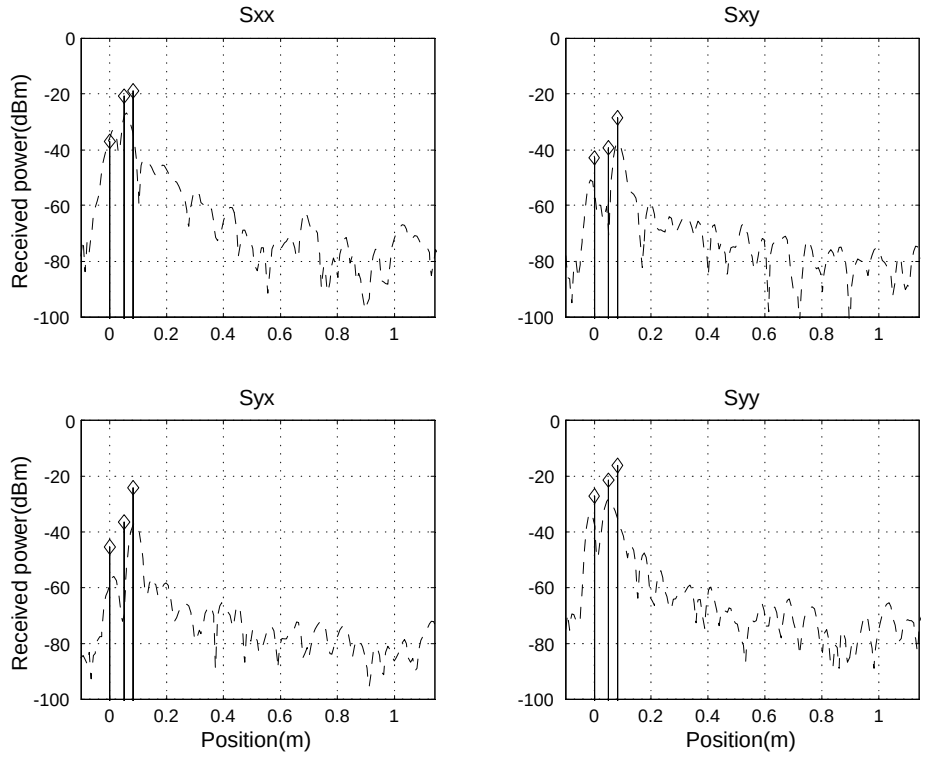

Figure 3.28: Plot of received power as a function of position for $s_{xx}, s_{xy}, s_{yx}, s_{yy}$ for sixteen metal screws

Figure 3.29: Metal sphere

d_p (m)	γ_p^h (°)	θ_p (°)	τ_p (°)
0.10	33.20	168.95	-26.49

Table 3.9: Huynen medium independent target parameters the metal sphere

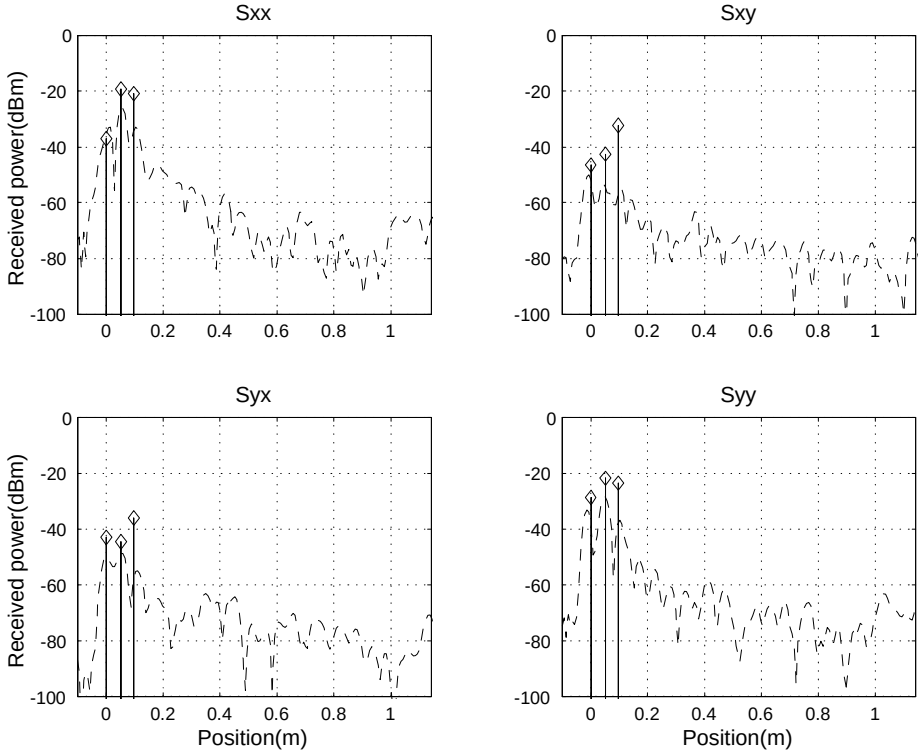

Figure 3.30: Plot of received power as a function of position for $s_{xx}, s_{xy}, s_{yx}, s_{yy}$ for the metal sphere

Discussion

The results show that the measured target parameters are different for the various objects buried in the sandpit, while the ground response parameters were within a few degrees of each other for the different radar measurements. The measured target parameters do vary from their theoretically values. These variations are due to the limited calibration of the measured data. Even though the data set is small, and calibration is absent, the limited results do indicate that the processing presented in this chapter shows much promise.

3.8 Conclusions

This chapter extends the model developed in Chapter 2 to a fully polarimetric radar model for a stepped frequency continuous wave radar. Based on certain assumptions relating to the target damping factor, the model is shown to be equivalent to the multi-snapshot exponential model found in signal processing theory. The Multi-snapshot MPM algorithm is used to extract the parameters from the exponential model. These parameters are related to the polarimetric SFCW GPR model parameters, providing valuable insight and understanding into how these parameters relate to the properties of a lossy medium. Using a technique proposed by Kostinski [101] the Huynen target parameters are extracted from the estimated scattering matrices. It is shown that these parameters can be separated into medium dependent and independent feature vectors.

Simulations are presented to investigate the performance of this technique for changing conductivity and hence model error. The performance of the algorithm is similar to that of the single polarization case. It is shown that the medium independent parameters are more tolerant to model errors than the corresponding medium dependent parameters, for the simulated results.

The simulations also show that the parameter estimation technique is able to resolve targets which were not visible in the radar impulse response.

The algorithm is applied to real measured data, captured with laboratory measurement equipment. Given the constraints of limited calibration (no polarimetric antenna calibration data was available to allow its removal from the raw measured data) and medium information (no material measurements were available to allow its effects to be removed from the signal processing model parameters to determine the actual GPR model parameters), the algorithm performed well for detecting the target positions for the two sets of field measurements.

Chapter 4

Implementation of a SFCW Radar

4.1 Introduction

The performance of any ground penetrating radar depends on the hardware implementation. Numerous SFCW radars have been implemented both commercially and for academic study. However, not much focus has been placed on the details of the design [107, 35, 37, 36, 3, 31].

SFCW modulation has been used for a number of years in antenna measurement facilities [15, 31]. These systems are typically implemented using a network analyzer controlled via a computer. The initial SFCW GPR systems were based on the same architecture [17]. Iizuka [32] and later Uratsuka [107] used two synthesizers in combination with commercial microwave building blocks to implement a SFCW GPR. However, most of the initial systems [17, 32, 107, 36] were costly, large, bulky and required large amounts of power. Even many of the more recent SFCW radar implementations such that the systems from the University of Queensland [21], the University of Delft [23] and C.O.R.I.S.T.A [22] are large and bulky. This limits the ease of deployment of the equipment for field measurement. For this reason the SFCW GPR did not progress further

than academic interest.

Over the last decade the cost of RF technologies (fast switching synthesizers, voltage controlled oscillators and other RF building blocks) has decreased considerably, making it more feasible to develop SFCW GPR technology. In addition the availability of fast, low cost and low power digital signal processors has contributed to the growing interest in this technique. The US Department of Energy [19, 20] and Coleman Research Corporation (CRC) [42] have both developed portable Stepped-FMCW and Stepped-FCW radars for landmine detection under Department of Defence (DOD) grants. Brashforth [18] took the technology and started his own company called Georadar which develops the only commercially available stepped FMCW radar system along with Satimo [5]. Noon *et al.* from the University of Queensland are also planning to release their SFCW radar technology through their company called GoundProbe [108]. There are many others who have investigated and developed SFCW hardware, including OSU [31], Conoco, Norwegian Geotechnical Institute [36], Norwegian University of Science and Technology [109], Ensco/Xadar [3] to name a few [4, 3], however most these systems are either university based, network analyser based systems, large laboratory systems or no longer available.

The University of Cape Town has been active in the area of designing and implementing SFCW GPRs since 1988 [110, 111]. Research included a review of radar architectures and the design of a radar [112, 113, 114], the design and testing of a feedthough cancellation system to improve the dynamic range of a SFCW radar [115] and the development of a low cost SFCW GPR prototype [43]. Two radar prototypes have been developed. The first system, called MercuryA, is a 1000 MHz to 2000 MHz SFCW GPR [116] developed by the author for a local company interested in landmine detection research [45]. The second system, called MercuryB, is a 200 MHz to 1600 MHz system developed with the help of masters students from the University [46, 47] as a prototype for Ball Aerospace for research into a forward looking radar for directional drilling.

In this chapter the design and development of a low cost stepped frequency continuous wave radar is presented. It addresses both the philosophy as well

as the technology that was used to develop the system. It is important to note that the intention of this chapter is not to present a detailed theoretical analysis of the radar design. This is beyond the scope of the thesis and is the topic of current research at the university. Due to the limitations in resources it was also not possible to develop the complete polarimetric radar system.

The chapter begins by providing motivation for using SFCW modulation. Next the choice of various SFCW GPR architectures is presented. This is followed by an overview of the design of the SFCW GPR, highlighting the key and novel aspects of the design. A brief description of the implementation of a 200 MHz to 1600 MHz system is also provided. Finally results are presented for a number of field measurements.

4.2 Contributions

In this chapter the following novel contributions were made

- The implementation of a SFCW GPR using off-the-shelf low cost mobile communications technology.

- The design of a simple heterodyne radar architecture using a single IQ demodulation channel, with all frequency generation and demodulation elements relative to a single reference clock.

- The choice of the synthesizer and IF bandwidth parameters to improve the IF phase noise relative to the transmit and local oscillator phase noise and to ensure coherency with respect to the reference oscillator.

- The design of a simple IQ demodulation and sampling algorithm which allows for the use of low cost high dynamic range analog-to-digital convertors.

4.3 Scope

The development of the technology in this chapter was primarily motivated by the lack of resources at the university, and funding to purchase commercially manufactured equipment, as well as the requirements for a small, compact and low power system that can easily be deployed field measurements. This chapter simply provides various insights gained by the author, in developing such a radar system. It is not the objective of this chapter to provide detailed design and analysis of the radar system - as this was not the major thrust of the thesis. However it is felt that this work represents a substantial contribution to the development of SFCW GPR hardware and that it is useful to include these results in this document. For a more detailed system design the reader is referred to a master's thesis supervised by the author [46].

4.4 Modulation Techniques

The GPR field has seen the development of a number of radar systems, designed using various modulation techniques. These include video pulse [15], frequency modulated CW [19], synthesized pulse (or SFCW) [3], and noise radars [25]. SFCW systems, in principle, measure the same electromagnetic parameters as conventional *carrier free* pulsed systems. It is felt, however, that the SFCW technique allows for careful control of emitted radiation, so important for compliance with modern EMC regulations, as well as for avoiding mutual interference when an array of radars are required to operate together. This modulation technique also has the ability to receive passively (with the transmitter off) RF noise in urban environments and then transmit in the noise gaps in the spectrum [**?**] with better SNR than impulse radars. In addition, SFCW provides the following advantages over other modulation techniques - high mean transmit power, large sensitivity, wide dynamic range and greater spectral control. This control allows for simple calibration to remove all systematic errors due to component distortion and antenna gain. SFCW radar design is not a new technology - a number of systems have been developed and their basic architecture and results

discussed in the literature [2, 31, 15, 3, 42, 20]. It is felt that there is large scope for improving the design and implementation of such radars.

One of the major disadvantages of SFCW radar is that its dynamic range is limited by strong radar returns e.g. antenna coupling. Pulsed systems allow one to apply a time varying gain or gating, with the aim of attenuating the strong early radar returns. This same principle can solve the coupling problem in SFCW GPRs. Pulse SFCW modulated radars combine the advantages of pulse and SFCW systems. Currently, the University of Queensland [21], Hamran from Norway [37] and OSU [31] have implemented pulsed SFCW radar systems and shown some very positive results [21]. An alternative approach to reducing the antenna coupling is to use frequency domain active cancellation system as proposed by Freundorfer [79] and later modified by Kabutz and Langman [115] to allow for the removal of any large coupling signal.

This chapter focuses more on the development of the fundamental architecture and performance of a standard SFCW system. It is fairly trivial to extend this to a pulse SFCW system [37, 21] or incorporate the active cancellation.

4.5 Possible Radar Architectures

Several different architectures exist to implement a SFCW radar. The fundamental requirement of all these architectures is that they all need to facilitate the design of a wideband high dynamic range radar. The most common architectures are based on the homodyne [3, 19] and heterodyne [107, 32] receivers. For a detailed look at other possible architectures (including a super-heterodyne system) the reader is referred to a masters dissertation by Kabutz [117]. In this section the homodyne system is briefly presented, followed by a more detailed discussion on the dual heterodyne architecture used to implement this radar system.

4.5.1 Homodyne Architecture

The homodyne radar is a system that synchronously detects radar returns, by mixing the receive signal with a portion of the transmit signal and thus mixing the required information down to DC, as is shown in Figure 4.1.

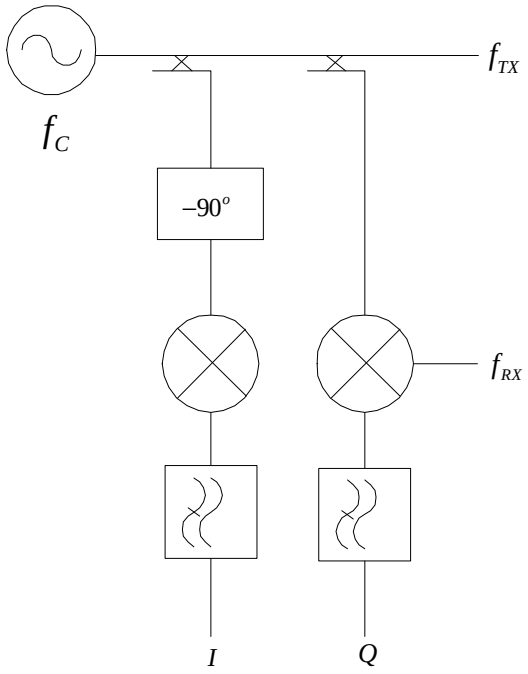

Figure 4.1: Block diagram of a homodyne architecture

The homodyne architecture has fundamental limitations, which limit its use in the development of low cost and high performance SFCW GPRs. These limitations include

- The filtering of the RF harmonics across a wide transmit bandwidth.
- The demodulation of the received signals to extract amplitude and phase information.

These will be discussed in more detail in the rest of this section.

RF Harmonics

The radar transmit frequency contains harmonics, $f_{\mathrm{TX}} = nf_{\mathrm{C}}$, where $n = 1, 2, ..., N$, and f_{C} is the oscillator fundamental frequency. These harmonics are mixed down to baseband resulting in the detection of multiple targets. Consider a target at a distance d metres from the radar. Transforming the raw stepped frequency data to the spatial domain (impulse response) results in multiple targets at positions given by nd mod $d_{\max}$, where $d_{\max}$ is the unambiguous range of the SFCW radar. The only way to remove this problem is to filter the radar oscillator output such that its largest harmonics are smaller than the required radar dynamic range (which can exceed 90 dB). For wideband systems, this requires expensive switched filter banks.

IQ Demodulation

Another problem with the homodyne architecture is the extraction of amplitude and phase information from the received signal. This typically involves mixing the received signal with an inphase (I) and quadrature (Q) portion of the radar oscillator (f_{C}) - as is shown in Figure 4.1. The system is prone to gain and phase imbalances resulting from the signal passing through two different IQ demodulation channels. This results in errors in the measured I and Q data. Complex calibration is required to remove IQ imbalance and gain variations in the demodulator. This calibration algorithm needs to operate over a wide bandwidth and environmental conditions. Noon [3] presented a technique to calibrate such a system, but mentions that the homodyne architecture is not the best for implementing SFCW GPR.

Finally, the DC signal in the homodyne receiver is subject to flicker noise and temperature drift. Although in general homodyne systems require less components and therefore have a lower manufacturing cost they suffer from problems which are difficult to solve effectively.

4.5.2 Heterodyne Dual Synthesizer Architecture

A heterodyne radar architecture synchronously detects the radar returns by mixing the received signal down to an intermediate frequency (IF), and in doing so, overcomes all of the limitations of the homodyne systems. Iizuka [32, 35, 79] and Uratsuka [107] were the first researchers to implement a SFCW GPR using this architecture. Pourier [31] from Ohio State University also mentions that this architecture was used to implement the SFCW radar system at OSU. However, the literature does not discuss the reasons for using this architecture and its implications for SFCW GPR measurements. This section presents the basic principles behind this architecture, as well as the motivation for its use in SFCW GPR.

Consider the block diagram of a dual synthesizer SFCW GPR shown in Figure 4.2.

The system consists of separate transmit and receive synthesizers. Each synthesizer is locked to a common reference oscillator, and offset from one another by the radar IF (f_{IF}). The transmit synthesizer is amplified and radiated through an antenna, reflects off a target and received by the radar. This RF signal is mixed with the receive synthesizer signal and then filtered at the IF. Since the IF can be designed to be *far away* (large frequency offset) from DC, the heterodyne architecture reduces the problem of temperature drift and alleviates the problem of flicker noise experienced by homodyne systems.

A further advantage provided by the heterodyne architecture is the absence of the requirement to filter the RF harmonics generated by the transmit and receive synthesizers. Consider the following transmit and receive synthesizer signals, namely $f_{\mathrm{TX}} = nf_{\mathrm{C}}$ and $f_{\mathrm{RX}} = m\left(f_{\mathrm{C}} + f_{\mathrm{IF}}\right)$, where f_{TX} and f_{RX} are the respective output frequencies of the two synthesizers. The frequencies at the output of the mixer are given by Equation 4.1.

$$f_{\mathrm{IF}}^{m} = \begin{cases} mf_{\mathrm{C}} + mf_{\mathrm{IF}} + nf_{\mathrm{C}} \\ mf_{\mathrm{C}} + mf_{\mathrm{IF}} - nf_{\mathrm{C}} \end{cases} \tag{4.1}$$

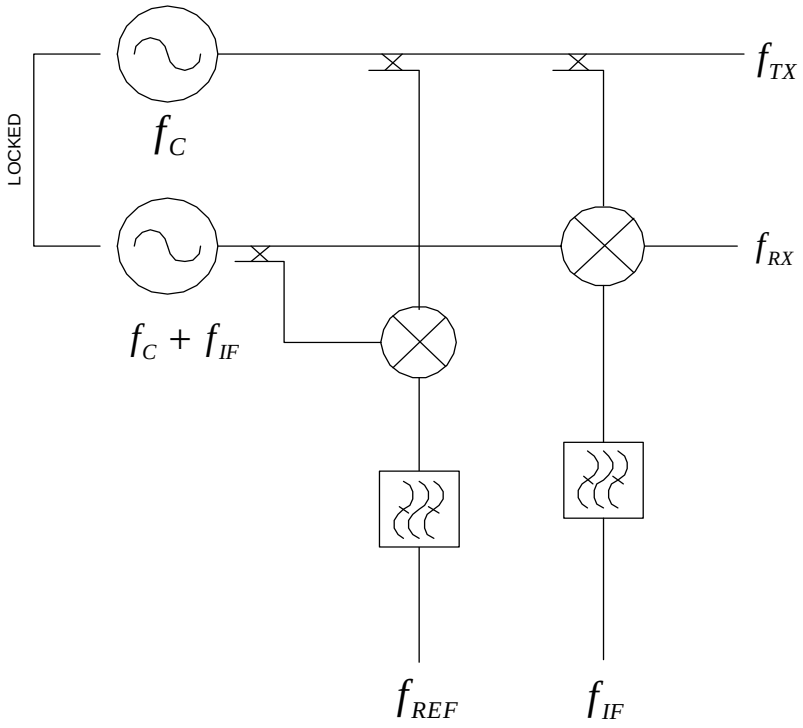

Figure 4.2: Block diagram of a heterodyne radar architecture

Ignoring all frequencies greater than f_C, the frequency at the input to the IF filter is given by $f_{IF}^m = mf_{IF}$, where f_{IF} is the IF resulting from the fundamental frequency of the synthesizer. Hence each harmonic of the IF corresponds to a harmonic of the transmit and receive synthesizer. Practically, this radar architecture reduces filtering of the harmonics at the RF to a simpler problem of filtering the harmonics at the IF.

Extracting the I and Q values from the intermediate frequency can be achieved digitally, by direct IF sampling and digital quadrature demodulation [118]. The IF signal in the above system is a narrow band signal and represents a far simpler problem than the case discussed in the literature. Direct sampling in combination with digital demodulation is an important advantage, since it removes all the problems associated with baseband IQ demodulators as discussed in Section 4.5.1. The details of the IQ demodulator are discussed in Section 4.6.5.

4.6 Radar Design

For the reasons presented in the previous section, the SFCW GPR implemented in this thesis uses the heterodyne architecture. To ensure low cost and small size, the synthesizers are implemented using standard off-the-shelf direct digital phase lock loop synthesizer technology and radio frequency components. In addition, most of these components are low power devices, enabling for the design of a low power SFCW GPR. In order to make this architecture practically viable, it is necessary to consider some important design aspects that will allow one to implement this type of SFCW system. These factors include synthesizer coherency, system phase noise, effects of temperature variations and implementation of an IQ demodulator. In this section, a proposed architecture for the SFCW GPR will be presented, followed by a discussion of the various design issues.

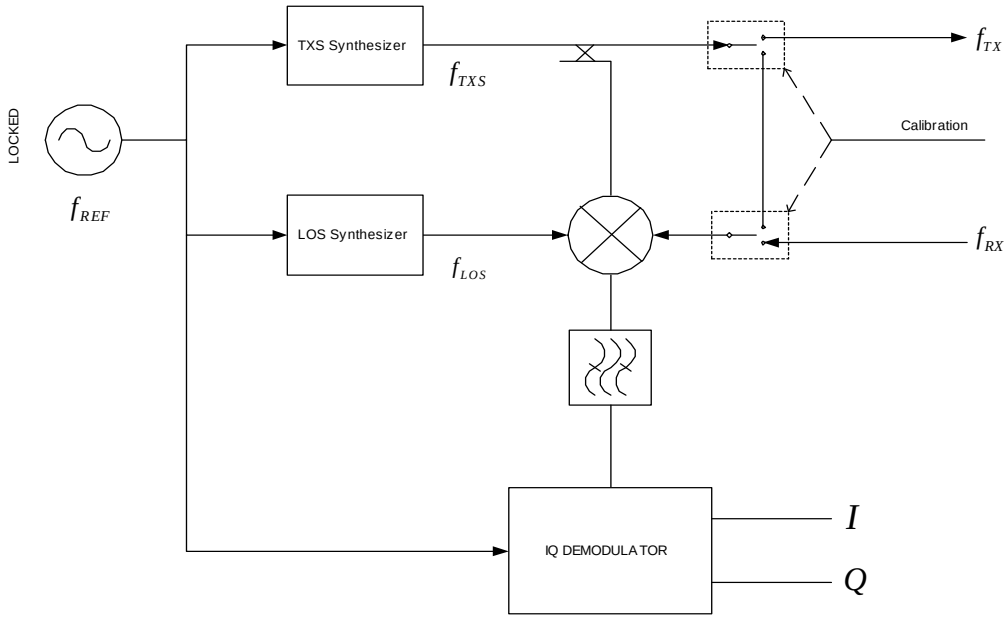

Figure 4.3: Block diagram of the Stepped Frequency Continuous Wave GPR

4.6.1 Radar Architecture

Figure 4.3 shows the basic radar architecture for the MercuryB and MercuryA SFCW GPR system.

The radar consists of two digital phase lock loop RF synthesizers both locked to the same reference frequency oscillator and offset by an IF (f_{IF}). The received signal is mixed with the local oscillator signal f_{LOS} and filtered to generate the IF (f_{IF}). The IF is converted to baseband inphase and quadrature signals using a digital IQ demodulator referenced to the master reference oscillator (f_{REF}). A calibration loop is provided to remove any systematic errors due to the RF circuitry.

4.6.2 System Coherency

Stepped frequency radar relies on the measurement of the phase difference between the transmitted and received signals. To measure this phase difference, there must be a reference of the transmitted signal phase. In general, radar coherency relies on the synthesizers and the sampling process being synchronized to the same master oscillator. This ensures that the phase measured at the intermediate frequency channel can be related back to the transmitted signal and therefore the phase difference measured.

Two methods exist to practically achieve system coherency. These are listed below.

- *The use of a separate reference channel.* The reference signal is generated by mixing signals coupled from the transmit and local oscillator synthesizers, hence providing a signal that contains the same transmit and local oscillator synthesizer errors as the receive signal. This is the standard technique used by most SFCW radars. However this method is limited by the fact that the reference and received channels use different components. This results in component matching errors which leads to phase and amplitude differences between the reference and receive channels. Complex calibration is required to remove these measurement errors. In addition the need for an extra reference channel, increases the system complexity and cost.

- *The use of a single reference channel and a calibration loop.* In Figure 4.3, switches are used to either multiplex the received signal or the transmitted signal to the intermediate frequency hardware. This architecture solves the problem of component matching discussed in the previous method, since it only uses a single channel IF. In addition, by using only a single channel, the hardware cost and complexity is reduced. In practice, the switches will have a limited isolation that will result in signal coupling between the transmit and reference channels. This is, however, limited as a result of the high isolation achievable with current low cost switches. Typically more

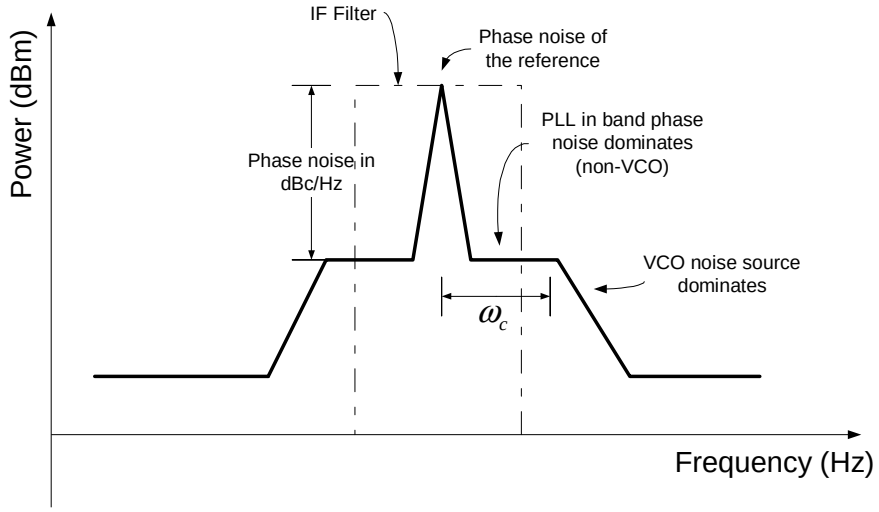

Figure 4.4: Typical phase noise plot for a PLL [1]

than 80dBs of isolation can be achieved with two switches low cost RF switches.

4.6.3 System Phase Noise

Consider the phase noise spectrum of the digital phase lock loop (DPLL) frequency synthesizer used to generate the transmit and local oscillator signals[1]. Within the loop the phase noise is determined by the phase noise of the reference oscillator, the PLL dividers, the loop filter and the phase detector - with the primary signal power coming from the reference source, as is shown in Figure 4.4.

Since within the loop bandwidth the synthesizer's phase noise is coherent with the reference oscillator, the two synthesizers are also phase coherent with each other. Outside the loop bandwidth the phase noise is that of the voltage controlled oscillator - which is uncorrelated to each of the transmit and receive synthesizers. Since the delay of the receive signal relative to the LOS (local oscillator synthesizer) signal is small for subsurface measurements (i.e. typically

[1] All synthesizers in the radar system use the DPLL technology.

less than 200 ns), the phase noise within the loop bandwidth of the received signal is also correlated with the LOS signal.

Hence in the mixing process, the phase noise within the loop bandwidth will reduce (subtracting two correlated phase sources) and outside the loop bandwidth will increase since the noise is correlated. It is thus essential to choose the IF bandwidth to be less than or equal to the loop bandwidth of the synthesizers. This reduces the phase noise at the output of the IF filter. Figures 4.5 and 4.6 show the results of phase noise cancellation for the 1000 MHz to 2000 MHz MercuyA radar system with the transmitter and receiver connected via two metres of RF cable - clearly showing the phase noise improvement over the 200 Hz to 12 kHz frequency band. The peak phase noise improvement is approximately 12 dB at a frequency of 10 kHz.

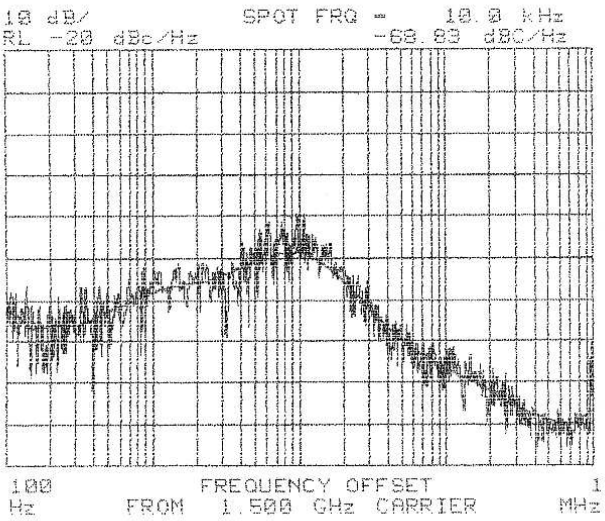

Figure 4.5: Measured phase noise for the MercuryA transmit synthesiser at 1.5 GHz

To remove the effects of uncorrelated noise, outside the loop filter bandwidth, the IF bandpass filter should be designed such that its bandwidth is less than twice the PLL loop cutoff frequency, as is shown in Figure 4.4. Figure 4.7 shows

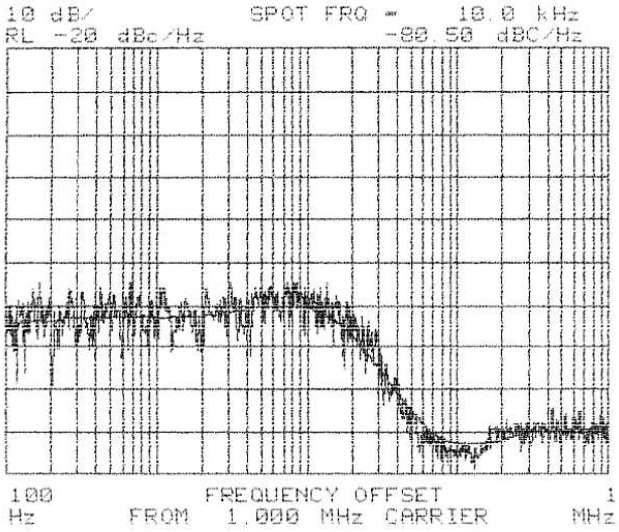

Figure 4.6: Measured IF phase noise at 1 MHz for the MercuryA radar with a transmit frequency of 1.5 GHz

the measured IF frequency after filtering for the MercuryA radar system.

4.6.4 Effects of Temperature Variations

Any variation in temperature of the reference oscillator will result in variations in phase at the output of the synthesizers and hence radar system. This is also true for any temperature variations of the active electronic components. This is a further motivation for using a reference channel in the radar design. In the current radar system the time between sampling the reference and receive channels is small compared to the time constant for temperature variations. This ensures that the phase changes due to temperature will be the same for both channels, and can be removed by calibration.

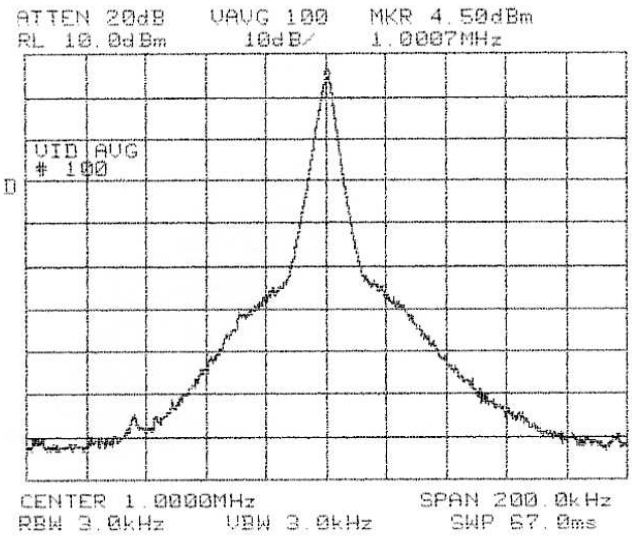

Figure 4.7: Filtered IF for the MercuryA radar system

4.6.5 Implementation of an IQ Demodulator

An essential element of the radar system design is the IQ demodulator. This section presents a simple and novel implementation, that is both straight forward to implement and low cost.

Consider an IF with an amplitude with respect to time described by $x(t)$. The sampling process records a sampled version of the narrow band IF signal (assuming no noise), such that $x\,[n]$ is given by

$$x[n] = A\sin\left(2\pi f_{\mathrm{IF}} nT + \phi\right) \tag{4.2}$$

where

- T is the sampling interval given by $T = MT_{IF} + T_S$.
- T_s is the effective sampling interval defined as $T_s = \frac{1}{N}T_{IF}$. The sampling frequency is also constrained by the Nyquist rate, such that $T_s > \frac{1}{2B}$ and

B is the bandwidth of the IF stage.

The integer N defines the number of samples per cycle of the IF. The integer M defines the number of cycles of the IF waveform skipped between samples. The advantage of this technique is that it allows one to use lower cost analogue-to-digital convertors (ADC) to sample high frequency IF signals, as long as the sample and hold is fast enough. The sampling mechanism is illustrated in Figure 4.8 for $N = 4$, and $M = 1$

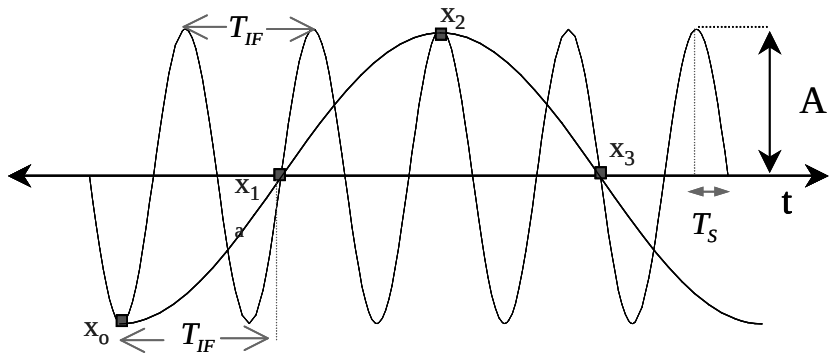

Figure 4.8: Graphical view of the sampler for a SFCW GPR

Assuming that four samples of the IF have been captured, the in-phase and quadrature (I and Q) values can be determined from $x[n]$ by digitally mixing $x[n]$ with $cos(\omega_{IF} nT)$ and $sin(\omega_{IF} nT)$ and then taking the DC component of the result. This is equivalent to multiplying the IF signal with $\exp(-j\omega_{IF} nT)$ and taking the real and imaginary parts of the results.

$$X = \frac{1}{N} \sum_{n=0}^{N-1} x[n] \exp\left(-j\frac{2\pi n}{N}\right) \tag{4.3}$$

where Equation 4.3 is simply the first harmonic of the DFT of $x[n]$. For most system, $N = 4$ provides a computationally efficient solution to I and Q, namely

$$I = \Re(X) = \frac{1}{4}(x[0] - x[2]) \tag{4.4}$$

$$Q = \Im(X) = \frac{1}{4}(x[3] - x[1]) \tag{4.5}$$

In Section 4.6.2 reasons were presented for the use of a single IQ demodulator with a reference channel in the transmit receive path and all radar timing relative to a master reference oscillator. For this radar configuration to work, it is essential that the IF samples from the receive path and the IF samples from the reference path are synchronized relative to each other - thus ensuring a constant phase difference between the IQ values. This is achieved by keeping track of the sample number, by keeping a reference of the count of the sample number in base N. This count provides the important information as to where on the IF waveform the data was sampled - providing a common reference for both the receive and reference channels.

Consider a sampled data stream **x,** corresponding to a set of samples from the ADC, such that $x_l = x[lT]$ and $T = \frac{1}{4}T_{IF}$ ($N = 4$ and $M = 0$). Then, the synchronized sampling stream is given by $y_d = x[(l \bmod N)T]$, where $d = l \bmod N$ and $d = 0, 1, \ldots, N-1$. This process can be illustrated by a simple example. Consider a set of measurements over some interval t, such that $3T \leq t \leq 11T$, then the captured sequence of data is given by

$$x_3, x_4, x_5, x_6, x_7, x_8, x_9, x_{10}, x_{11} \tag{4.6}$$

Assume that at time $t = 3T$, the received channel data is captured. The received data vector $\mathbf{y}$ is given by,

$$\mathbf{y} = (y_0, y_1, y_2, y_3) = (x_4, x_5, x_6, x_3) \tag{4.7}$$

Assume that at time $t = 8T$, the reference channel data is captured. The reference data vector $\mathbf{y}'$ is given by

$$\mathbf{y}^{'} = (y_0^{'}, y_1^{'}, y_2^{'}, y_3^{'}) = (x_8, x_9, x_{10}, x_{11}) \tag{4.8}$$

Hence both vectors are synchronized.

4.7 Radar Implementation

This section presents a brief description of the implementation of the MercuryB 200 MHz - 1600 MHz SFCW GPR, with its system specification listed in Table 4.1.

Operating frequency	$200 - 1600$ MHz
Bandwidth	1400 MHz
Frequency step size	2 MHz
Maximum number of frequency steps	700
Transmit power	-15 dBm to 10 dBm
Maximum receive signal (1dB compression point)	-35 dBm
Noise floor	-145 dBm
Scan Rate	5 Hz
Dynamic Range	>70 dB
Antenna Type	Shielded cavity backed loaded bowtie.
Weight	4 Kg
Power	12 W
Power Source	Lead acid battery 12 V 4 Ahr

Table 4.1: MercuryB specification summary

This implementation is similar to the MercuryA system - with differences mainly in the mechanical form factor and data capture software. For this reason only the MercuryB implementation will be presented. For more details the reader is referred to [46].

The radar can be divided into a number of modules as shown in Figure 4.9.

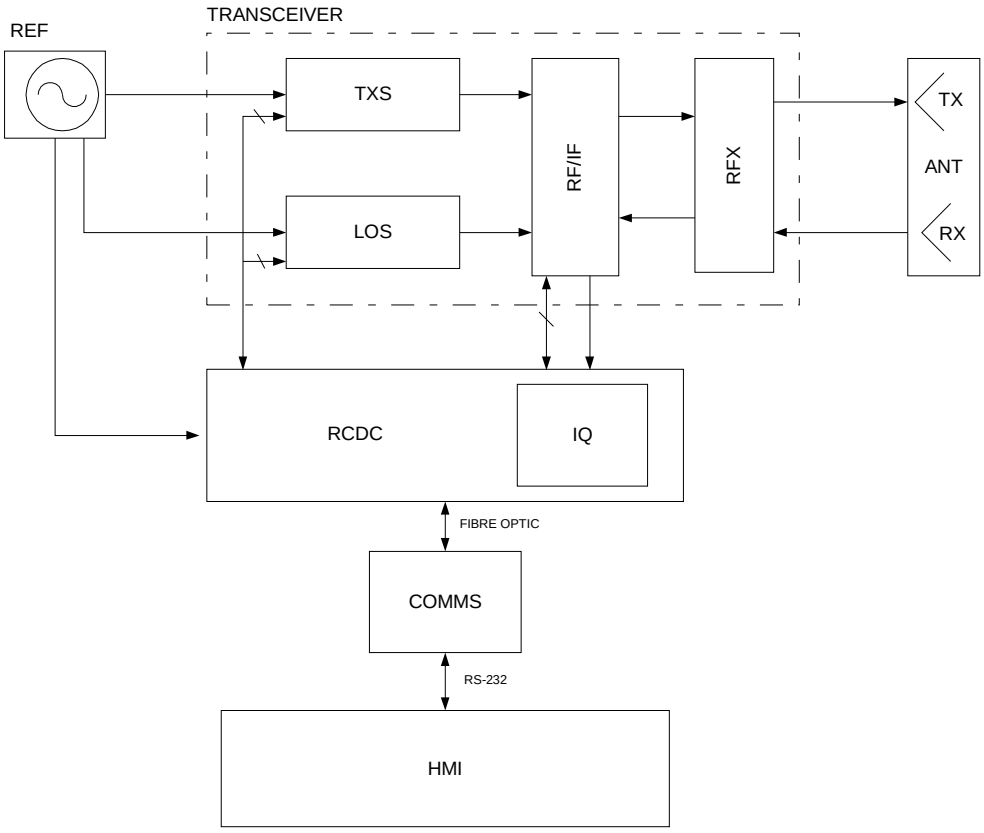

Figure 4.9: Block diagram of the implementation of the MercuryB radar system.

Each of these modules is listed below along with a brief discussion.

- **Frequency Reference Module (REF)** is the master oscillator of the system, that provides the reference to the synthesizer modules as well as to the sampling system. Since differential measurements are taken at each frequency, it is not essential to use an expensive temperature compensated oscillator.

- **Radar Controller/ Data Capture Module (RCDC)** controls the generation of radar frequencies and capture of the received coherent data for each radar scan. At the heart of the RCDC is a microcontroller which controls the various radar modules as well as implements a simple communication protocol that allows the radar to communicate with a personal computer. The digital sampling circuitry is implemented using Field Programmable Gate Array (FPGA) technology and a low cost ADC. The FPGA generates all the timing and control signals to capture the IF data and implements the IQ demodulation scheme. It also includes hardware averaging to reduce uncorrelated noise in the receive signal.

- **Communications Module (COMMS)** provides a fibre optic link from the radar to the PC. This serves to isolate the radar from the switching noise of the PC, that is to reduce the Electromagnetic Interference (EMI). The fibre optic link allows one to separate the transceiver from the human machine interface (up to 50 M). The communication module plugs into a standard 9 pin RS-232C port on the computer and connects to the radar via low cost plastic fibre.

- **Human Machine Interface (HMI)** provides a visual interface for the radar. It provides the functionality to control the radar and capture and display the data in various formats. The HMI is divided into two software modules; a radar server which provides a public internet enabled Common Object Request Broker Architecture (CORBA) interface to the radar hardware and a client component that displays and captures the data. In addition various signal processing algorithms have been implemented to

enhance the radar display, including software compensation for the signal attenuation with distance from the radar. Currently the software simply displays the impulse response of the captured data - the algorithms discussed in this thesis have yet to be implemented in the radar client software.

- **Transceiver module (TRANS).** The radar transceiver is the heart of the radar system and implements the heterodyne architecture discussed in Section 4.5 and 4.6. It consists of four modules

  - **Transmit Synthesizer (TXS).** This generates a low power signal that is amplified and transmitted via the antennas. The synthesizer covers a 200 MHz to 1600 MHz bandwidth with a 2 MHz step size. It is implemented using a standard DPLL synthesizer architecture [1] that operates over an octave bandwidth from 800 MHz to 1600 MHz. A programmable 2/4 divider is used to extend the TXS frequency range down to 200 MHz. The synthesizer includes 30 dBs of gain control, which allows one to compensate for gain variations in the system.
  - **Local Oscillator Synthesizer (LOS)** is exactly the same as the TXS synthesizer. It generates the required local oscillator signal (offset from the TXS by the IF frequency) that when mixed with the received signal, results in the IF.
  - **RF/IF (RFIF)** translates the received signal down to the intermediate signal. It also implements the calibration channel. The IF stage has a variable gain control to allow one to maximize the dynamic range of the analogue-to-digital convertor on the RCDC module. The IF for the system is 2 MHz, with a bandwidth of 100 kHz.
  - **RF Extender Board (RFX)** currently implements the output power stage and the input low noise amplification stage (LNA). The board provides the ability to extend the RF functionality of the radar.

- **Antennas (ANT):** The antennas used for the radar system were cavity backed, resistively loaded dipoles covering a 600 MHz to 1200 MHz band.

These were designed and built by Ball Aerospace. The antenna isolation between the transmit and receive antenna when co-polarized was approximately 30 dBs.

- **Power Supply Unit (PSU)** coverts a DC power supply from 9 - 18 volts (typically a 12 V battery) to the required system voltages for each of the radar modules. Heavy filtering was implemented and strict adherence to EMI design principles [119] was maintained to ensure very low noise ripple to the RF modules. The measured RMS noise on the RF power lines was less than 1 mV RMS.

The MercuryB radar transceiver was implemented using standard 3U Eurocard boards that plugged into a proprietary backplane and mounted in an off-the-shelf enclosure. Figure 4.9 shows a picture of the radar transceiver system.

Figure 4.10: Photograph of the MercuryB radar hardware.

The radar architecture is mechanically divided into four logical units - a power supply board, the transceiver board the RF extender board and the Radar Data

Capture and Controller Board. The modules in the transceiver board consist of four daughter boards that plug into an RF motherboard. This provides mechanical rigidity for the daughterboards as well as RF isolation The RF components are mounted on the underside of the daughter boards such that they face the ground plane of the RF motherboard. The daughter boards are fixed to the motherboard using conductive spacers.

The MercuryA system was designed to fit a custom mechanical enclosure. A photograph of this system is shown in Figure 4.11

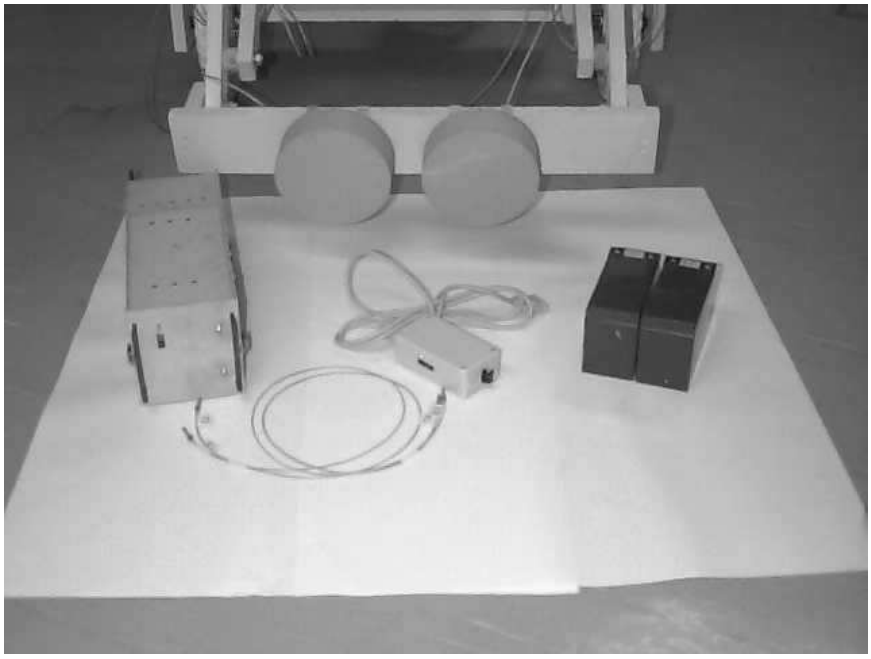

Figure 4.11: Photograph of the MercuryA radar system including the radar transceiver, fibre optic communication link, batteries and antennas

It is important to note that the size of both systems were smaller than most of the SFCW GPR systems [21, 23, 18]. It is also important to note that this system is a prototype and that there is scope for improvement. For example with design improvements it is relatively trivial to increase the radar scan rate to $>$ 50 Hz.

4.8 Radar Measurements

This section presents measurements to demonstrate the performance of the radar. Note that some measurements have already been presented in Chapter 2. All data was captured and processed using the HMI software. The results presented are screen captures from the HMI. All results presented were captured with the MercuryB radar system, except for the last set of measurements which shows results for the MercuryA system.

4.8.1 Measurement 1: Back Yard

The data was collected in the back yard of a home in Cape Town, South Africa, where cables were known to run underneath the yard paving. Figure 4.12 shows the processed results assuming a real permittivity of $\varepsilon_r^{'} = 6$. The figure clearly shows the soil layering as well as several hyperbolic targets, which may correspond to the buried power utilities. The antennas were co-polarized.

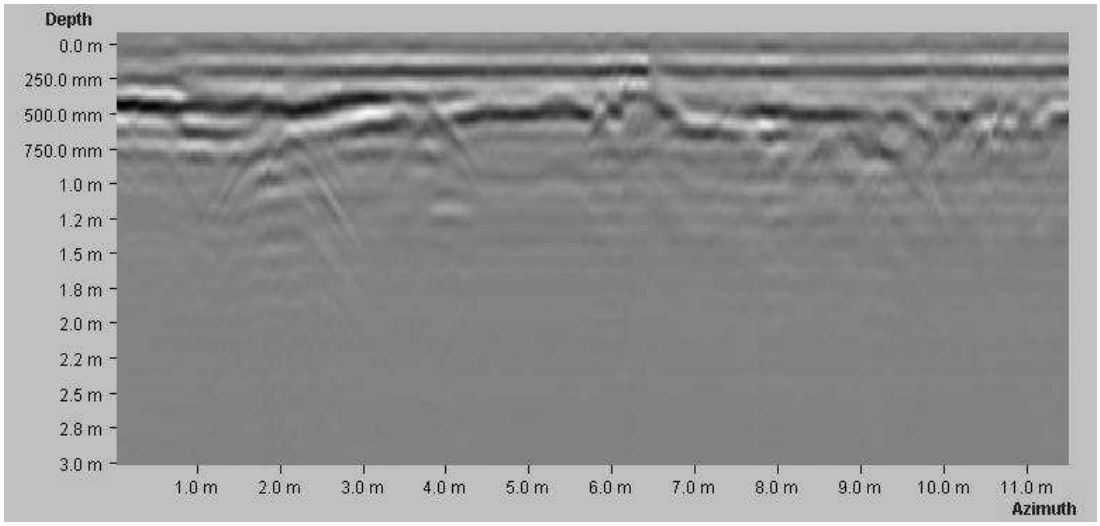

Figure 4.12: Radar profile for yard measurements

4.8.2 Measurement 2: Ball Aerospace Indoor Test Pit

In Chapter 2, measurements were presented for a pipe buried in a tub. This same measurement setup was also used to capture results with an impulse radar from Software and Sensors. Figure 4.13 shows images for data captured with the MercuryB with co-polarized bow-tie antennas (Figure 4.13(b)) and Pulse Ekko 1000 GPR (Figure 4.13(a)) systems. The Pulse Ekko system antenna had a centre frequency of 900 MHz, with an approximate bandwidth of 900 MHz, while the bowties used for the SFCW system worked from around 600 MHz to 1200 MHz. This reduction in bandwidth results in slightly poorer resolution for the MercuryB measurements.

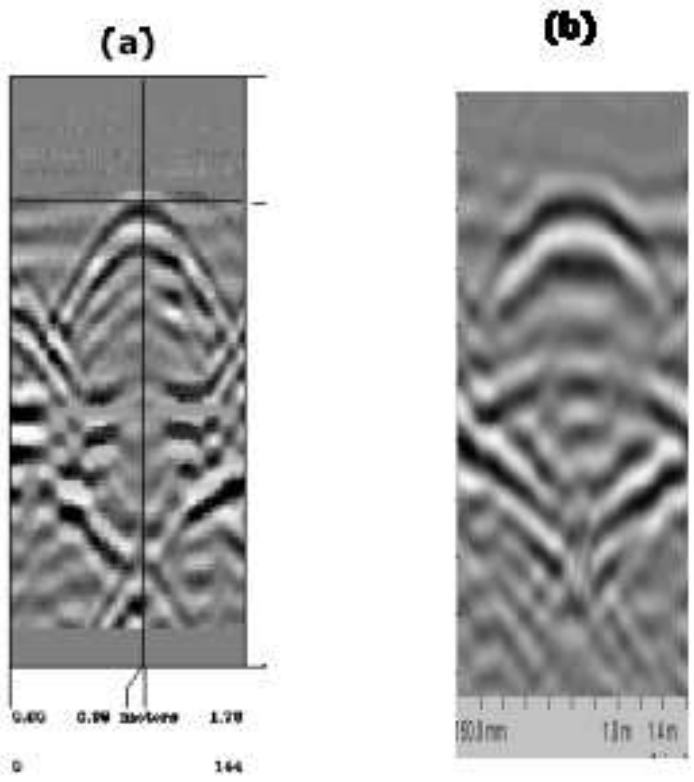

Figure 4.13: Comparison between MercuryB SFCW GPR and the Pulse Ekko 1000 impulse GPR

4.8.3 Measurement 3: Outdoor Test Pit - Ball Aerospace

An outdoor test site was constructed outside the Ball Aerospace offices in Broomfield, Colorado. The test site was constructed by digging a large pit in the ground, burying some large pipes and then refilling it. Figure 4.14 shows a profile of the edge of the site. The results clearly show the bottom and side of the pit. In addition, hyperbolas can be seen at 1 m and 1.5 m depths, that correspond to some of the buried pipes. Unfortunately detailed diagrams of the pit were not provided to the author, and hence are not included in this section. The antennas were co-polarized.

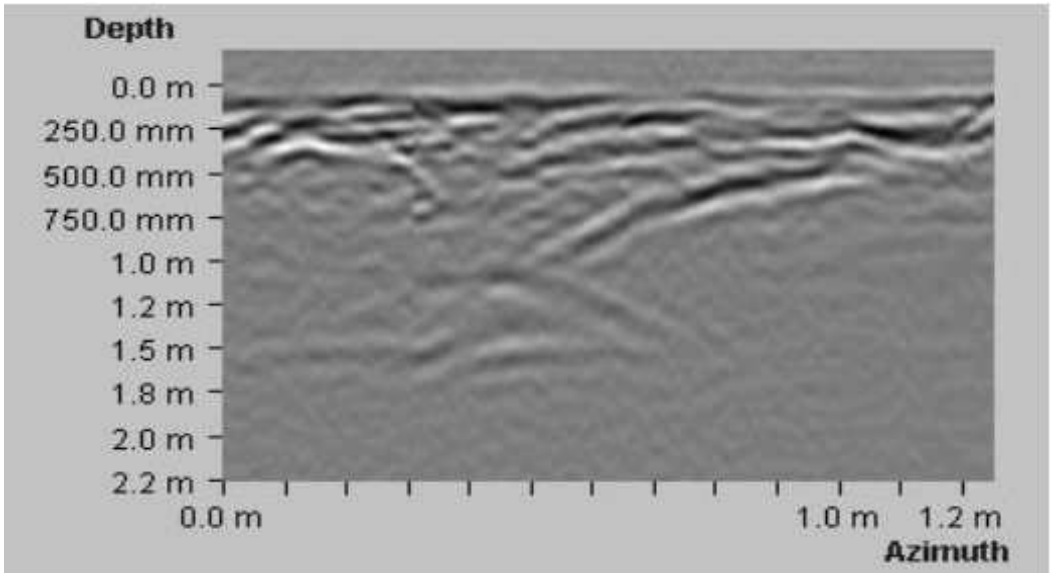

Figure 4.14: Radar profile of a test pit at Ball Aerospace, Broomfield Colorado

4.8.4 Measurement 4: Landmine Detection Measurements

The final measurement shows results of data captured with the MercuryA radar system using left and right circular polarized antennas, at a test site at CSIR in Pretoria, South Africa. An aerial photograph of the test site is shown in Figure 4.15.

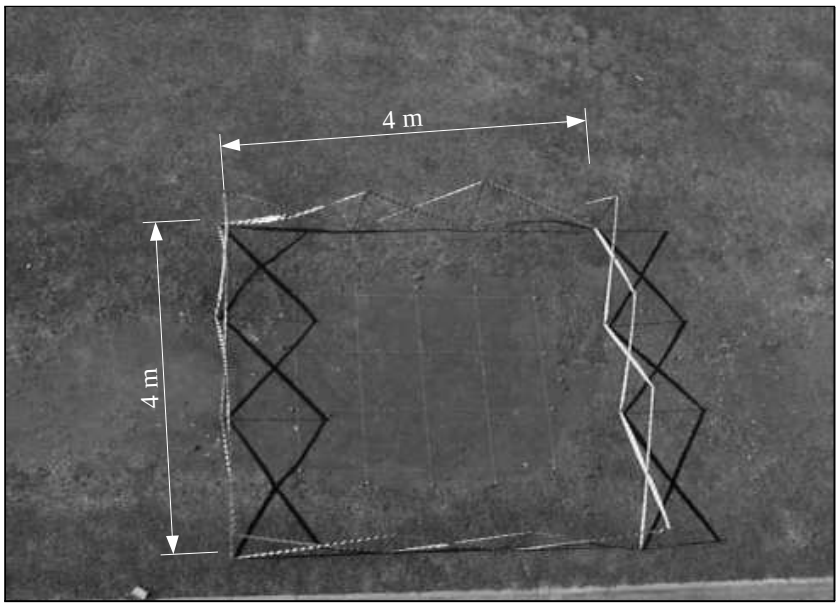

Figure 4.15: Photograph of mine test site at the CSIR, Pretoria

Various targets were buried below the surface of the test site. These targets included - a Coke can, a Bakelite mine (filled with beeswax), a PPM-2 AP mine, a metal AT mine (filled with bee's wax), rocks, screws and an explosive simulant. Figure 4.16 shows the results for a scan over the centre lane of the test pit, which crossed over the following targets (in order)

- Coke can at a depth of 5 cm.
- Bakelite mine at 15 cm.
- PPM-2 AP (antipersonnel) mine at 1 cm.
- A metal AT (anti-tank) mine at 20 cm.

In the interpretation of the results, it should be noted that the antenna coupling varied resulting from the mechanical setup on which the radar and antennas were mounted. This resulted in a variation of energy transmitted into the ground and hence scattering from the targets, and a smaller target responses from the coke

can. One also needs to consider that the radar has a much larger dynamic range than that which can be displayed on a page, and hence the larger target tend to dominate the results.

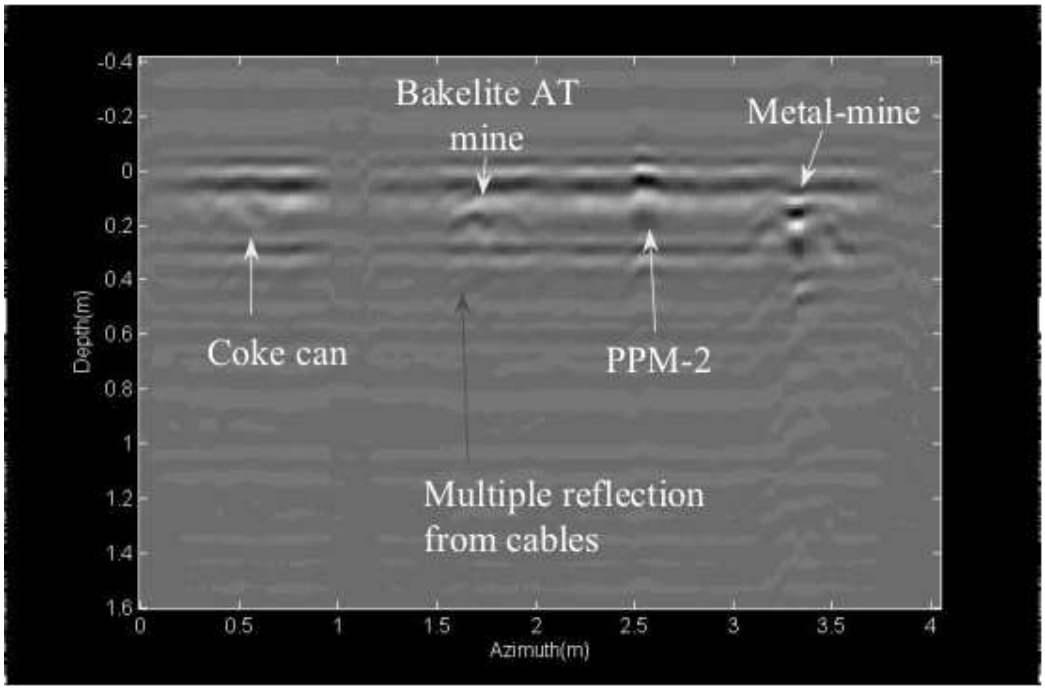

Figure 4.16: Radar profile of a cross section through the centre of the mine test site

Figure 4.16 clearly shows the reflections from each target. Note the hyperbolic edge reflections from the Bakelite and Metal AT mines.

4.9 Conclusions

This chapter has presents some of the design concepts and implementation details for the development of a low cost and compact SFCW GPR system. As far as the author is aware, these design innovations present some novel contributions to the field of SFCW GPR hardware development. Results are presented that show the performance of the radar for various applications. Comparisons

between the MercuryB and Pulse Ekko 1000 system show that the SFCW radar performed as well as the impulse radar, even in the early stages of the MercuryB development. The radar performance has been investigated in previous research under the supervision of the author [46], however it is acknowledged that more measurements still need to be performed to fully characterize the performance of the radar with the goal of generating detailed test specifications. This is an area of ongoing research.

Chapter 5

Conclusions and Scope for Future Work

5.1 Conclusions

Fully polarimetric GPR data is known to provide valuable information to aid in the detection and identification of subsurface features [24, 2, 87, 85]. However, very little attention has been given to the problem of extracting the polarimetric features from measured GPR data - hence the motivation for this work.

This thesis describes the development of an algorithm to extract features from polarimetric SFCW GPR data. This algorithm yields a set of feature vectors that are independent of the properties of the medium, and hence provide valuable information for the identification of subsurface features in unknown media. During the research, the need for low cost, compact and low power SFCW GPR equipment became apparent, and such equipment was developed.

The next sections provide detailed conclusions and future work that should flow from this investigation.

5.1.1 Single Polarization SFCW GPR

The thesis presents the development of a signal processing model based on the radar geometry and linear approximations to the wavenumber in a lossy medium. These approximations are shown to have errors of less than 0.01% for conductivities smaller than 40 mS/m. The model is shown to be equivalent to the exponential model found in signal processing theory. This provides valuable insight into the application of *Super-resolution* processing to SFCW GPR data.

The Matrix Pencil-of-Function Method is used to extract the parameters from the exponential model in a least squared sense. By relating the GPR model parameters to the exponential model, valuable insight and understanding of how the exponential model parameters relate to the properties of the medium and the radar setup, is gained. Simulations are presented to investigate the performance of the algorithm for changing medium parameters. It is shown that the estimated model parameter errors are a complex non-linear function of the conductivity of the medium, the target positions, the radar frequency and the predicted model parameters. This complex relationship between the model errors and the estimated model parameters makes it difficult to define a cutoff conductivity for which the model is no longer valid. Simulations are also performed to compare the MPM with the standard IDFT processing. It is shown that the algorithm is able to estimate the target parameters, even when it is difficult to distinguish features in the synthetic range profiles.

The algorithm is applied to real measured data, captured with the radar developed in this thesis. Given the constraints of limited calibration and medium information, the algorithm performed well for detecting the target positions for the two sets of field measurements.

5.1.2 Fully Polarimetric SFCW GPR

The single polarization GPR model is extended to a fully polarimetric SFCW GPR model. Based on assumptions that the target dispersion (resulting from the

target damping factor) is the same for all polarizations or less than the dispersion of the medium, the model is shown to be equivalent to the multi-dimensional exponential signal processing model.

The multi-snapshot Matrix Pencil-of-function Method is used to extract the scattering parameters from the measured data. These parameters are then related to the polarimetric SFCW GPR model parameters, providing valuable insight and understanding into how these parameters relate to the properties of a lossy medium.

Using a technique proposed by Kostinski [101], the Huynen target parameters are extracted from the estimated scattering matrices. Using the Huynen diagonal matrix form of the estimated scattering matrix, it is shown that these polarimetric features can be divided into two sets of parameters; those dependent and those independent on the properties of the medium. Hence, the extracted target features are both independent of the antenna polarization and orientation, and properties of the medium.

Simulations are presented to investigate the performance of this technique for changing conductivity and hence model error. The performance of the algorithm is similar to that of the single polarization case. It is shown that the medium independent parameters are more tolerant to model errors than the corresponding medium dependent parameters. However, as with the single polarization model, it is difficult to determine a cutoff conductivity for which the model is no longer valid, due to the strong non-linear dependence between the model parameter errors and the model parameters to estimate. Simulations are performed to compare the parameter estimation technique with the standard windowed IDFT processing algorithm. The results show that the developed algorithm is able to estimate the target parameters, even when the targets are not visible in the synthetic range profiles.

The algorithm is applied to real measured data, captured with laboratory measurement equipment. Given the constraints of limited calibration and properties of the medium, the algorithm is able to determine feature vectors that are different for the various buried targets, indicating the promise of this technique.

5.1.3 Hardware Development

Most of the current SFCW GPR systems are large and bulky with huge power requirements, making fieldwork difficult. The decrease in cost and size of RF and digital technologies, resulting from the wireless technology boom, has increased the feasibility for the development of compact, low cost and low power SFCW GPR systems.

This thesis presents various design concepts and implementation details, to realize such a radar system. The radar design is based on a dual heterodyne architecture, with all timing, including the IQ demodulator, relative to a single reference clock. This reduces the radars complexity and cost. The IQ demodulator is implemented using a simple digital algorithm that allows for the undersampling of the radar IF. This enables the use of low cost and high performance analog-to-digital convertors.

Results are presented to show the performance of the radar for various applications. Comparisons between the MercuryB and Pulse Ekko 1000 system show that the SFCW radar performs as well as the impulse radar. Measurements with the MercuryB system demonstrate the radars ability to detect the bottom and sides of an outdoor test site, clearly showing the new refilled portion of the site. The higher frequency MercuryA system is able to detect a number of mine simulants buried a few centimeters below the surface, clearly showing the hyperbolic reflections from the edges of the larger mine targets.

5.2 Future Work

There are a few areas for which the author believes future work should be undertaken, to improve the processing techniques and hardware developed in this thesis. A number of these areas are currently under investigation by the author and other members at the Radar Remote Sensing Group at the University. These include:

- Investigating the performance of the single polarization processing technique for increasing medium losses using measured data for which the scattering of the various targets and the properties of the medium are known. This would involve the setting up of a measurement facility for which the losses of the medium could be increased in a controlled manner and for which these properties can be accurately determined. Detailed analysis of the required antennas should be included in this investigation to provide detailed antenna information to the processing algorithms. This information would include antenna beam patterns as a function of frequency and position. Comparisons could then be made between the measured scattering data and that predicted by the model. Comparison with simulated data using the FDTD method would be an advantage.

- A detailed investigation of the model error for both the single and fully polarimetric models for increasing conductivity - to determine a method of predicting the performance of the parameter estimation algorithm based on the properties of the medium and the measured data. This would also provide increased understanding of the results presented in this document.

- The development of polarimetric calibration techniques for SFCW GPR data.

- Investigating the performance of the fully polarimetric processing technique for increasing medium losses using measured data for which the scattering of the various targets and the properties of the medium are known. This would involve the use of the measurement facility mentioned in the first point of this section. Further analysis of the antenna polarization would be required to understand the polarization of the electromagnetic radiation incident on targets located at various depths.

- Extension of the polarimetric model to more complex anisotropic media as well as more detailed models for the medium properties.

- Investigating the use of the medium independent polarimetric feature vectors for the detection and identification of subsurface targets - using large sets of measured and simulated SFCW GPR data.

- The development of a fully polarimetric SFCW GPR and the comparison of its performance with other available GPR systems. This should include a detailed system analysis through both simulation and laboratory measurements.

Appendix A

Linearization of the Wavenumber k_m

In this appendix the Maclaurin series expansion of a function together with the binomial series expansion is used, to approximate the wavenumber k_m and hence α_m and β_m at high frequency and/or low conductive loss.

Chapter 3 defined that $k_m = \beta_m - j\alpha_m$ where

$$k_m = \frac{\omega}{v}\sqrt{1 - j\tan(\delta)} \tag{A.1}$$

and $\tan\delta$ is the loss tangent of the medium and is given by

$$\tan(\delta) = \frac{\sigma^{'} + \omega\varepsilon^{''}}{\omega\varepsilon^{'}} \tag{A.2}$$

Letting $x = \tan\delta$, the function $f(x)$ can be defined, such that

$$\frac{\omega}{v}f(x) = k_m(x) \tag{A.3}$$

where

$$f(x) = \sqrt{1 - jx} \tag{A.4}$$

The Maclaurin series of the function $f(x)$ is the series

$$\sum_{n=0}^{\infty} \frac{f^{(n)}(0)}{n!} x^n \tag{A.5}$$

where $f^{(n)}(0)$ indicates the n^{th} derivative of $f(x)$ evaluated at $x = 0$ and is given by

$$\begin{aligned} f^0(0) &= 1 && \text{for } n = 0 \\ f^n(0) &= -\prod_{u=0}^{n-1} j \left| u - \tfrac{1}{2} \right| && \text{for } n = 1, 2, 3, \ldots \end{aligned} \tag{A.6}$$

Using the Ratio Test for the convergence of a power series, it can be shown that Equation A.5 converges for $|x| < 1$, i.e. $|\tan \delta| < 1$.

A.1 Case 1: Purely Conductive Losses

If the losses are purely conductive, then $\tan \delta = \frac{\sigma}{\omega \varepsilon'}$, and hence the Maclaurin series of $k_m(x)$ is

$$\begin{aligned} k_m(x) &= \frac{\omega}{v} \left[1 - \frac{1}{2} j \frac{\sigma}{\omega \varepsilon'} + \frac{1}{8} \left(\frac{\sigma}{\omega \varepsilon'} \right)^2 + \cdots \right] \\ &= \frac{\omega}{v} - \frac{1}{2} j \frac{\sigma}{v \varepsilon'} + \frac{1}{8} \frac{\sigma^2}{\omega v \left(\varepsilon' \right)^2} - \cdots \end{aligned} \tag{A.7}$$

which can be approximated as

$$k_m(x) \approx \frac{\omega}{v} - \frac{1}{2} j \frac{\sigma}{v \varepsilon'} \tag{A.8}$$

and noting that $k_m = \beta_m - j\alpha_m$

$$\alpha_m \approx \frac{1}{2}\frac{\sigma}{v\varepsilon'} \tag{A.9}$$

$$\beta_m \approx \frac{\omega}{v} \tag{A.10}$$

for $\frac{\sigma^2}{\omega v\left(\varepsilon'\right)^2} \ll 1$.

A.2 Case 2: Purely Dielectric Losses

If the losses are purely dielectric, then $\tan\delta = \frac{\varepsilon''}{\varepsilon'}$, and hence $k_m(x)$

$$k_m(x) = \frac{\omega}{v}\sqrt{1 - j\frac{\varepsilon''}{\varepsilon'}} \tag{A.11}$$

and noting that $k_m = \beta_m - j\alpha_m$

$$\alpha_m = \mathrm{Im}\left(\sqrt{1 - j\frac{\varepsilon''}{\varepsilon'}}\right) \tag{A.12}$$

$$\beta_m = \mathrm{Re}\left(\sqrt{1 - j\frac{\varepsilon''}{\varepsilon'}}\right)\frac{\omega}{v} \tag{A.13}$$

Hence no approximations are required for media with purely dielectric losses.

A.3 Case 2: Combined Conductive and Dielectric Losses

Next consider binomial expansion of x^n where $x = \frac{\sigma' + \omega\epsilon''}{\omega\epsilon'}$.

$$\begin{aligned}\left(\frac{\epsilon^{''}}{\epsilon^{'}}+\frac{\sigma^{'}}{\omega\epsilon^{'}}\right)^{n} &= \left(\frac{\epsilon^{''}}{\epsilon^{'}}\right)^{n}\left(1+\frac{\sigma^{'}}{\omega\epsilon^{''}}\right)^{n} \\ &= \left(\frac{\epsilon^{''}}{\epsilon^{'}}\right)^{n}\left[1+n\frac{\sigma^{'}}{\omega\epsilon^{''}}+\frac{n(n-1)}{2!}\left(\frac{\sigma^{'}}{\omega\epsilon^{''}}\right)^{2}+\ldots\right] \\ &= \left(\frac{\epsilon^{''}}{\epsilon^{'}}\right)^{n}+n\left(\frac{\epsilon^{''}}{\epsilon^{'}}\right)^{n-1}\frac{\sigma^{'}}{\omega\epsilon^{'}}+\frac{n(n-1)}{2!}\left(\frac{\epsilon^{''}}{\epsilon^{'}}\right)^{n-2}\left(\frac{\sigma^{'}}{\omega\epsilon^{'}}\right)^{2}+\ldots\end{aligned}$$

hence the wavenumber $k_m(\omega)$ is given by,

$$\begin{aligned}k_m(\omega) &= \frac{\omega}{v}\left[\left(\frac{\epsilon^{''}}{\epsilon^{'}}\right)^{n}+n\left(\frac{\epsilon^{''}}{\epsilon^{'}}\right)^{n-1}\frac{\sigma^{'}}{\omega\epsilon^{'}}+\frac{n(n-1)}{2!}\left(\frac{\epsilon^{''}}{\epsilon^{'}}\right)^{n-2}\left(\frac{\sigma^{'}}{\omega\epsilon^{'}}\right)^{2}+\ldots\right] \\ &= \frac{\omega}{v}\left(\frac{\epsilon^{''}}{\epsilon^{'}}\right)^{n}+n\left(\frac{\epsilon^{''}}{\epsilon^{'}}\right)^{n-1}\frac{\sigma^{'}}{v\epsilon^{'}}+\frac{n(n-1)}{2!}\left(\frac{\epsilon^{''}}{\epsilon^{'}}\right)^{n-2}\frac{1}{v\omega}\left(\frac{\sigma^{'}}{\epsilon^{'}}\right)^{2}+\ldots\end{aligned}$$

Assuming that $\left(\frac{\epsilon^{''}}{\epsilon^{'}}\right)<1$, $\frac{1}{\omega v}\left(\frac{\sigma^{'}}{\epsilon^{'}}\right)^{2}<<1$ and $|\tan\delta|<1$) then

$$\begin{aligned}\frac{\omega}{v}\sum_{n=0}^{\infty}\frac{f^{(n)}(0)}{n!}\left(\frac{\epsilon^{''}}{\epsilon^{'}}+\frac{\sigma^{'}}{\omega\epsilon^{'}}\right)^{n} &\approx \frac{\omega}{v}\sum_{n=0}^{\infty}\frac{f^{(n)}(0)}{n!}\left(\frac{\epsilon^{''}}{\epsilon^{'}}\right)^{n} \\ &\quad+\sum_{n=0}^{\infty}\frac{f^{(n)}(0)}{n!}n\left(\frac{\epsilon^{''}}{\epsilon^{'}}\right)^{n}\frac{\sigma^{'}}{v\epsilon^{''}} \qquad \text{(A.14)}\end{aligned}$$

Substituting Equation A.14 into Equation A.5 and Equation A.3 and noting that $k_m=\beta_m-j\alpha_m$ we can write the low loss high frequency approximations for α_m and β_m:

$$\alpha_m = -\sum_{n=0}^{n=\infty}\frac{\mathrm{Im}\left(f^{(n)}(0)\right)}{n!}\left(\frac{\epsilon^{''}}{\epsilon^{'}}\right)^{n}\frac{\omega}{v}-\sum_{n=0}^{n=\infty}\frac{\mathrm{Im}\left(f^{(n)}(0)\right)}{n!}n\left(\frac{\epsilon^{''}}{\epsilon^{'}}\right)^{n}\frac{\sigma^{'}}{\epsilon^{''}v} \qquad \text{(A.15)}$$

$$\beta_m = \sum_{n=0}^{n=\infty}\frac{\mathrm{Re}\left(f^{(n)}(0)\right)}{n!}\left(\frac{\epsilon^{''}}{\epsilon^{'}}\right)^{n}\frac{\omega}{v}+\sum_{n=0}^{n=\infty}\frac{\mathrm{Re}\left(f^{(n)}(0)\right)}{n!}n\left(\frac{\epsilon^{''}}{\epsilon^{'}}\right)^{n}\frac{\sigma^{'}}{\epsilon^{''}v} \qquad \text{(A.16)}$$

and hence

$$\alpha_m = \alpha_{m1}\frac{\omega}{v} + \alpha_{m2} \tag{A.17}$$

$$\beta_m = \beta_{m1}\frac{\omega}{v} + \beta_{m2} \tag{A.18}$$

Appendix B

Resolution and Spectral Shape

An important concept that appears frequently in radar theory is the concept of resolution. Wehner [27] defines the range resolution in terms of the ability to resolve point targets separated in slant range (along the line of sight) of the radar. Assuming that the received waveform has a bandwidth B (see Figure B.1), the corresponding impulse response would have a $\sin(x)/x$ envelope. The resulted time resolution $\Delta T = \frac{1}{2B}$ is given by the width of the mainlobe at the point 4 dB below the peak (a convenient criterion chosen to simplify the formula). Hence using this minimum distance one would be able to resolve the impulse response from two targets - as is shown in Figure B.2.

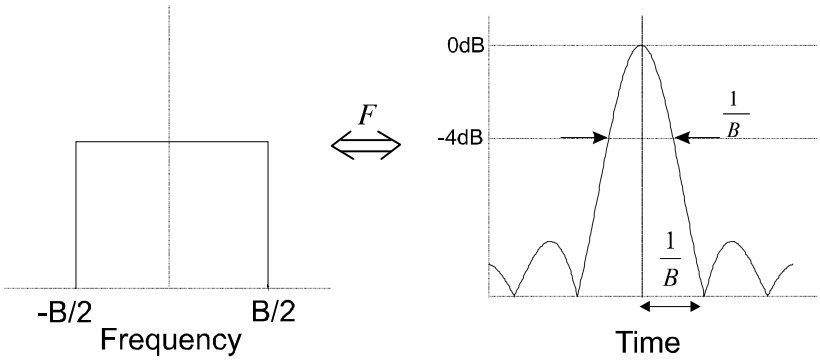

Figure B.1: Frequency/Time transform for a pulse waveform

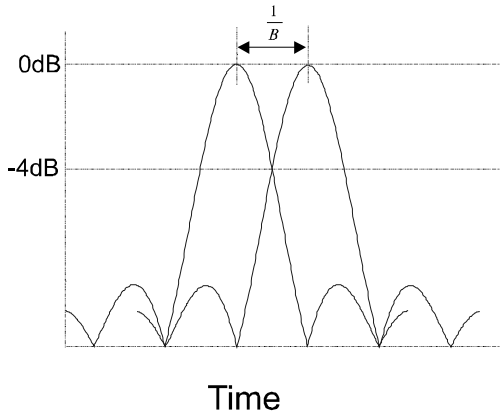

Figure B.2: Resolution of two pulses

It is important to note that in most GPR scenarios one is interested in the impulse response of the target, since time sidelobes can swamp weak, close-by targets. The corresponding target's bandwidth (target reflectivity spectrum) may not necessarily be rectangular, i.e. with corresponding time domain response.

The term "resolution" is used to provide some upper limit to the resolving power of the waveform - but this is only an approximation, with the strong assumption that our target is a point scatterer (with corresponding "infinite" reflectivity spectrum [30, 29]). When comparing resolutions of difference waveforms, one must be careful of how one defines the bandwith of the system. The concept of resolution can also be applied to cross-range resolution, depth resolution and even frequency resolution. In this appendix the discussion will be limited to depth profiles.

Recent papers have looked at the comparison between various waveforms, in particular impulse and SFCW types [53, 120]. An important criterion used in these papers is the level of side-lobes. However the radar bandwith not only relates to the radar resolution but also to the side-lobe level, when the spectral shape is considered. For a SFCW waveform, the shape of the radiated spectrum is typically limited (truncated) by the frequency range of the frequency generator - hence the spectral shape is considered to be rectangular. It is also not continuous, due to the discrete step nature of the modulation. Now, consider the case of an

impulse waveform. The bandwidth of the resulting transmitted pulse is typically truncated and shaped by the antenna response. The waveform bandwidth is then defined, typically, as the width of the waveform spectrum at 3 dB below the peak response in the bandwidth of the antenna. If one wishes to compare the resolution and sidelobe level for an impulse and SFCW waveform (using the above definitions for pulse bandwith), one would be comparing waveforms with spectra as shown in Figure B.3.

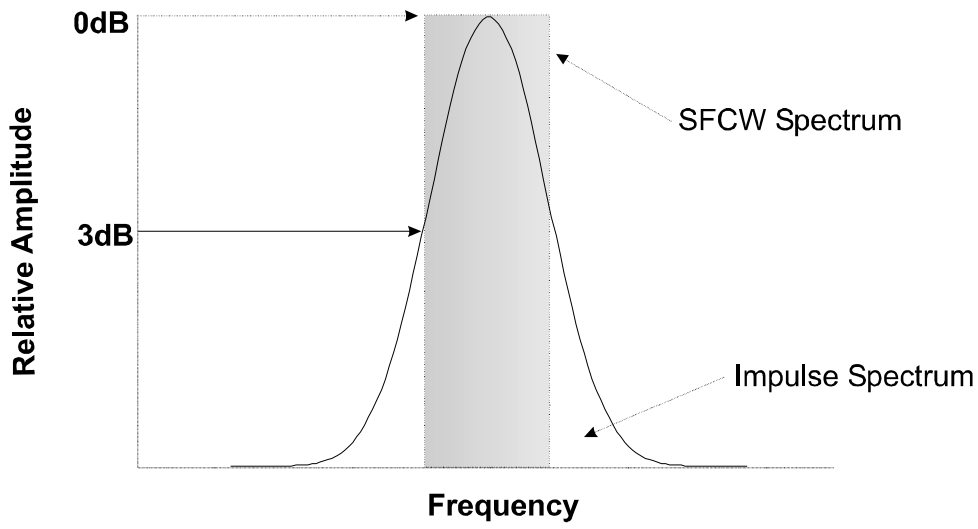

Figure B.3: Spectra of a bandlimited Gaussian pulse and conventional SFCWwaveform

The figure shows a bandlimited Gaussian shaped impulse, which has a Gaussian shaped spectrum with a SFCW radar operating over the same 3dB bandwidth. The resulting impulse response for the two waveforms is shown in Figure B.4, and the SFCW impulse response is indeed dismal.

The sidelobes of the impulse response of the SFCW can be reduced by weighting the spectrum. In fact, if the SFCW spectra is weighted with a window that has the same envelope as the envelope of the spectrum of the impulse waveform and one ensures that both spectra cover the same carrier frequency span, then both waveforms will have the same impulse response. There is thus no difference between the waveforms, based on the restricted criteria of resolution and side

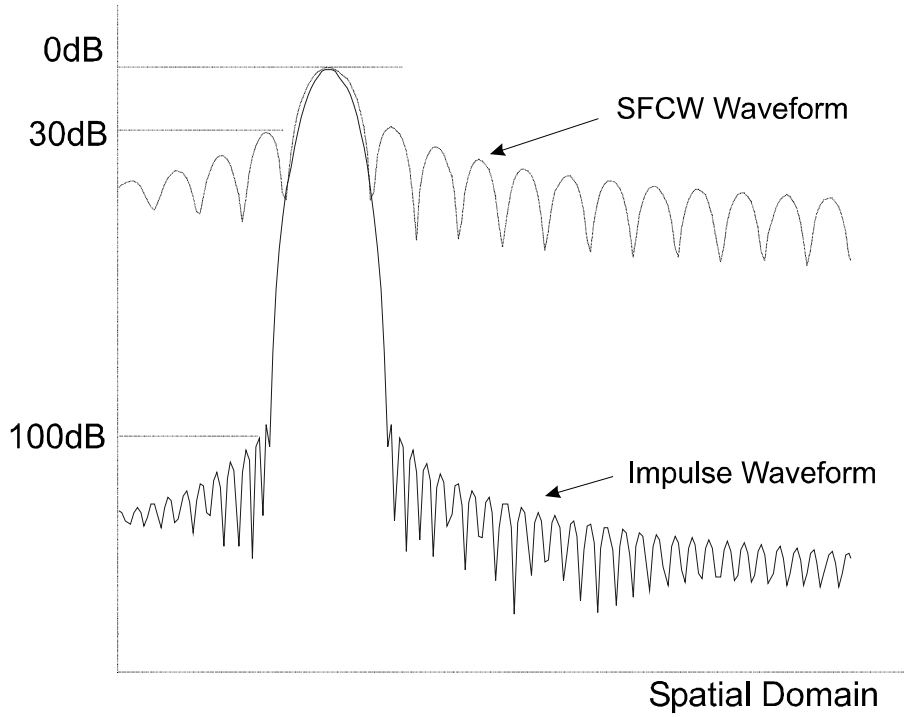

Figure B.4: Impulse response of a bandlimited Gaussian pulse and SFCW waveform

lobes. The results will be the same as shown in Figure B.4, except the synthetic range response is now generated by applying a Gaussian window to the frequency domain data, ensuring that the 3 dB bandwidth points are the same as that of an equivalent impulse radar waveform.

Hence, when comparing the impulse response of two waveforms, it is important to take care in how one defines the spectra. The bandwidth alone is not sufficient. The GPR literature is full of papers comparing the impulse response of the baseband pulse and SFCW modulation techniques, however most miss the simple point that theoretically the waveforms can be made identical. The differences lies more in the implementation of the hardware and the algorithms used to extract the information from the radar waveforms. With the growing interest by regulatory authorities [4] in the EMC of GPR, the impulse repetitive nature of pulsed systems may not be as attractive as the equivalent SFCW system, which has possibilities of sophisticated spectral control.

Appendix C

Error Analysis for an IDFT Based Target Parameter Estimation

This appendix presents an analysis of the performance of the IDFT estimator when the true GPR model is described by Equation 2.21 in Chapter 2. The effects on target position and model dispersion are investigated. The analysis below is only important when using the IDFT to estimate the parameters for the target reflection. For simplicity the effects of noise will be ignored ($n_x' \to 0$) since the effects of inaccuracies of d_p and λ_p are independent of the noise.

Model Inaccuracies Due to d_p with $\lambda_p = 0$

Consider a single target at a position d_p such that $d_p = m\Delta d + \kappa\Delta d$ where $\kappa \in \Re$, $-0.5 \leq \kappa < 0.5$ and with amplitude A_o. Equation 2.53 can then be written as

$$v_x'^r[n] = A_o e^{-j2\pi p\frac{n}{N}} e^{-j2\pi\kappa\frac{n}{N}} \tag{C.1}$$

Solving Equation 2.22 for $\mathbf{b}$ where $b_l = b[l]$ for $l = 0, 1, \ldots, N-1$, it can be shown that

$$b[l] = A_o \left[e^{-j\pi(p-l-\kappa)\left(\frac{N+1}{N}\right)} \frac{\sin \pi \left(p-l-\kappa\right)}{\sin \frac{\pi(p-l-\kappa)}{N}} \right] \tag{C.2}$$

where l is the l^{th} radar range bin. For $\kappa = 0$, the model is exact and

$$\begin{aligned} b[l] &= A_o \qquad \text{for } l = v \\ b[l] &= 0 \qquad \text{for } l \neq v \end{aligned}$$

However when $\kappa \neq 0$, the signal processing model is in error and

$$\begin{aligned} b[l] &= A_o \left[e^{j\pi\kappa\left(\frac{N+1}{N}\right)} \frac{\sin \pi\kappa}{\sin \frac{\pi\kappa}{N}} \right] && \text{for } p = l \\ b[l] &= A_o \left[e^{-j\pi(p-l-\kappa)\left(\frac{N+1}{N}\right)} \frac{\sin \pi \left(p-l-\kappa\right)}{\sin \frac{\pi(p-l-\kappa)}{N}} \right] && \text{for } p \neq l \end{aligned} \tag{C.3}$$

Equation C.3 is simply the standard $\sin(x)/x$ impulse response for a point target scatterer. In order to extract A_o from Equation C.3 one would need to interpolate $b[l]$ to determine the target position for which $b(v)$ is maximum, where $(v \in \Re : 0 < v < N\Delta d)$. For multiple targets, any target that falls off a range bin will effect the estimates of other targets. In Figure C.1 the ratio of the sampled side lobe level $b\,[l]$ to the main lobe level A_o. Since $b\,[l]$ is symmetrical about $z = p\Delta d$, only the values of b_l for $l \geq p$ are displayed.

Note that the graph is normalized with respect to the measured peak side-lobe value. It can be seen that as the target moves off a position which is an integer multiple of Δz, $\dfrac{\hat{b}_l}{\hat{b}_p}$ increases for $l > p$. The sidelode level can be reduced by windowing, however this is at the expense of the width of the main lobe, since higher spatial frequencies will be attenuated. A detailed review of a number of windowing functions is included in a classical text by Harris [80]. In this thesis the Hamming window is used, since it provides a good compromise between resolution and side-lobe levels.

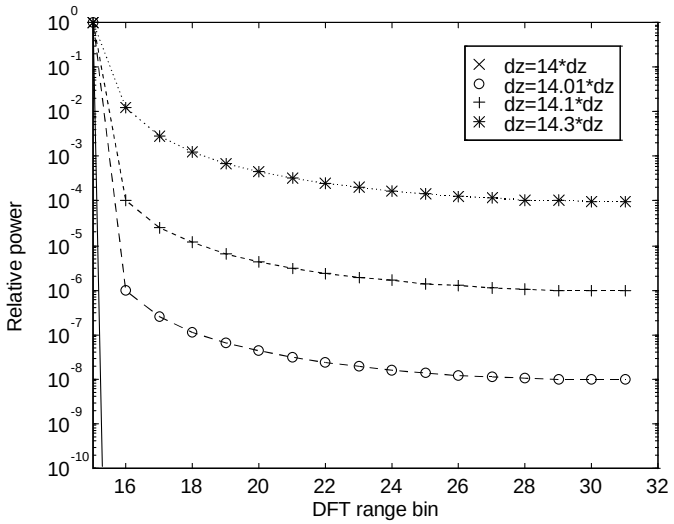

Figure C.1: Range profile for $p \geq l$ as a target is moved off a range bin

Model Inaccuracies Due to λ_p with $d_p = p\Delta d$

Consider a single target at position d_p such that $d_p = p\Delta d$. Equation 2.53 can be written as

$$v_x'^r[n] = A_o e^{\lambda_p \Delta r n} e^{-j2\pi p \frac{n}{N}} \tag{C.4}$$

Solving Equation C.4 for **b** it can be shown that

$$b[l] = A_o e^{\frac{\lambda_p}{2}\Delta r(N-1)} e^{-j\pi(p-l)\frac{N-1}{N}} \frac{j \sinh\left(\frac{\lambda_p}{2}\Delta r N\right)}{\sin\left(\pi\frac{(p-v)}{N} + j\frac{\lambda_p}{2}\Delta r\right)} \tag{C.5}$$

For $\lambda_p = 0$, the model is exact and

$$\begin{aligned} b[l] &= A_o \qquad \text{for } p = l \\ b[l] &= 0 \qquad \text{for } p \neq l \end{aligned}$$

For $\lambda_m \neq 0$, the model is in error and

$$b[l] = A_o e^{\frac{\lambda_p}{2}\Delta r(N-1)} \frac{\sinh\left(\frac{\lambda_m}{2}\Delta r N\right)}{\sinh\left(\frac{\lambda_m}{2}\Delta r\right)} \qquad \text{for } p = l$$

$$b[l] = A_o e^{\frac{\lambda_p}{2}\Delta r(N-1)} e^{-j\pi(p-l)\frac{N-1}{N}} \frac{j\sinh\left(\frac{\lambda_p}{2}\Delta r N\right)}{\sin\left(\pi\frac{(p-l)}{N} + j\frac{\lambda_p}{2}\Delta r\right)} \qquad \text{for } p \neq l$$

The exponential factor λ_p is a function of the losses in the media resulting from σ_m and ε''_m as well as the exponential damping factor of the target. Figure C.2 and C.3 show a plot of the ratio of the sampled side lobe level $b[l]$ to the measured main lobe level A_o for increasing σ_m and ε''_m - which in turn will result in increasing λ_p . Only the sidelobe level for $p \geq l$ is plotted.

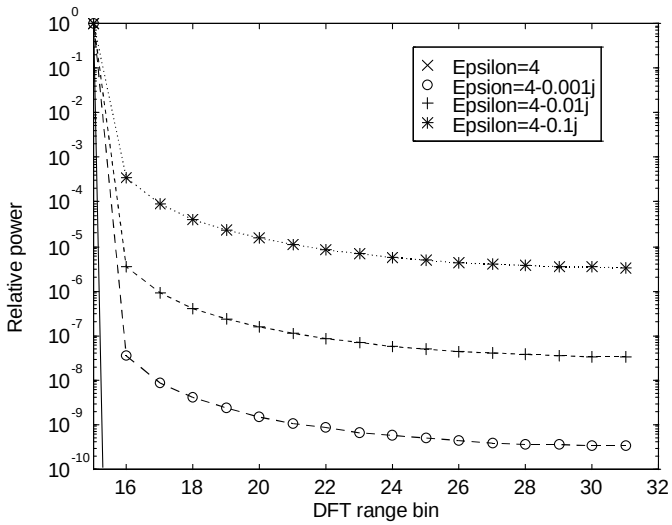

Figure C.2: The range profile for a target located at $15dz$ for increasing ε''_m

Figures C.2 and C.3 show that as the conductivity and dielectric losses in the medium increase, the model error e_n and hence the energy in the the sidelobes increase.

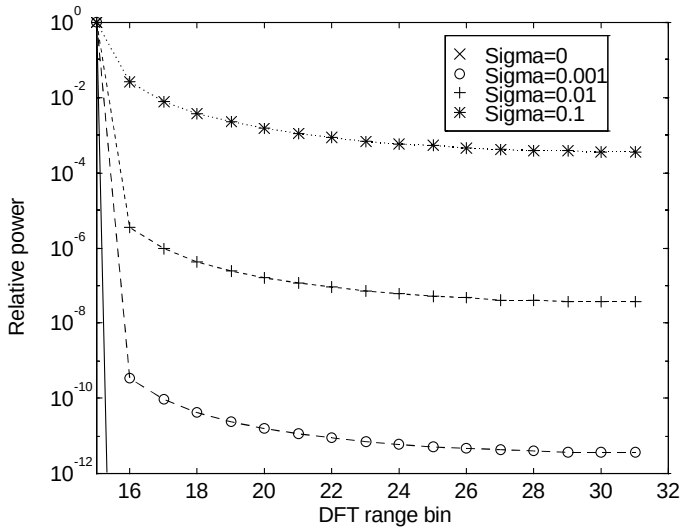

Figure C.3: The range profile for a target located at $15dz$ for increasing conductivity σ_m

Bibliography

[1] D. Banerjee, *PLL Performance, Simulation, and Design*. National Semiconductors, http://wireless.national.com, second ed., 2001.

[2] D. Daniels, *Surface-Penetrating Radar*. Radar, Sonar, Navigation and Avionics Series, IEE Publishing, 1996.

[3] D. A. Noon, *Step-Frequency Radar Design and Signal Processing Enhances Ground Penetrating Radar Performance*. PhD thesis, Department of Electrical & Computer Engineering. The University of Queensland, January 1996.

[4] G. Olhoeft, "Ground penetrating radar (ground probing radar, subsurface radar, georadar, earth sounding radar) GRORADAR(TM)." http://www.g-p-r.com, 2002.

[5] DeTec, "Commercial GPR products." http://diwww.epfl.ch/lami/detec, 2001.

[6] L. Assmussen, ed., *1st International Conference on Geotechnical Applications of Ground Penetrating Radar*, (USDoA/ARS, Tifton, Georgia USA), 1986.

[7] M. Collins, ed., *2nd International Symposium on Geotechnical Applications of Ground Penetrating Radar*, (University of Florida, Gainesville, Florida USA), 1988.

[8] J. E. Lucius, G. R. Olhoeft, and S. K. Duke, "Third International Conference on Ground Penetrating Radar ," Tech. Rep. 90-414, United States

Geological Survey (FGDC), 590 National Center, Reston, Virginia, 22092, May 1990.

[9] P. Hanninen, ed., May 14-18 1992.

[10] D. Redman, ed., *5th International Conference on Ground Penetrating Radar*, (Sensors and Software, Kitchener, Ontario Canada), 1994.

[11] S. Sato, ed., *6th International Conference on Ground Penetrating Radar*, (Tohoku University, Sendai, Japan), 1996.

[12] R. Plumb, ed., *7th International Conference on Ground Penetrating Radar*, (University of Kansas, Lawrence, Kansas, USA), 1998.

[13] D. Noon, ed., *8th International Conference on Ground Penetrating Radar*, (University of Queensland, Gold Coast, Australia), 2000.

[14] C. Nguyen, "Subsurface sensing technologies and applications." http://ee.tamu.edu/ssta-journal, 2002.

[15] L. Peters, J. Daniels, and J. Young, "Ground Penetrating Radar as a Subsurface Environmental Sensing Tool," *IEEE Proceedings*, vol. 82, pp. 1803–1821, December 1994.

[16] J. Young and L. Peters, *Applications of subsurface Transient Radar*, ch. 8, pp. 296–348. Nostrand Reinhold Company, 1988.

[17] L. A. Robinson, W. B. Weir, and L. Young, "Location and Recognition of Discontinuities in Dielectric Media Using Synthetic RF Pulses," *IEEE Proceedings*, vol. 62, pp. 36–44, January 1974.

[18] D. Crice, "GeoRadar inc. home page." http://www.georadar.com/, 2002.

[19] S. Koppenjan and M. Bashforth, "The Department of Energy's Ground Penetrating Radar (GPR), an FM-CW system," *SPIE AEROSPACE*, vol. 1942, pp. 44–55, 1993.

[20] S. K. Koppenjan, C. M. Allen, D. Gardner, H. Wong, H. R. Lee, and S. J. Lockwood, "Multi-Frequency Synthetic-Aperture Imaging with a Lightweight Ground Penetrating Radar System," *Journal of Applied Geophysics*, vol. 43, no. 2-4, pp. 251–258, 2000.

[21] G. F. Stickley, D. A. Noon, M. Cherniakov, and I. D. Longstaff, "Gated Stepped-Frequency Ground Penetrating Radar," *Journal of Geophysics*, vol. 43, pp. 259–269, March 2000.

[22] G. Albertia and et Al., "Advanced stepped frequency GPR development," in *Proc. Of the Conference on Subsurface Sensing Technologies and Applications II*, (San Diego, USA), SPIE, August 2000.

[23] ICTR, "Ground penetrating radar research at IRCTR (TU delft) funded by STW." http://irctr.et.tudelft.nl/GPR/, 2002.

[24] R. L. Roberts, *Analysis and Theoretical Modelling of GPR Polarization Data*. PhD thesis, The Ohio State University, 1994.

[25] Y. Xu, *Random Noise Polarimetry: Theory and Applications Toward Subsurface Probing*. PhD thesis, University of Nebraska, Lincoln, 1997.

[26] M. I. Skolnik, *Introduction to Radar Systems, 2nd Edition* . New York: McGraw-Hill Book Company, January 1980.

[27] D. R. Wehner, *High Resolution Radar*. Norwood, MA: Artech House, January 1987.

[28] S. Haykin, *Communication Systems, Fourth Edition*. McMaster University, 2000.

[29] A. J. Wilkinson, R. T. Lord, and M. R. Inggs, "Stepped-Frequency Processing by Reconstruction of Target Reflectivity Spectrum," in *Proceedings of the 1998 IEEE South African Symposium on Communications and Signal Processing*, (University of Cape Town), pp. 101–104, COMSIG'98, September 1998.

[30] R. T. Lord, M. R. Inggs, and M. K. Cope, "Measurements and Characteristics of RFI for a Low-Bandwidth VHF SAR System," in *Proc. 3rd European Conference on Synthetic Aperture Radar, EUSAR 2000*, pp. 845–848, EUSAR 2000, May 2000.

[31] M. A. Poirier, "Advanced ground penetrating radar," tech. rep., The Ohio State University Electroscience Laboratory, 1995.

[32] K. Iizuka and A. P. Freundorfer, "Detection of Nonmetallic Buried Objects by a Step Frequency Radar," *Institute of Electrical & Electronic Engineers*, vol. 71, pp. 277–279, February 1983.

[33] S. M. Kay and S. L. Marple Jnr., "Spectrum Analysis - A Modern Perspective," *IEEE Proceedings*, vol. 69, pp. 1380–1419, November 1981.

[34] T. Hauschild and F. Menke, "Using the GPOF Algorithm in Ground Penetrating Radar Systems," in *Proc. IEEE 1999 International Geoscience and Remote Sensing Symposium*, (IGARSS'99 Hamburg, Germany), 1999.

[35] V. K. Nguyen, K. H. Wu, H. Ogura, K. Iisuka, H. Mori, and A. P. Freundorfer, "Step-Frequency Radar," *J. Appl. Phys.*, vol. 56, pp. 2572–2583, November 1984.

[36] F. N. Kong and T. L. By, "Performance of a GPR System which uses Step Frequency Signals," *Journal of Applied Geophysics*, vol. 33, pp. 15–26, 1995.

[37] S. E. Hamran, D. T. Gjessing, J. Hjelmstad, and E. Aarholt, "Ground Penetrating Synthetic Pulse Radar : Dynamic Range and Modes of Operation," *J. Appl. Geophys.*, vol. 33, pp. 7–16, 1995.

[38] R. Kumaresan, D. W. Tufts, and L. L. Scharf, "A Prony Method for Noisy Data: Choosing the Signal Components and Selecting the Order in Exponential Signal Models," *IEEE Proceedings*, vol. 72, pp. 230–242, February 1984.

[39] W. M. Steedly and R. L. Moses, "High Resolution Exponential Modeling of Fully Polarized Radar Returns," *IEEE Trans. on Aerospace and Electronic Systems*, vol. 27, pp. 459–469, May 1991.

[40] D.-M. Chiang, *Parametric Signal Processing Techniques for Model Mismatch and Mixed Parameter Estimation*. PhD thesis, The Ohio State University, 1996.

[41] C.-C. Chen, M. B. Higgins, K. O'Neill, and D. R., "UWB fully-polarimetric GPR classification of subsurface unexploded ordnance," *IEEE Trans. on Geosci. Remote Sensing*, vol. 39, pp. 1221–1230, June 2001.

[42] W. Steinway and C. Barret, "Development Status of a Stepped-Frequency Ground Penetration Radar," *SPIE, Proc. of Underground and Obscured Object Imaging and Detection*, vol. 1942, pp. 34–40, April 15-16 1993.

[43] A. Langman, S. Dimaio, B. Burns, and M. R. Inggs, "Development of a low cost SFCW ground penetrating radar," in *Proceedings of the IEEE 1996 Geoscience and Remote Sensing Symposium*, vol. IV, pp. 2020–2022, IGARSS'96, May 1996.

[44] A. Langman, M. R. Inggs, and B. C. Flores, "Improving the resolution of a Stepped Frequency CW Ground Penetrating Radar," in *Conference on Advanced Microwave and Millimetre Wave Detectors, 39th SPIE Annual Symposium*, vol. 2275, Soc. Photo. Instrumentation Engineers, July 1994.

[45] A. Langman and M. R. Inggs, "New Technology UWB Stepped CW Radar," in *Proceedings of the PIERS workshop on Advances in Radar Methods*, vol. ISBN 92-828-1947-7, (Luxemborg Office for Official Publications of the EC), European Commission, July 1998.

[46] G. Farquharson, "Design and implementation of a 200 to 1600MHz, stepped frequency, ground penentrating radar transceiver," Master's thesis, Department of Electrical Engineering, University of Cape Town, August 1999.

[47] A. B. Wallis, "The Design and Implementation of a Distributed Data Capture and Processing Framework for Ground Penetrating Radar," Master's thesis, UCT Radar Remote Sensing Group, February 2001.

[48] W. C. Chew, *Waves and Fields in Inhomogeneous Media*. IEEE Press, 1990.

[49] G. Turner and F. Siggins, "Constant Q Attenuation of Subsurface Radar Pulses," *Journal of Geophysics*, vol. 59, pp. 1–10, August 1994.

[50] M. H. Powers, "Modelling frequency-dependant GPR," *The Leading Edge*, 1997.

[51] C. A. Balanis, *Advanved Engineering Electromagnetics*. John Wiley & sons, 1989.

[52] D. A. Noon and D. Longstaff, "Performances of GPR across a Broad Frequency Spectrum," in *Workshop on Applications of Radio Science (WARS '95)*, (Canberra, ACT, Australia), June 1995.

[53] D. A. Noon and G. F. Stickley, "Antenna Ring-Down, Range-Sidelobes and Quality Factors of Time- and Frequency-Domain GPR Systems," *Cooperative Research Centre for Sensor Signal & Info Proc.*, pp. 1–6, 1998.

[54] D. J. Daniels, D. J. Gunton, and H. F. Scott, "Introduction to Sub-surface Radar," *Institute of Electrical Engineers (United Kingdom)*, vol. 135, August 1988. Pt.F.

[55] P. Hoekstra and A. Delaney, "Dielectric Properties of Soils and UHF and Microwave Frequencies," *Journal of Geophysical Research*, vol. 79, pp. 1699–1708, April 1974.

[56] J. R. Wang, "The dielectric properties of soil-water mixtures at microwave frequencies," *Radio Science*, vol. 15, pp. 977–985, September 1980.

[57] T. J. Schmugge and J. R. Wang, "An Empirical Model for the Complex Dielectric Permittivity of Soils as a Function of Water Content," *IEEE Trans. on Geosci. Remote Sensing*, vol. GE-18, pp. 288–295, October 1980.

[58] G. P. Deloor, "The dielectric properties of wet materials," *IEEE Trans. on Geosci. Remote Sensing*, vol. GE-21, pp. 364–369, July 1983.

[59] M. C. Dobson, F. T. Ulaby, M. Hallikainen, and M. A. El-Rayes, "Microwave Dielectric Behavior of Wet Soil-Part II: Dielectric Mixing Models," *IEEE Trans. on Geosci. Remote Sensing*, vol. GE-23, pp. 35–46, January 1985.

[60] M. Hallikainen, F. T. Ulaby, M. C. Dobson, M. A. El-Rayes, and L. Wu, "Microwave Dielectric Behaviour of Wet Soil-Part1:Empirical Models and Experimental Observations," *IEEE Trans. on Geosci. Remote Sensing*, vol. GE-23, pp. 25–34, January 1985.

[61] W. R. Scott and G. S. Smith, "Measured Electrical Constitutive Parameters of Soil as Functions of Frequency and Moisture Content," *IEEE Trans. on Geosci. Remote Sensing*, vol. 30, pp. 621–623, May 1992.

[62] N. R. Peplinski, F. T. Ulaby, and M. C. Dobson, "Dielectric Properties of Soils in the 0.3-1.3 GHz Range," *IEEE Trans. on Geosci. Remote Sensing*, vol. 33, pp. 803–807, May 1995.

[63] F. Hollender and S. Tillare, "Modelling Ground-Penetrating Radar Wave Propagation and Reflection with the Jonscher Parameterization," *Geophysics*, vol. 63, pp. 1933–1942, December 1998.

[64] D. Chiang and L. C. Potter, "Parameter Estimation Algorithm for a GTD-Based Model of Complex-Valued Stepped-Frequency, Monostatic Radar Measurement," tech. rep., Signal Processing and Artifical Neural Networks Laboratory, The Ohio State University, 1995.

[65] M. P. Hurst and R. Mittra, "Scattering Center Analysis Via Prony's Method," *IEEE Trans. on Antennas and Propagat.*, vol. AP-35, no. 8, pp. 986–988, 1987.

[66] R. Kumaresan and D. Tufts, "Improved Spectral Resolution III : Efficient Realization," *IEEE Proceedings*, vol. 68, no. 10, pp. 1354–1355, 1980.

[67] D. W. Tufts and R. Kumaresan, "Estimation of Frequencies of Multiple Sinusoids: Making Linear Prediction Perform Like Maximum Likelihood," *IEEE Proceedings*, vol. 70, pp. 975–989, September 1982.

[68] D. W. Tufts and R. Kumaresan, "Singular Value Decomposition and Improved Frequency Estimation Using Linear Prediction," *IEEE Trans. on Acoust., Speech, and Signal Processing*, vol. ASSP-30, pp. 671–675, August 1982.

[69] Y. Hua and T. K. Sarkar, "Matrix Pencil Method for Estimating Parameters of Exponentially Dampled/Undamped Sinusoids in Noise," *IEEE Trans. on Acoust., Speech, and Signal Processing*, vol. 38, pp. 814–824, May 1990.

[70] S. M. Kay, *Fundamentals of Statistical Processing, Volume 1: Estimation Theory, 1/e.* Prentice Hall, 1993.

[71] D.-M. Chiang and L. C. Potter, "On the Equivalence of Exponential Signal Estimators," tech. rep., The Ohio State University, 1997.

[72] R. O. Schmidt, "Multiple Emitter Location and Signal Parameter Estimation," *IEEE Trans. on Antennas and Propagat.*, vol. AP-34, pp. 276–280, March 1986.

[73] Y. Hua and T. K. Sarkar, "Generalized pencil-of-functions method for extracting the poles of electromagnetic system from its transient response," *IEEE Trans. of Antennas and Propagat.*, vol. 37, pp. 229–234, Feb. 1989.

[74] M. Zoltowski and F. Haber, "A Vector Space Approach to Direction Finding in a Coherent Multipath Environment," *IEEE Trans. on Antennas and Propagat.*, vol. AP-34, no. 9, pp. 1069–1079, 1986.

[75] R. Roy, A. Paulraj, and A. Kailath, "ESPRIT = a Subspace Rotation Approach to Estimation of Parameters of Cissoids in Noise," *IEEE Trans. on Acoust., Speech, and Signal Processing*, vol. 34, no. 10, pp. 1340–1343, 1986.

[76] M. D. A. Rahman and K.-B. Yu, "Total Least Squares Approach for Frequency Estimation Using Linear Prediction," *IEEE Trans. on Acoust., Speech, and Signal Processing*, vol. ASSP-35, pp. 1440–1454, October 1987.

[77] W. M. Steedly, C. J. Ying, and R. L. Moses, "Statistical Analysis of TLS-Based Prony Technique," *Automatica: Special Issue on Statistical Signal Processing and Control*, January 1994.

[78] K. T. Kim, D. K. Seo, and H. Kim, "Radar Target Identification Using One-Dimensional Scattering Centers," *IEEE Proc. Radar, Sonar Navigation*, vol. 148, pp. 285–296, October 2001.

[79] A. P. Freundorfer, *Step Frequency Radar*. PhD thesis, University of Toronto, 1989.

[80] F. J. Harris, "On the Use of Windows for Harmonic Analysis with the Discrete Fourier Transform," *IEEE Proceedings*, vol. 66, No. 1, pp. 51–83, January 1978.

[81] A. Langman and M. R. Inggs, "Pulse versus Stepped Frequency Continuous Wave Modulation for Ground Penetrating Radar," in *Processings of IGARSS 2001*, (University of New South Wales, Sydney, Australia), IEEE, IEEE, July 2001.

[82] L. C. Chan and L. Peters Jr., "Characterization of Subsurface Radar Targets ," *IEEE*, vol. 67, no. 7, p. 991, 1979.

[83] L. C. Chan, L. Peters, and D. L. Moffat, "Improved Performance of a Subsurface Radar Target Identification System through Antenna Design," *IEEE Trans. Antennas and Propagat.*, vol. AP-29, pp. 307–311, March 1981.

[84] I. Arai and T. Suzuki, "Experimental Results on Subsurface Radar with Improved Resolution," *Journal of Electromagnetic Waves and Applications*, vol. 7, no. 11, pp. 1479–1495, 1993.

[85] Y. Xu, R. M. Narayanan, X. Xu, and C. J. O., "Polarimetric Processing of Coherent Random Noise Radar Data for Buried Object Detection," *IEEE Trans. on Geosci. Remote Sensing*, vol. 39, no. 3, pp. 467–478, 2001.

[86] R. M. Narayanan, R. T. Becker, and B. M. B., "Detection of Buried Pipes Using Polarimetric Stepped Frequency Ground Penetrating Radar GPR Images," *Pipes and Pipelines International*, vol. 45, no. 3, pp. 15–31, 2000.

[87] S. J. Radzevicius, *Dipole Antenna Properties and their Effects on Ground Penetrating Radar Data*. PhD thesis, The Ohio State University, 2001.

[88] A. Langman and M. R. Inggs, "The Use of Polarimetry in Subsurface Radar," in *Proceedings of the 1994 International Geoscience & Remote Sensing Symposium (IGARSS '94)*, vol. 4, (Pasadena, USA), pp. 2489–2491, IGARSS '94, August 94.

[89] A. Langman and M. R. Inggs, "A SFCW Polarimetric Ground Penetration Radar," in *Proceedings of the Fifth International Ground Penetrating Radar Conference, Waterloo, Canada*, pp. 1–19, Proc. of the 5th int.conf. on Ground Penetrating Radar, July 94.

[90] F. T. Ulaby and C. Elachi, *Radar Polarimetry for Geoscience Application*. Artech House, 1990.

[91] J. C. Hubbert, "A Comparison of Radar, Optic, and Speculare Null Polarization Theories," *IEEE Trans. on Geosci. Remote Sensing*, vol. 32, pp. 658–671, May 1994.

[92] S. R. Cloude, "Polarimetric Techniques in Radar Signal Processing," *Microwave Journal*, pp. 119 – 127, July 1993.

[93] F. T. Ulaby, M. Whitt, and K. Sarabandi, "AVNA - Based Polarimetric Scatterometers," *IEEE Trans. on Antennas and Propagat.*, pp. 6–16, October 1990. Magazine.

[94] E. Ertin and L. C. Potter, "Polarimetric Classification of Scattering Centers," tech. rep., Department of Electrical Engineering, The Ohio State University, Columbus, OH 43210, 1996.

[95] C. D. Graves, "Radar Polarization Power Scattering Matrix," in *IRE*, (U.S.A.), pp. 248–252, IRE, February 1955.

[96] J. R. Huynen, "Measurement of the Target Scattering Matrix," *IEEE Proceedings*, pp. 936–946, August 1965.

[97] J. R. Huynen, *Phenomenological Theory of Radar Targets*. PhD thesis, Technical University of Delft, Delft, The Netherlands, 1970.

[98] W.-M. Boerner, W.-L. Yan, A.-Q. Xi, and Y. Yamaguchi, "On the Basic Principles of Radar Polarimetry: the Target Characterostoc Polarization State Theory of Kennaugh, Huynen's," *IEEE Proceedings*, vol. 79, pp. 1538–1550, October 1991.

[99] W.-M. Boerner, W.-L. Yan, A.-Q. Xi, and Y. Yamaguchi, "Basic Equations of Radar Polarimetry and Its Solutions MIKON-91," *University of Illinois at Chigago*, vol. 2, pp. 13–30, 1991.

[100] A. P. Agrawal and W.-M. Boerner, "Redevelopment of Kennaugh's Target Characteristic Polarization State Theory Using the Polarization Transformation Ratio," *IEEE Trans. on Geosci. Remote Sensing*, vol. 27, pp. 2–14, January 1989.

[101] A. B. Kostinski and W.-M. Boerner, "On Foundations of Radar Polarimetry," *IEEE Trans. on Antennas and Propagat.*, vol. AP-34, pp. 1395–1404, December 1986.

[102] M. Davidovitz and W.-M. Boerner, "Extension of Kennaugh's Optimal Polarization Concept to the Asymmetric Scattering Matrix Case," *IEEE Trans. on Antennas and Propagat.*, vol. AP-34, pp. 569–573, April 1986.

[103] N. E. Chamberlain, E. K. Walton, and F. D. Garber, "Radar Target Identification of Aircraft Using Polarization- Diverse Features," *IEEE Trans. on Aerospace and Electronic Systems*, vol. 27, pp. 58–67, January 1991.

[104] Y. Wang, J. Zallat, and J. Saillard, "Polarimetric High Resolution Methods," in *Third International Workshop on Radar Polarimetry*, (Nantes, France), pp. 480–491, March 1995.

[105] J. R. Huynen, "Lexicographic Radar Target Analysis," tech. rep., P.Q. Research, 10531 Blandor Way, Los Altos Hills, California 94024, March 1994.

[106] J. R. Huynen, "A New Extended Target Decomposition Scheme," Tech. Rep. P.Q.R. 109, P.Q. Research, 10531 Blandor Way, Los Altos Hills, California 94024, March 1994.

[107] S. Uratsuka, K. Okamoto, H. Mineno, and S. Mae, "Step Frequency Radar Experiments on the Antartica Sea Ice," in *Processing of IGARSS'88*, (Edinb. Scotland), pp. 1703–1706, IEEE, September 1988.

[108] Groundprobe, "GroundProbe." http://www.groundprobe.com/, 2002.

[109] E. S. Eide and J. Hjelmstad, "A Multi Antenna Ultra Wideband Ground Penetrating Radar System Using Arbitrary Waveforms," in *IGARSS'99*, p. (3), IGARSS'99, 1999.

[110] A. D. M. Garvin, "Investigation into the uses and accuracy of a Stepped-Frequency Continuous Wave Radar," tech. rep., Dept Electrical Engineering, University of Cape Town, Private Bag, Rondebosch 7700, South Africa, November 1990.

[111] A. D. M. Garvin, "Range, resolution and imaging applications of a Stepped Frequency Continuous Wave Radar," *Proc. SAIEE*, September 1991.

[112] M. R. Inggs and A. Garvin, "A Stepped Frequency CW Ground Penetration Radar," in *Proceedings of the Microwave Signatures-92 Conference, Igls, Austria, July, 1992*, (Inst. for Radio Frequency Technology, Oberpfaffenhofen), pp. 1c13–1c16, German Aerospace Research Establishment (DLR), July 1992.

[113] A. Langman, "Video Pulse Radar Prestudy," tech. rep., Dept Electrical Engineering, University of Cape Town, Private Bag, Rondebosch 7700, South Africa, September 1991.

[114] M. R. Inggs and A. Langman, "Stepped Frequency Continuous Wave Radar for Sub-surface Sensing Applications," tech. rep., UCT Radar Remote Sensing Group, October 1992.

[115] M. Kabutz, A. Langman, and M. R. Inggs, "Hardware Cancellation of the Direct Coupling in a stepped CW Ground Penetrating Radar," in *Proceedings of the 1994 International Geoscience & Remote Sensing Symposium (IGARSS '94)*, vol. 4, (Pasadena, USA), pp. 2505–2507, IGARSS '94, August 94.

[116] A. Langman, "Project: Minerad: Radar RF Transceiver Unit Development Specification and Design Document," tech. rep., Reutech Radar Systems, Technopark Stellenbosch, January 1997.

[117] M. H. Kabutz, "L-Band Stepped Frequency Mine Detection Radar - System Design," tech. rep., UCT Radar Remote Sensing Group, July 1996.

[118] J. B. Tsui, *Digital Techniques for Wideband Receivers*. Norwood, MA: Artech House, 1995.

[119] T. Williams, *EMC for Product Designers*. Reed Educational and Professional Publishing Ltd, second ed., 1996.

[120] D. Daniels, "Ultra-wideband detection of buried objects," in *IEEE IGARSS Proceedings*, (IGARSS'97 Singapore), pp. 1278–1281, August 1997.